Contributions to the Automated Segmentation of Brain Tumors in Magnetic Resonance Images

Der Technischen Fakultät der
Universität Erlangen-Nürnberg

zur Erlangung des Grades

D O K T O R - I N G E N I E U R

vorgelegt von

Michael Kaus

Erlangen - 1999

Als Dissertation genehmigt von
der Technischen Fakultät der
Universität Erlangen-Nürnberg

Tag der Einreichung:

Tag der Promotion:

Dekan:	Prof. Dr.-Ing. habil. G. Herold
Berichterstatter:	Prof. Dr.-Ing. Dieter Seitzer
	Prof. Dr. Heinrich Niemann
	Prof. Dr. med. Ron Kikinis

Abstract

This thesis studies the problem of the segmentation of magnetic resonance images (MRI) in patients with meningiomas and low grade gliomas. The studies are motivated by the potential of computer assisted neurosurgery to improve treatment outcome. To make such methods clinically practical, these techniques require the development of automated segmentation methods.

First, the MR imaging characteristics of meningiomas and low grade gliomas are analyzed to assess the possibilities of automated segmentation. The analysis demonstrates that segmentation is not possible with a) statistical classification due to overlapping intensity distributions of tissue classes, or b) the spatial alignment (registration) of an anatomical normal brain atlas because such an atlas does not describe pathology.

Subsequently, a segmentation framework that iterates statistical classification, local segmentation techniques and registration of a brain atlas is described and shown to allow complete segmentation of the skin surface, the brain, the ventricles and the tumor. A validation study with clinical MRI data demonstrates that the algorithm performs well despite the presence of overlapping intensity distributions of tissue classes. The reduction of operator time from 3 hours to 5-10 minutes makes it practical to consider the integration of computerized segmentation into clinical routine.

The use of optical flow methods for the task of aligning an anatomical atlas to individual patient datasets is analyzed. An existing 2D optical flow approach that models discontinuous deformation fields is extended to 3D, and a novel N-channel probabilistic (NP) similarity measure is proposed that separates labels of different objects into different channels and incorporates classification probabilities as a confidence measure. A validation study with clinical and simulated MRI demonstrates that registration accuracy can be significantly improved for the alignment of multiple templates, and for the registration of templates to images with classification errors.

The algorithms developed in this thesis are also used to project structural information (e.g. white matter tracts) from a normal brain atlas onto patients with brain tumors. The method provides anatomical information, which is not available from conventional MRI, for the planning of surgical approaches.

This thesis contains three major contributions: a robust, reproducible and accurate method for the segmentation of brain tumors in MRI, a 3D adaptive regularization optical flow method and an N-channel probabilistic similarity measure for template matching.

Acknowledgements

My deepest gratitude goes to my supervisors, Prof. Dr.-Ing. Dieter Seitzer, and Prof. Dr. med. Ron Kikinis, for their encouragement, guidance and support throughout my studies.

I thank Prof. Dr. med. Ference Jolesz for generously hosting me at the Department of Radiology, Brigham & Women's Hospital, Harvard Medical School.

Special thanks goes to Simon Warfield, PhD for making my stay at the SPL such a valuable experience. He has provided the foundations to my studies, guided me during my time at the Surgical Planning Lab in a highly approachable manner, and amazed me with having all the answers to my questions about medical image analysis.

Particular gratitude also goes to William H. Wells, PhD, for his support and guidance, for instructing me in many medical image analysis problems, in particular the registration methods, and his help with the preparation of the thesis.

I thank Prof. Dr. Heinrich Niemann for the second review of the thesis.

I thank Prof. Dr. med. Rudolf Fahlbusch and PD Dr. med. Ralf Steinmeier for the invaluable clinical experiences during my time as a research fellow at the neurosurgical department in Erlangen, for leading me to the field of medical image analysis and guiding my first steps.

I thank Dr.-Ing. Joachim Dengler for generously sharing his competence and insights in non-linear registration techniques.

Deep appreciation goes to the staff of the Surgical Planning Laboratory for providing excellent working conditions, in particular Dr.-Ing. Carl-Fredrik Westin for being a great colleague, his help with scientific visualization and many useful discussions, Andre Robatino, PhD, for his help with non-linear registration methods, Dr. med. Arya Nabavi for valuable discussions and help with the medical aspects of the manuscript, Alexandra Chabrerie, Carl Kolvenbach, Charles Mamisch, Drs. med. Emmanouel Chatzidakis, Arya Nabavi, Fatma Ozlen, Daniel Boll, for sharing their insights to Neurosurgery with me, and for help with the selection and many hours of preparation of the clinical data.

Deepest gratitude goes to my wife, Ortrun Icke, for love, support and encouragement, and my parents, for long-distance support and encouragement.

This work was funded by grants DAAD D/96/34017 and Whittaker RG-96-0440.

Contents

Chapter 1

Introduction

One of the principal problems in neurosurgical planning is the localization of critical brain structures with respect to the tumor to define the safest possible surgical approach. The surgical intervention requires accurate cortical localization, the definition of exact target trajectories, and the identification of anatomical and pathological boundaries.

Medical imaging and computer assisted surgery techniques have become increasingly utilized in neurosurgery [2, 9, 65, 69, 79, 97, 106, 145]. Some of the most substantial reasons for this are:

- The availability of accurate anatomical three-dimensional (3D) models from 2D medical image data provides precise information about spatial relationships between critical anatomical structures (e.g. eloquent cortical areas, vascular structures) and pathology which are often indistinguishable by the naked eye [65, 81, 97].

- Computer assisted surgical planning allows the surgeon to test and analyze alternative navigational paths and movements through physical space using an interactive 3D display. This facilitates the surgeons preoperative definition of the safest possible approach that will result in the least possible damage to normal tissue [18, 65, 80, 87, 97].

- "Neuronavigation" systems that are based on frameless stereotaxy devices track surgical instruments relative to preoperative image information of the patient in real-time [40, 41, 79, 92, 106, 114, 144, 145]. Neuronavigation increases the safety of pathologic tissue removal by improving localization and targeting, and enables accurate determination of the margins of the tumor within the normal brain to avoid eloquent areas of brain [2, 9, 65, 69, 79, 97, 100, 106, 145].

Today commercially available neuronavigation systems only provide the surgeon with 2D cross-sections of the intensity value images and a 3D model of the skin. The main limiting factor for routine use of 3D models in daily clinical practice is the amount of time that an operator has to spend in the preparation of the data [97]. The availability of automated methods will significantly reduce the time and is necessary to make such methods practical.

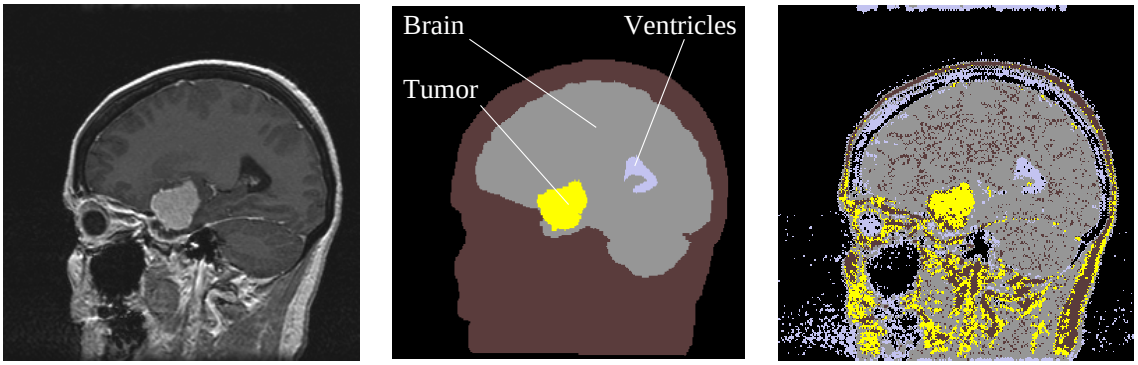

(a) Saggittal cross-section of MRI volume (Meningioma)

(b) Manual segmentation

(c) Statistical classification

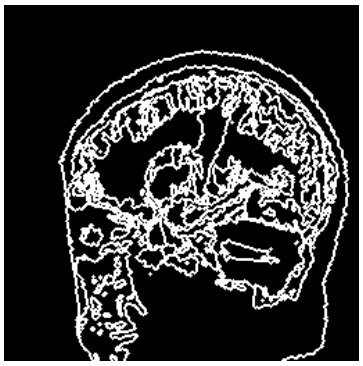

(d) Outline of all structures in the registered anatomical atlas

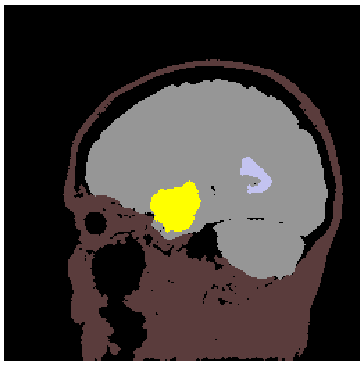

(e) Combination of statistical classification and model-based methods

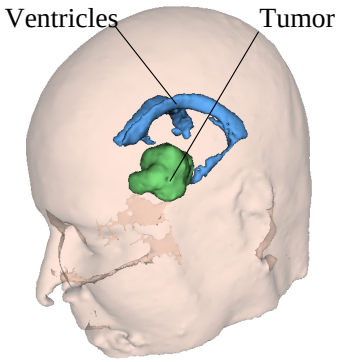

(f) 3D model

Figure 1.1: **Illustration of the segmentation of a brain tumor using different methods.** *Classification (c) or model-based methods (d) alone cannot successfully segment normal and pathologic tissue. The combination of both methods (e) allows a segmentation similar to the manual segmentation of a clinical expert (b).*

A prerequisite for image based modeling is segmentation. Segmentation is a method of separating the data into anatomical objects by labeling intensity value images according to the tissue type. Many medical image segmentation approaches evolved from general image processing methods such as low level image operations (thresholding, edge detection, mathematical morphology) [112], statistical classification [25, 48, 133], active contours [94] or neural networks [25]. For tumor segmentation, conventional segmentation methods work well in some cases but will not differentiate between non-enhancing tumor and normal tissue [25, 50, 135, 136]. Clinical image analysis indicates that methods based on image information alone are insufficient for successful differentiation between tissues (see Figure 1.1c) [70, 71].

A different aproach are template based segmentation methods [31, 139, 141]. The information about the size, shape and location of anatomical structures is gained

directly from a digital anatomical atlas [81]. "Registration" methods allow to adapt the anatomical atlas to the patient's individual image data of the.

The majority of the prior template based segmentation work focuses on the segmentation of normal brain or brains with multiple sclerosis (MS) lesions, which are small in size and limited to a subset of the brain tissue, the white matter [38, 72, 140, 141]. Tumors, however, vary greatly in size, shape, location, tissue composition and homogeneity [71, 152]. The lack of general a priori shape information in tumors makes their standardisation in an atlas difficult, which is why this method cannot be directly used to segment brain tumors (see Figure 1.1d).

For these reasons, this work has two goals: First, to demonstrate that accurate and robust automated segmentation of MRI of normal and tumor tissue is possible with the combination of anatomical knowledge, statistical classification and structural segmentation methods (see Figure 1.1e). Second, to investigate and improve state of the art registration methods with the purpose of optimizing their use for the adaptation of a digital brain atlas to individual patient image datasets.

After a review of the current state of the art (Chapter 2) a methologic overview is given (Chapter 3), before the algorithms are described in detail. This includes the specification of a method for the automated segmentation of normal and tumor tissue of MRI in patients with meningiomas and low grade gliomas (Chapter 4), and the comparison of several optical flow methods and the development of a new method for improved registration of an atlas to individual patient datasets (Chapter 5). Finally, the methods developed in this thesis are validated in Chapter 6.

The segmentation methods presented in this work are currently used routinely and for further clinical evaluation at the Brigham & Women's Hospital, Harvard Medical School, Boston, MA, USA.

Chapter 2

State of the Art

2.1 Medical Applications

Medical images are rich in information that can be used for diagnosis and subsequent therapeutic interventions. While the increased availability of imaging modalities such as MR, CT, MR-angiography and functional imaging is of considerable use to the medical practitioner, these methods are still inherently limited because they provide images with information content limited by the physical characteristics of the imaging device. While visual inspection of the 2D images is often sufficient for the practitioner, some situations require image post-processing (i.e. segmentation) for the extraction and utilization of the structural and geometric information inherent in the 3D medical imagery.

Applications in the area of treatment of patients with brain tumors range from identification and characterization of a tumor [70, 71, 107, 109], quantitative volume-measurement for the planning and evaluation of radiotherapy [50, 132, 131, 135], to surgical planning and intra-operative guidance, where 3D visualization provides improved insight into spatial relationships between brain structures and aids in the task of localizing e.g. tumor-boundaries and critical areas (e.g. motory and sensory cortex) [43, 69, 92, 97, 98, 114, 144]. Preliminary results demonstrate improvement of existing treatment methods and new possibilities for therapy [9, 69, 97, 117, 130, 132, 135].

Significance of MRI

Magnetic resonance imaging (MRI) is the most frequently used imaging technique in clinical neuroscience and neurosurgery for noninvasively establishing diagnosis, quantitatively evaluating disease processes and guiding therapy [67]. This is because of the absence of ionizing radiation, as opposed to other imaging methods such as x-ray computer-tomography (CT), its capacity to produce images in planes with any orientation, and superior contrast resolution of soft tissue, such as tumor and related pathologic tissue (edema, necrotic and cystic parts) (see Appendix A) [52, 152].

Surgical Planning

One of the principal problems in surgical planning is the precise localization of critical brain structures with respect to the tumor to define the safest possible surgical approach with the least possible damage to normal tissue.

While 2D images accurately describe the size and location of anatomical objects, 3D views from 2D images highlight structural information and spatial relationships of the anatomy. The process of generating 3D views, however, is a difficult task and is traditionally carried out in the clinicians mind.

However, with image processing tools, the information in the orthogonal 2D cross-sections can be enhanced and interactively displayed using 3D models (see Figure 2.1). This considerably helps the surgeon in the trajectory optimization process and the planning of the procedure by:

- allowing him to test and analyze alternative navigational paths and movements through the physical space
- improving the spatial information about relationships of critical structures (e.g. pre- and post-central gyri, vascular structures) and pathology
- providing an integrated display of information from different imaging modalities such as CT, MR, MR-angiography or functional imaging
- presenting image information in a way that is more similar to the surgical view of the patient during the operation, thus facilitating the comprehension of the entire anatomy. For example, the (mental) 3D visualization of structures that do not readily align with the planes of the image acquisition (e.g. the vascular tree) is difficult based on 2D images alone but is essential to the surgical procedure.

Image guided surgical planning methods have been successfully applied to choose the optimal position of entry and trajectory of the approach, enable optimal craniotomy (the "opening of the skull"), simulate the surgical opening and the tumor resection, and enhance neuroanatomic and neurosurgical training [18, 65, 81, 87, 97].

Computer based Intraoperative Image Guidance

Cranial neurosurgery has been a major area of the application of image guidance because even small damage to the brain during access to target areas can have very serious consequences for the patient, and the human surgical visualization during surgery is a complex task since:

- The neurosurgeon has a limited view of the operating field. For example, conventional craniotomy restricts the surgeons view by the relatively small area of exposed brain surface.
- The surgeon cannot visualize structures beyond the exposed surfaces, making it difficult to comprehend all of the relevant anatomy.

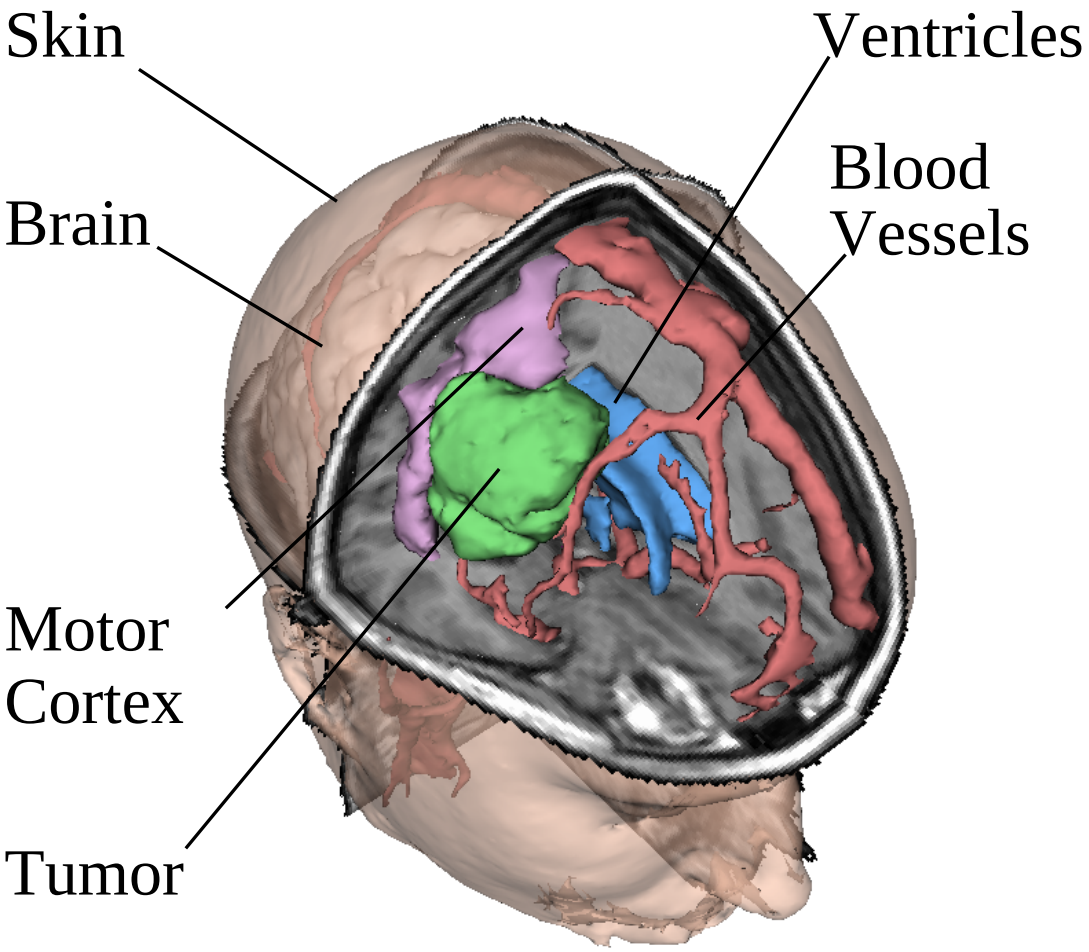

Figure 2.1: **3D rendering of anatomical model for surgical planning and intra-operative visualization.** *The visualization software ("3D Slicer", [49]) allows for arbitrary reformatting of 2D cross-sections, and translation, rotation and zooming of the scene. During surgery, the position of a surgical instrument is indicated in the 3D-scene by display of a virtual pointer.*

- Integration of the preoperatively acquired 2D imaging information has to be done mentally, to treat disease processes that are manifest in 3D.
- It is difficult in some cases to assess the margins of a tumor. For example, the margins of a low grade astrocytoma are often indistinguishable from surrounding brain on visual inspection. For a high grade tumor, gadolinium staining demarcates tumor growth more clearly than visual inspection and the enhancing margin may not correspond to anything visually.

Such limitations of direct surgical visualization have several consequences. Cortical localization is not accurate, the definition of exact trajectories of targeting is impossible, and in order to ensure complete resection, normal tissue has to be removed if the anatomical and pathological boundaries are not clear.

Tumor surgery can be significantly improved by image guidance. Frameless stereotaxy devices (or "Neuronavigation systmes") track surgical or pointing instruments relative to preoperative image information of the patient in real-time. By tracking the 3D pose (position) of surgical instruments, in conjunction with tracking the 3D pose of the patient, the operator can be navigated through 3D coordinates by showing the position of the instrument on 2D scans or 3D visualizations of the anatomy of the patient [145, 144, 41, 114, 106, 79, 92] or by overlaying 3D renderings of anatomical structures on the surgeons view of the patient [55, 54, 35]. Neuronavigation improves localization and targeting based on previously-acquired images, enables accurate determination of the margins of the tumor within the normal brain to avoid eloquent areas of brain [69, 9, 145, 106, 79, 97, 65, 2, 100].

MR-guided Intraoperative Image Guidance

During surgery, preoperatively acquired image information is no longer accurate. This is due to patient movement and shifts or deformations of the anatomy resulting from the surgical intervention. In this situation either partial correction of the 3D models or full volumetric image update is necessary, which can be acquired from intraoperative imaging. In this scenario, the entire operation takes place inside MR scanning devices which provide the surgeon with continuous real-time imagery during the surgical intervention [110, 56, 89, 9, 130, 90, 117]. Preliminary work has been reported on the measurement of brain shift, updating of preoperative images by warping and fusion to intraoperative image volumes and intraoperative image segmentation for updating of the preoperative 3D models [59, 60, 142].

Radiation Treatment Monitoring

MRI is often used for monitoring tumor response to radiation therapy. By taking multiple images of a subject over time a clinician can effectively track progress or regress of a medical condition and quickly determine the impact of radiation treatment of brain tumors. By using initial images as a baseline, subject tracking results in interpretations that are specific to an individual. Computer-based segmentation of MRI data improves the boundary definition of pathologic tissue and provide the means for an objective and reproducible measurement of tumor response or relative tumor volume measurement during therapy, which is important for clinical trials. [8, 24, 135, 132, 131].

Motivation for Automated Segmentation

Image segmentation is an essential requirement for the applications described above, and the automation of the segmentation process is a crucial task for several reasons (e.g. [3, 48, 71, 95]):

- The complexity and variability of the brain can make the identification of different structures difficult. The situation is even worse for brain tumors.
- Due to the sheer size of the datasets, manual segmentation is labor intensive and thus not feasible in standard clinical settings.

- Manual segmentation is subject to human error, resulting in unpredictable inter- and intra- operator variability.

Requirements for the Clinical Application of Segmentation

To meet the requirements of clinical routine, the constraints on segmentation methods for medical image analysis are [48]:

- minimal user interaction
- efficient procedures running on standard computer hardware
- robustness (insensitivity to noise and to variations among patients)
- reliability (predictable results)

2.2 Magnetic Resonance Imaging (MRI): Basic Principles and Properties

This section provides a brief introduction to magnetic resonance imaging, outlines artifacts and limitations and gives an overview of considerations concerning the application of MRI on the pathologic brain. Further readings on MRI physics and application can be found in [85, 99, 101, 146].

2.2.1 Conceptual Overview

In medical settings MRI is used to produce high quality images of the inside of the human body. Clinical MR images are based on proton density and proton relaxation dynamics. These vary according to the tissue under examination and reflect its physical and biochemical properties. Different tissues are characterized and discriminated according to the different properties of their constituents (water, iron, fat, blood and its breakdown products).

The MR images are obtained by placing the patient or area of interest within a powerful, highly uniform, static magnetic field. Magnetized protons (hydrogen nuclei) within the patient align like small magnets in this field. Radiofrequency pulses are then utilized to create an oscillating magnetic field perpendicular to the main field, from which the nuclei absorb energy and move out of alignment with the static field, in a state of excitation. As the nuclei return from excitation to the equilibrium state, a signal induced in the receiver coil of the instrument by the nuclear magnetization can then be transformed by a series of algorithms into diagnostic, digital images.

During a single image acquisition, several components of the received signals are recorded, the most common being the proton densities and the relaxation time constants T1 and T2[1]. Hence, an image represents the spatial distribution of several

[1]T1 (spin-lattice relaxation time) describes the relaxation time of the nuclei as projected on the longitudinal z-axis, z being the direction of the main constant magnetic field. T2 (spin-spin relaxation time) describes the relaxation time as projected on the transverse xy-plane

distinct tissue-related parameters. Each pixel/voxel is a feature vector of these properties.

2.2.2 Image Artifacts and Limitations

The quality of image processing is limited by the quality of the underlying imaging technique. Thus, it is important to know and understand the characteristics and limitations of MRI. This section provides a qualitative overview of common artifacts seen in clinical magnetic resonance images and comments on its limitations with respect to imagery of pathologic brain.

Dropouts and Shifts

Shift artifacts cause displacement of a reconstructed object from its true position in the image and local image distortions. They are due to susceptibility artifacts (change of magnetic susceptibility at tissue boundaries) or chemical shifts (shift of frequency response due to the chemical environment) and occur where air/tissue, tissue/bone, or tissue/metal form boundaries. A second effect of susceptibility artifacts is signal dropout, which appear near air-tissue and tissue-bone interfaces [115].

Motion

Motion artifacts appear as repeating densities oriented in the scanning direction or "ghost images". These result from motion during the acquisition of a sequence. In brain imagery, this artifact is most commonly caused by physical movement of the subject during image acquisition [115].

Partial Volume Effect

The partial volume effect results from the finite spatial resolution of the MR image: a pixel/voxel may represent more than one kind of tissue type. As a result, borders between two different tissues types are blurred or misrepresented. In brain imagery, this typically appears at the interfaces brain surface with cerebro-spinal fluid (CSF) (see Appendix A for anatomical description), where CSF may appear as white matter [48].

Noise

The signal-to-noise (SNR) ratio increases proportional to the pixel/voxel size (i.e. the field of view (FOV) and the resolution), proportional to the square root of the imaging time and is determined to a significant extent by the strength of the external magnetic field [146]. The noise may be modeled as additive, rayleigh distributed white noise [140].

Geometric and Signal Distortions

Inhomogeneities in the static or gradient magnetic field cause systematic geometric and intensity signal distortions. Gradient field inhomogeneities may distort an image to a bow tie, barrel or potato chip shape. A nonlinear static magnetic field causes the intensity signal of a tissue type to vary spatially [84, 118].

Contrast

Contrast between tissues is highly sensitive to the choice of parameters, e.g. the type of sequence, T1-,T2-, PD-weighting, resolution and artifacts. For the characterization of brain tumors, MR tissue parameters are not sufficient for distinction between tumors (types, degree) or between tumor tissues (active tissue, edema, necrosis, cystic parts), which is partly explained by the large variety of tumor types and varying degrees in many tumors [70, 71].

2.2.3 Features of the Application to the Pathologic Brain

The main quality measures in MRI are high tissue contrast, resolution and SNR. These are functions of numerous intrinsic and extrinsic parameters and thus subject to a complex optimization process. The most important intrinsic parameters, which are measured in the course of the MR examination, are the spin-lattice relaxation time (T1), the spin-spin relaxation time (T2), and the proton density (PD), which depend on the different tissue characteristics. The extrinsic parameters are those chosen by the examining physician and include the echo time (TE), repetition time (TR), field-of-view (FOV), slice thickness, and resolution. In addition, there is a wide choice of pulse sequences [67]. For an explanation of the physics of these parameters see [85, 99, 146].

Because each combination of extrinsic parameters represents a tradeoff between the quality characteristics of an MR image, image acquisition protocols containing a series of different MR sequences are specifically designed for the analysis task at hand. In general, spin-echo (SE) sequences are used for good tissue contrast properties: white and gray matter are represented by their T1 and PD values, active tumor tissue with T1 images, and edema on T2 images. Gradient-recalled-echo (GRE) T1 sequences are used for obtaining a large number of images with high resolution from a volume as required for surgical planning and image processing, however sacrificing the contrast for resolution [67].

The appearance of tumor tissue may be improved by the application of contrast-enhancing agents. These drugs contain gadolinium, a paramagnetic metal ion that shortens the T1 signal in regions of blood-brain barrier breakdown [67]. The degree of enhancement is related to the level of the blood-brain barrier disruption and the related transport of the agent. Thus, the degree of enhancement is patient, tumor type and stage dependent [108].

2.3 Segmentation of Magnetic Resonance Images of the Brain

2.3.1 Introduction

Image segmentation has been defined as "the process that subdivides an image into its constituent parts or objects" [53], or "the decomposition of an image into natural units" [113].

For medical image analysis, the goal of segmentation is "to partition the original set of image points into subsets corresponding to meaningful anatomic structures", which may be particular tissue types (e.g. bone, white matter, gray matter, tumor), or functionally-identifiable structures (motor cortex, sensory cortex) [3]. This conversion may be accomplished by labeling individual voxels as belonging to a tissue class, by extracting volumes of connected voxels with common intensity responses, by extracting surfaces separating voxels with common responses, or by combinations of these steps.

Classification of Medical Image Segmentation Methods

For 2D image processing, several classifications of segmentation methods have been proposed which apply to 3D with the specification that regions are volumes and edges become surfaces [3]. Haralick and Shapiro state that "Image segmentation techniques are basically ad hoc and differ precisely in the way they emphasize one or more of the desired properties" [58]. Following Gonzalez and Wintz, "segmentation algorithms are generally based on two basic properties of gray-level values: discontinuity and similarity" [53]. Jähne divides segmentation approaches into "three basic concepts: pixel-based, edge-based and region-based" [68]. For medical image processing, segmentation methods have been categorized as follows [38, 72]:

- manual or operator controlled
- automated
  - data (i.e. intensity) driven
  - model or template driven

Operator controlled segmentation methods are based on superior human pattern recognition capabilities and prior clinical experience [38]. An interaction between an expert medical practitioner and the image analysis system is utilized. In this approach, the operator uses a graphical interface to apply basic segmentation methods such as thresholding (e.g. [88]), mathematical morphology operators [112], seeded region growing [1], or combinations of these [17, 62] and to draw borders of regions of interest, typically slice by slice through the 3D volume (e.g. [134]).

Signal intensity driven segmentation differentiates tissue types or structures based on their response to the medical imaging mechanism. Such methods are often statistical in nature, and usually rely on the operator defining the characteristics of each tissue class (e.g. the average response, represented by the intensity in the image), either as a statistical model [25, 48, 74, 133, 147, 148] or by identifying a small number of distinctive prototype voxels in the scan [25, 26]. These methods then classify the remaining voxels using e.g. nearest neighbor or k-means style classification [34, 42]. Alternative methods use edge detection (e.g. [113]) or other surface extraction methods such as deformable models (e.g. [95]) to directly define volume boundaries, by identifying transitions in intensity properties between neighboring but different anatomical regions.

Template driven segmentation methods utilize anatomical knowledge to guide the segmentation process. A common approach is to compare individual images to an anatomical atlas to define volumes of interest. Identifying structures based upon a priori knowledge and a presegmented anatomical map relies on the assumption that the individual brain image and the atlas template are in the same frame of reference. This can be achieved by non-linear spatial alignment procedures (commonly referred to as *registration*), that identify geometric differences and project the template onto the individual. [20, 30, 31, 36, 72, 141].

The remainder of this section aims to provide a survey of relevant recent literature concerning medical image segmentation of MRI and segmentation of brain tumors in particular. The material presented is heavily condensed and papers before 1995 are only referred to in "classic" cases. Later in this Chapter (Section 2.4) a description of current non-linear registration techniques is presented.

2.3.2 Signal Intensity Driven Segmentation with Statistical Classifiers

In the case of MR image data sets, statistical classification is the process of finding rules to map voxels intensity values onto different tissue types. The decision to classify a voxel as a certain tissue type is made in an n-dimensional *feature space*, with n being the number of imaging modalities available. The decision is based on prior knowledge of the combination of intensity values for different tissue types, which may form *clusters* in feature space. Thus, "the problem of classification is basically one of partitioning the feature space into regions, one region for each category" [34].

Statistical classification methods have been extensively investigated in medical image analysis literature. A thorough review of the theory of statistical classification methods may be found in [34, 42], a review of MR image segmentation techniques using statistical pattern recognition in [8].

The use of multi-channel statistical intensity classifiers for medical image segmentation was pioneered by Vannier *et al.* [133], describing the application of classification technology originally intended for the segmentation of remote sensing data

on MR image data and later used and extended by others. The application of both *supervised* and *unsupervised* methods have been described, which differ in that supervised methods require training data sets to identify each tissue type while unsupervised methods assign grey value response of tissues a general probability function (e.g. a gaussian). Training is usually provided by manual selection of prototype points in the image for each tissue type through a medical expert.

Vannier *et al.* conclude that supervised classification has a more important role in MRI analysis than in satellite image analysis because the classifier training by a radiologist is likely to provide more reliable prototypes as opposed to general probability distribution models.

Clarke *et al.* [24] report a comparison between supervised and unsupervised methods, highlighting that supervised methods are operator dependent and thus subject to variability of results, which has been measured to be relatively large. Unsupervised methods have the advantage of being operator-independent and clearly desirable from a viewpoint of reproducibility. However these methods may not result in meaningful segmentations and the quality of the results strongly depends upon the initialization of the algorithm. In a report on the stability of three classification techniques, the maximum likelihood (MLM), the k-nearest neighbor (kNN) classifier and a backpropagation artificial neural net (ANN), Clarke *et al.* [25] find the kNN method to be the most accurate and most stable, but also the slowest. Recently, algorithmical improvements have made kNN computationally feasible [140].

Common MR artifacts such as spatial inhomogeneities and partial volume effects and noise (see section 2.2.2) cause the MR response of a tissue to vary spatially, resulting in mis-classifications due to the global nature of the tissue model. Wells *et al.* [148, 149] have addressed the issue of intensity inhomogeneities in MRI with an Expectation-Maximization (EM) method which was later extended and refined by others [13, 51]. This method iterates between estimation of tissue class labels and estimation of the RF intensity inhomogeneity for tissue segmentation and correction of slowly varying intensity variations.

The effect of noise on the EM method has been addressed recently by extending the measurement model with a prior statistical neighborhood model, a Markov Random Field (MRF), which was introduced to image segmentation by Geman and Geman [46]. This prior model allows to incorporate information about the spatial homogeneity of tissue structure in a local neighborhood, so that the determination of the class of a pixel depends on the class of neighboring pixels. The algorithms presented by Held *et al.* and Kapur *et al.* show improved robustness to noise [61, 74]. The main problem of statistical classification of MRI are misclassifications due to overlapping intensity distributions of different tissue classes [140, 24].

2.3.3 Template Driven Segmentation

A different approach to segmenting medical images uses a priori anatomical knowledge. In this context, an anatomic atlas may represent the name and location of anatomic structures. By comparing the atlas with the individual data, volumes of interest or explicit structures can be located in the patient.

Comparing two different brains requires a mechanism for their integration into

the same spatial frame of reference, which is referred to as *registration*. The registration usually consists of two components, namely establishing a relationship between the reference and the patient specific data, and the subsequent projection of the atlas onto the patient data or vice versa.

Several groups have investigated the template based segmentation framework for the application to MR images of the brain. They basically differ in:

- the representation of the template anatomy in the digital atlas
- the frame of reference where datasets are compared
- the method of integrating the template information to generate a segmentation
- the method of alignment

Digital Brain Atlases

Much research has been directed towards the development of 3D-atlases of the human brain for several applications, e.g. as a guide in neurosurgical planning, as a template for segmentation, as a reference for quantitative comparison of brain architecture across different subjects, to locate functionally important structures (e.g. motory or sensory cortex) or for teaching purposes [37, 63, 81, 127]. The atlas from the groups of Evans *et al.* , Thompson *et al.* and Kikinis *et al.* have been used for the segmentation of patient brain images, which differ in the type of data source (MRI or histological slices) and the information provided (volumetric, surfaces or tissue probabilities).

Evans *et al.* [37] used MR images from 305 living normal subject to reach an average representation of human brain anatomy. For the purpose of averaging over different subjects, the 3D volumes were transformed into the *Talairach* system, a standardized stereotactic coordinate system for the human brain based upon common anatomical landmarks [119]. The (piecewise affine) transformation of 12 individual rectangular regions of brain aligns the anterior and posterior commissures and overall extrema. Subsequently, the transformed images are normalized and averaged on a voxel-by-voxel basis. The average intensity template provides a probability map for the location of anatomic structures.

Thompson *et al.* [127] also developed an average atlas on the basis of six normal subjects. However, they used digital images of thin histological slices of cadavers (*cryosectioning*) instead of MRI, providing improved image quality of 1024^2-2048^2 at a slice thickness of 20-50 μm, but, due to the sheer amount of image data, labeling of structures has just started. The images where mapped into Talairach space, and the brain boundaries outlined manually. This atlas holds a representation of the sulcal surfaces, which was constructed by mapping regular meshes onto each sulci and averaging over the six subjects, leading to a set of probabilistic measures for the variability of the human brain [127]. This atlas was later combined with MRI volumes of 10 normal subjects transformed into and averaged in Talairach space [126].

The atlas of Kikinis *et al.* [81] is based on volumetric MR images of a single normal living subject (256x256x124 resolution, 1.5 mm slice thickness). Instead of

adopting the Talairach system, the atlas is deformed to fit the individual brain. Using manual and semi-automatic segmentation techniques, volumetric label maps of currently app. 250 different structures of the brain were generated. This atlas is the most detailed in terms of the number of structures, and, because the imaging method is noninvasive and nondestructive, the subject may be reimaged for extension of the atlas (e.g. to add functional data).

Spatial Frame of Reference for the Comparison of Individuals

There are two ways of comparing different subjects:

- the individual is transformed into the Talairach stereotactic space
- the atlas is transformed to map the individual's anatomy

As for template based segmentation, the choice for a strategy depends on the choice of the atlas. Comparing to a population-based atlas in Talairach space has been used for the identification of otherwise not differentiable structures in MR images such as different sulci and gyri [28, 31], while a deformable atlas has been used to define volumes of interest such as white and gray matter to restrict a statistical classification scheme for MS lesions [140, 141].

While it is argued that population-based atlases better express the differences among individuals, the choice of the Talairach system as the "standard brain space" is considered problematic since the piecewise affine transformation may not be sufficient to describe inter-individual anatomic variability [129].

Spatial Alignment of a Brain Atlas

With a segmented digital atlas of the brain at hand, the question then becomes how the atlas and the patient are projected into the same frame of reference in order to compare the two. This presents a challenge, because wide inter-subject anatomical variations have been reported even among normals, such that neural structures differ in shape, size, orientation, topology and spatial relation to each other [124, 125]. In case of pathology, such as tumors, these variations are even more substantial, and above all, these structures do not exist in an anatomical atlas of a normal brain.

Due to the complex variability between individual brains, a linear transformation will fail to describe the differences appropriately. Instead, the transformation is better characterized as non-linear with a high degree of freedom, allowing for structures to deform in a non-linear fashion (i.e. shrink, grow, and twist), and to move or rotate locally and independently (e.g. [21, 28]).

The alignment of atlas and patient usually involves two steps, namely to establish the correspondence between two data sets, and subsequently to warp one dataset onto the other. To the present date, many different approaches for the task of non-linear registration have been proposed, varying in the coupling between data, the level of automation and the tissue deformation model. For illustrative purposes we shall remain in the context of atlas based segmentation framework and refer to Section 2.4 for a detailed review of relevant literature in the field of non-linear registration techniques.

Integration of Anatomical Models and Segmentation Processes

Once the match between the atlas data and the patient is established, different ways have been reported to use the anatomical information for the segmentation process.

- The matched atlas is used directly. Segmentation is achieved by looking up the corresponding tissue label in the atlas on a voxel-by-voxel basis [31, 36, 44].
- The matched atlas represents a probability map of structures in a standardized stereotactic space, incorporated as priors in a bayesian classification method [72, 155].
- The atlas is used as a mask to restrict a subsequent segmentation or classification scheme to regions of interest [66, 140, 141].
- The atlas is used as an additional feature channel with statistical classification, and classification and registration are iterated [139].

The direct use of an anatomic atlas accounts for the anatomic variability of human brains by deforming the atlas onto the patient. An atlas probability map collected in a standardized space accounts for anatomic variability by combining several subjects into one atlas. In the following, recent approaches with the template based framework are reviewed.

Application of Template Driven Segmentation to MR Images of the Brain

Initial work on the methodology of atlas based brain segmentation by Evans *et al.* [36] and later Collins *et al.* [31] used an atlas of 20 normal brains, averaged in Talairach space and manually outlined for 60 different structures. For registration, they use a combination of a linear and a non-linear matching step based on volumetric gray-value data and the gradient amplitudes and directions. The segmentation is reduced to a registration problem.

Kamber *et al.* [72] from the same group used an averaged probabilistic atlas in Talairach space, derived from 12 patients and segmented into white and gray matter, ventricle and external liquor (csf)[2] for the segmentation of multiple sclerosis (MS) lesions. In this illness, 95% of the lesions appear in white matter. This property is used by thresholding the probability of white matter to restrict a bayesian classification to a region of interest. They manage to reduce the false positive lesion by 56%-82%. Recently, Zijdenbos *et al.* [155] reported the use of a probabilistic atlas based on 300 patients in combination with a Talairach space registration method and a back-propagation artificial network (ANN), that uses three different MR modalities in conjunction with three probability maps of an anatomic atlas as input channels for the segmentation of MS lesions.

Gee *et al.* [44] have used a volumetric non-linear registration method based on Bajcsy *et al.* [4] for anatomical localization. Segmentation consisted of matching a one subject volumetric atlas containing 109 different structures. For the segmentation, the brain in CT, MRI or PET was manually outlined and contours matched to

[2]See appendix A for anatomical description

contours with an optical flow based approach. The outlines of anatomic structures in the matched atlas where directly transferred to delineate regions of interest.

Haller *et al.* [57] have used a single subject atlas in combination with an non-linear matching scheme based on fluid dynamics (Christensen *et al.* [21]) to segment the hippocampus.

Warfield *et al.* have reported the application of template based segmentation in patients with multiple sclerosis [140, 141]. In this approach, an optical flow scheme to match a single subject atlas to the patient was used to segment the brain from the head and subsequently gray matter from white matter. Then, the white matter area is masked out and a statistical classifier in combination with mathematical morphological operations is used to segment white matter lesions. This procedure has also been used to identify basal ganglia structures in the brain [66]. Recent work by this group has described an adaptive template based approach, where classification and registration are iterated [139]. The matched atlas is used as an additional feature channel to the statistical classification, and the segmentation is used for the registration of the atlas. This approach can segment normal and abnormal structures of different regions in the body.

2.3.4 Segmentation of Brain Tumors

Preliminary work applying conventional segmentation methods for tumor segmentation report limited success, often indicated by the lack of clinical validation studies. Approaches that operate on single MR acquisitions using thresholding and morphological operators [50], active contours [153] or neural networks [33, 154] work well in some cases but may not differentiate between active tumor, associated pathology and normal tissue, which requires the acquisition of several tissue parameters [70]. Especially active contour approaches need initialization close to the final boundary, which is difficult to automate due to the variability of shape and thus requires tedious manual interactions [123].

Clark *et al.* and later Velthuizen and Vaidyanathan from the same group apply multispectral classification methods to glioblastomas and astrocytomas [23, 103, 131, 132, 135]. Their validation work is notable, but at the same time reveals problems with overlapping intensity distributions, although these methods show improved results over the single channel methods. In a recent study, a classification method guided by anatomical knowledge was required for the automatic detection and segmentation of glioblastoma multiforme from a combination of T1-, T2- and proton density (PD) MRI with promising results [22]. However, anatomical knowledge is not individualised by using e.g. registration techniques.

2.4 Non-linear Registration of Medical Images

2.4.1 Introduction

The process of bringing two images into spatial alignment is referred to as *registration*. It usually consists of two steps, namely a) to establish the correspondence

between a (fixed) reference data set (e.g. the patient) and a template data set (e.g. an atlas), and b) the subsequent *projection* of the template onto the reference.

The representation of the correspondence between two images depends on the number of degrees of freedom (DOF) the correspondence model allows. Linear registration methods can be described using a constant matrix equation to express the spatial relationship between the coordinates of two volumes. They allow only a global translation and rotation in the *rigid* case, and additional global scaling and sheers in the *affine* case. The term *non-linear registration* applies to those methods that allow more than 9 DOF. In these cases, the geometric transform consists of a transform map, with either a linear transform for several independent compartments of the image or a translation vector for every voxel.

Registration methods are also characterized by the subjects that need to be aligned. *Intra-subject* registration aims at the alignment of e.g. several image modalities (e.g. CT and MR) taken from a single patient. Applications may be integrated visualization, follow-up studies over a longer period of time to evaluate therapy or disease process, or intraoperative registration, where anatomy has changed due to the surgical intervention. *Inter-subject* registration aligns data sets from different patients, for the characterization of shape differences between patients or with respect to an atlas of a normal brain, or for the definition of anatomical structures or segmentation. It has been found that a linear transformation is not sufficient neither for inter-subject registration nor to describe the changes seen in patients undergoing surgical procedures [28].

Approaches to non-linear registration of medical images may be characterized by the level of detail at which similarity is measured, i.e. comparison of corresponding

- points (point-based),
- surfaces (surface-based),
- the entire volume (volume-based)

Point-based methods rely on the information of corresponding anatomical landmarks (fiducials). Such approaches consist of a) identification of two sets of corresponding landmarks, which is usually done manually, and b) establishing the transformation between the data sets with an interpolating transformation model. The deformation is usually modeled by thin-plate splines, using the fiducials as control points. The landmarks form the search space of a minimization problem, where the energy function is a point-wise distance measure or similarity measure.

Surface-based methods establish correspondence through boundaries of objects, usually extracted manually or semi-automatically. The deformation is modeled by smoothly connected shapes originating from 3D-snakes. Approaches vary in the parametrization of the shape (e.g. Fourier-modes or Chen-surfaces) and the shape/elasticity constraints.

Volume-based methods work on a voxel-to-voxel basis. The deformation is modeled either as a rubber membrane (or ball/sponge in 3D) using optical-flow type

formulations, or as elastic/viscous-fluid objects using continuum-mechanics formulations. These methods differ in the feature domain (e.g. gray values, texture, edges, segmented object regions), the employed similarity measures (e.g. sum-of-squared-differences, cross-correlation, joint intensity distribution) and the way the model reflects actual physical properties of the image medium.

In the following, recent publications in each of these three groups will be illustrated. Global rigid and affine registration methods are not covered here. For extensive review and comparison of such techniques the reader is referred to e.g. [93, 151].

2.4.2 Point based Similarity Measure Methods

These methods use a set of corresponding anatomical markers (fiducials), which are usually placed interactively, to guide the registration process. In this framework, the fiducials are used as control points of thin-plate splines, that regularize or interpolate the deformation over the entire data set. Originally employed by Bookstein *et al.* for biological shape analysis [11], Kim *et al.* [82] combined this method with Mutual Information (MI), a statistical similarity measure based on joint entropy of two gray value data set. MI has been used and validated for the rigid registration of medical images from different modalities by Wells *et al.* and Collignon *et al.* [27, 137, 150]. Point-based methods are attractive for statistical description of shape differences. However, they require intensive operator interaction in order to properly select corresponding landmarks and have limited deformation capabilities, which are directly coupled to the number of control points.

2.4.3 Surface based Similarity Measure Methods

Several approaches have been published that use surfaces of objects to establish the correspondence between datasets. The basis of these methods is the deformable shape or snake method of Kass *et al.* [75] to model the deformation. A survey of these methods is presented in [94]. These approaches essentially use smooth connected data structures (contours in 2D and surfaces in 3D) coupled to an energy functional, which is a weighted sum of various terms to tradeoff faithfulness to the data and stretching and smoothing of the shape. The shape is deformed until a minimum state of energy is reached.

As to non-linear registration techniques, these methods usually involve several steps: The extraction of corresponding surfaces of interest, the derivation of a parametric representation of these surfaces, the establishment of the transformation that matches the surfaces, and, in case a volumetric match is desired, an interpolation of the surface transformation over the volume.

MacDonald *et al.* [91] used a polygonal model to represent the presegmented template surface. The transformation was estimated by minimizing a cost function in the domain of the vertex coordinates describing the polyhedra to be deformed. The objective function was a weighted sum of a data constraint, attracting the template to boundaries in the patient image, and several model terms to avoid

inter- and intra- surface intersection. Their method was used for template driven segmentation of the cortical brain surface.

Thompson *et al.* [124, 125, 126] include several surfaces (ventricles and cortex structures) to determine a match. The shapes were represented by a Chen-surface (loosely, a superquadric with spherical harmonics modulated onto it [125]). For extraction of the surfaces in the template and patient dataset, the shapes were initialized by manually identifying landmarks on the structures of interest, and subsequently refined by minimizing an energy formulation of a 3D-snake, which was attracted by a thresholded 1st order derivative edge image. Subsequently, surface displacement functions were established on parametric mesh representations of the surfaces, mapping points from the same grid location within their respective surface. These surfaces warps were then interpolated to form a displacement field over the whole volume. The method was applied mono- and multimodal (MRI to MRI and MRI to cryosection volumes).

The use of corresponding geometric features binds the mapping process closely to the underlying anatomy. Impressive results are achieved, especially in the mapping of cortical structures. However, these methods require significant manual interaction for the initialization of shapes, which is crucial to the performance of the algorithm. Another drawback is that some image information is partially neglected to the favor of surface descriptions.

2.4.4 Volume based Similarity Measure Methods

There are two main approaches to volumetric non-linear registration of medical images that have been pursued over the last 10 years: Optical flow based and continuum-mechanics based approaches. Both approaches may be integrated into the concept of regularization. The minimization of an energy formulation consisting of a local similarity measure between the data and constraints on the deformation field leads to the solution of the registration problem. Approaches in this domain essentially differ in

- the similarity measure: sum-of-squared-differences (SSD), normalized cross-correlation or joint-entropy measures
- data domain: gray values, derived features such as image gradients or distance maps of structures, or segmented images
- the regularization: none, 1st or 2nd order derivatives of the deformation field or both
- method of solution: jacobi relaxation or multi-grid methods with conjugate gradient relaxation of finite element discretizations

To use optical flow ("the distribution of apparent velocities of movement of brightness patterns in an image" [64]) for image registration, the template image can be seen as the second instance of the scene represented in the target image. The optical flow field then represents the shape differences between objects. The optical flow is then applied to the image, where the flow vectors are used as translation

vectors. Optical flow estimation and subsequent deformation of the template image is iterated until a match with the target is achieved.

Many different formulations appeared and continue to appear. From the several optical flow paradigms (see Barron *et al.* [7, 6] for an overview) the *matching* techniques have been investigated for medical image registration [28, 31, 141]. The advantages of these approaches are i) that they do not require temporal derivatives, which is numerically problematic with only two image instances, and ii) the generality of the correlation type similarity measure, which allows the use of image features.

In optical-flow methods, displacement vectors are assumed to be small, which is not correct in medical images. This results from linear approximations made to reach a formulation that is faster to solve. These shortcomings have been addressed by solving the registration in two steps: i) solving for global translations and rotations prior to the non-linear registration and ii) embedding optical flow into a multi-resolution pyramid with a coarse-to-fine strategy.

A different approach is the application of methods originated in continuum-mechanics modeling [5, 15, 19, 21]. Here, the template is given properties of an elastic or viscous-fluid material. External and internal forces compete in a deformation process until a state of equilibrium is reached. External forces are measured with local similarity functions between patient and template images. Internal forces such as shear and viscous stress are expressed through 1st and 2nd order derivatives of the deformation field. Unlike optical flow methods, the constraints on the deformation field are based on actual physical properties. However, these methods substantially increase the computation time due to the increased complexity of the model.

Optical Flow Methods

Region-based methods define velocity/displacement as the set of regional translations that achieve the best image match [7]. Solutions are computed by maximizing an integrated similarity measure locally over the subdivided images, which is regularized with constraints on the deformation field.

Collins *et al.* [31] applied a multi–resolution matching technique in combination with a rigid alignment step to account for global translational and rotational offsets prior to non-linear registration. The normalized cross-correlation gradient magnitude and direction of the grey values over a local neighborhood was chosen to measure similarity. The best match was found by optimizing three translation parameters for each node of a regularly meshed grid. No global regularization was used, instead a threshold was applied to prevent unrealistically large deformations. Validation was carried out in a similar fashion to Gee *et al.* . A phantom was artificially deformed and the algorithm applied to fit the original to the deformed version. Performance was measured with the root-mean-squared distance between 296 landmarks, resulting in an average mismatch of 6.41 mm. In a later evaluation study based on MRI of real brains with simulated deformations [28], reasonable overlap between deep brain structures were reported, but sulci and gyri matched insufficiently. In a recent publication, Collins *et al.* [29] improved his method by adding cortical constraints to the model. Different sulci and gyri were identified

semi-automatically to partially solve the correspondence problem prior to the registration and represented as Chamfer distance functions.

Warfield *et al.* [140, 141] used a technique developed by Dengler *et al.* [32] to register an atlas to patients. The method is essentially a multi-resolution region-based optical flow scheme using an SSD similarity measure and a global regularization of the deformation field with 1st order derivatives. Instead of applying the method directly to the gray value data, corresponding structures were segmented, which significantly improved the robustness of the match. More recent work of this group [66, 77, 139] used a more rigorous approximation by calculating the deformation field in small image patches instead of using a regularization for improved computational performance.

Continuum Mechanics Methods

The continuum mechanics approach differs from optical flow methods in its motivation. Some investigators have described methods of brain registration across individuals where the template is embedded in a deformable medium with elastic [4, 5, 15, 96] or viscous-fluid [19, 21] properties. The template medium is subject to external an internal forces, which deform the template until the involved forces reach a state of equilibrium. The deformation field is described by a simplified version of the Navier-Stokes equations.

The idea of using an elastic model for the registration of CT images was pioneered by Broit *et al.* [15]. A normalized cross-correlation similarity measure with a global 1st order regularization was chosen, leading to the model of the simple membrane. Bajcsy and Kovacic [5, 4] from the same group refined this method by implementing a multiresolution version in a coarse-to-fine strategy, that allows to capture larger shape disparities on coarse levels. In order to discretize the model equations, linear Taylor approximations were made and finite difference approximation led to a large system of linear equations which was solved with Jacobi iterations. Bajcsy *et al.* applied their method to manually outlined CT, MR and PET data, using the boundaries of structures as features. In a validation study of this technique, Gee and Bajcsy [44, 45] derived an atlas of 109 structures by manually outlining 135 sections from a postmortem young normal brain. To assess the performance of the algorithm, the atlas was matched to several artificially deformed versions of itself. The resulting volumetric percent difference was 6 %, and the mean overlap error was 22%.

In Christensen *et al.* [19], the external forces are derived from a local normalized cross-correlation function applied to the gray values. The internal forces express viscous shear and stress, and increase with the deformation. The non-linear deformation force is evaluated without approximation, thus allowing large, non-linear deformations. This leads to impressive results in the registration of brain data sets across individuals. However, the solution on a finite spatial grid using successive over-relaxation leads to extensive computation times (9 hours on a massively parallel supercomputer for the registration of two 128x128x148 volumes).

Some work has been conducted to improve the computational performance of Christensen's approach. Bro-Nielsen *et al.* [14] present a fast algorithm for the

solution of the Navier-Stokes equations based entirely on convolutions, achieving a speed improvement of an order of magnitude.

Until now, volume based methods are the only type of non-linear registration techniques that do not require manual interaction. However, the establishment of correspondence is often based either i) on intensity data alone and thus subject to imaging artifacts or differences in the representation of tissue types across images, or ii) on segmented data and thus subject to segmentation errors.

Discontinuities in the Deformation Field

At the present time, non-linear registration methods assume a smooth deformation field and one-to-one correspondence. The assumption of a smooth deformation field is violated at the boundary of objects which move and deform independently. The assumption of one-to-one correspondence is violated if template and target are not topologically equivalent.

The problem of accommodating discontinuities in a deformation field has been studied in the field of reconstructing 3D surfaces from 2D images. When a 3D surface is to be estimated from an image of multiple objects, discontinuities must be present between the different objects. Terzopolous *et al.* [120] reported a surface reconstruction method based on the membrane model that is able to generate smooth surface representations between discontinuities, and at known depth discontinuities, the smoothness functional is deactivated, allowing the reconstructed surface to "fracture" locally.

However, the introduction of such energies makes the computation of flow field difficult, because the minimization problem is now non-convex, i.e. has several local energy minima [10]. Stochastic relaxation methods (e.g. simulated annealing) that are suitable for the solution of non-convex problems are known to be slow [10, 105]. Thus, several attempts have been made to speed up the computation; finite element modeling and the use of multi-grid techniques [121, 122], approximation of the non-convex functional with a convex functional [10]. Schmidt and Dengler propose a decoupling of the discontinuity detection from the deformation field estimation, leading to a significant improvement of the computational performance [32, 111]. In this approach, an optical flow criterion was regularized with a controlled continuity function to allow local control of the degree of regularization applied by the membrane through the use of a scaling of the membrane deformation energy. This approach was successful in tracking moving objects with a continuity controlled regularization of optical flow estimates.

2.5 Conclusion

Significance of Automatic Segmentation Methods Many applications of computer assisted surgery and radiology require the segmentation of normal and abnormal tissue in MRI images of patients with brain tumors. Manual segmentation is usually not clinically practical, and the accurate, robust and reliable automated segmentation of MRI of brain tumors is still an unsolved problem.

Choice of a Segmentation Framework Correct segmentation of MRI of brain tumors based on intensity values alone is not possible due to overlapping grey value distributions of different tissue classes. Similarly, segmentation based on the registration of a normal atlas is capable of identifying structures despite ambiguous intensity distributions, but is limited to the segmentation of normal structures. In these aspects, these two techniques are complementary. Their combination is a promising approach to exploit the advantages of both methods.

Non-linear Registration for Template based Segmentation Automated template based segmentation requires automatic non-linear registration. Currently, only the volumetric approaches are fully automatic.

The problems of segmentation and registration are strongly related:

- Structures with similar or identical (grey value) image characteristics can be segmented with the registration of an anatomical atlas. For example, information such as "there is no skin inside the brain" can be utilized to prevent brain tissue being segmented as skin and vice versa, despite considerable overlap of intensity distribution.

- Registration cannot rely exclusively on the raw MRI data. State of the art surface based registration methods require the identification and description of surfaces. Volumetric techniques interpret any change in intensity as deformation or movement. This results in registration errors, if intensity differences resulting from different modality, noise, or imaging artifacts, do not relate to object diffferences. Registration based on segmented images conserves brightness, and is more robust to noise.

- Registration errors result in segmentation errors and vice versa.

Some of the limitations of current sate of the art registration methods are

- Current non-linear registration methods assume one-to-one correspondence, i.e. topological equivalence. This is not true for large intrinsic tumors.

- The deformation field is assumed to be smooth. However, registration of multiple objects moving or deforming independently may cause discontinuities.

- Current registration methods assume correct segmentations, such that segmentation errors lead to registration errors.

This review of the current state of the art shows, that several methods for the segmentation and registration of medical images exist, each of them with some limitations. The next chapter proposes our strategy to overcome some of these problems.

Chapter 3

Outline and Original Contributions

Goals of this work

The goal of this work is to develop algorithms for the automated segmentation of normal and pathological tissue of MRI of patients with brain tumors. The specific objectives of this work are a) to develop a method based on the integration of statistical classification and nonlinear registration, in which context from a digital brain atlas is used to moderate classification, and b) to extend the range of conditions under which nonlinear registration methods can operate successfully to improve the performance of template moderated segmentation methods.

Methological Overview

Statistical classification technology is based on the intensity information in an image and has been used for the segmentation into global tissue classes. Because normal and tumor tissue classes have the same or overlapping grey value distributions (Section 4.1), such methods fail. Similarly, segmentation by registration of explicit anatomical templates has been successfully applied to identify normal anatomical structures, but may fail in the presence of highly variable brain tumors (Section 4.1).

The **segmentation paradigm** chosen in this work is called adaptive template moderated classification (ATMC), which integrates these two separarate approaches to segmentation [139]. Figure 3.1 illustrates the concept of the framework. The algorithm involves the iteration of a) classification of the patient data set to assign labels to tissue types, and b) nonlinear registration to spatially adapt (align, register) the anatomical templates of a digital atlas to match the individual. The tissue labels are computed with a statistical classification algorithm which is moderated by the aligned anatomical template. As the computation progresses, the alignment is refined by iteration of nonlinear registration and tissue classification. The tissue classification makes the nonlinear registration more robust, and the aligned templates improves the ability of the tissue classification to discriminate different structures with similar image acquisition characteristics. In Chapter 4, the details

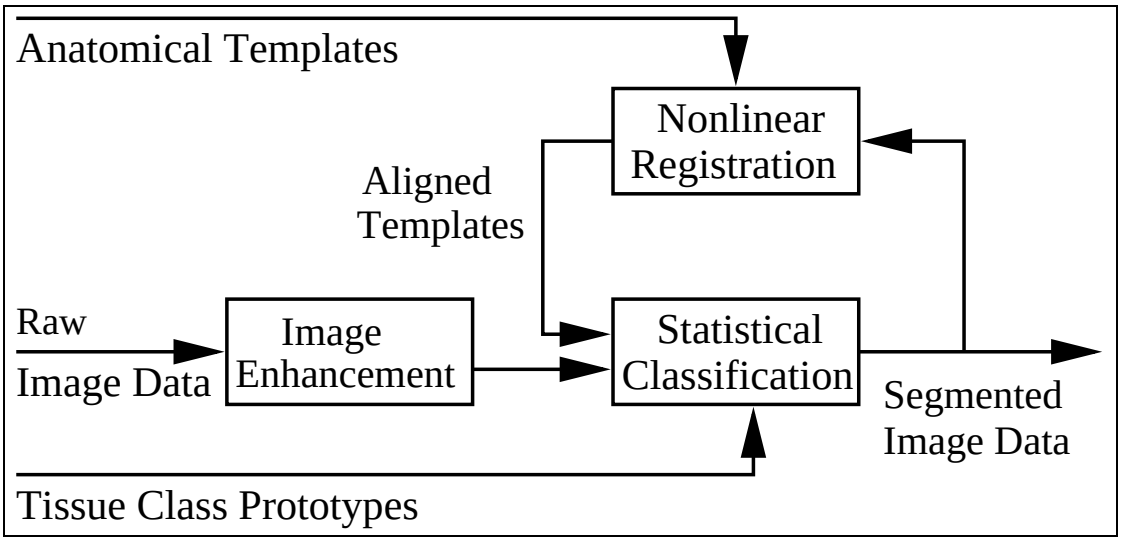

Figure 3.1: **Schematic description of the adaptive template moderated classification (ATMC) paradigm.** *Statistical classification and registration of an anatomical atlas are iterated to resolve ambiguities resulting from overlapping intensity distributions of tissue classes.*

of the method and the design for the specific task of brain tumor segmentation is discussed in detail.

The **nonlinear registration technique** used in the context of the brain tumor segmentation method developed in this work is based on an existing optical flow algorithm. This method works under a set of assumptions that does not model well the image data and the deformation of the structures to which they apply. These assumptions include the correctness of the underlying segmentation and the continuity of nonlinear deformations. In Chapter 5, the performance of several approaches to nonlinear registration are compared in terms of accuracy, robustness and computational requirements. An extension to existing methods is developed, that a) takes into account the probability of the segmentation, and b) allows discontinuous deformation fields commonly found in images where several objects deform or move independently.

In Chapter 6, the methods developed in this thesis are investigated and validated based on synthetic images and databases of clinical image data.

Original Contributions

- Implementation of an optical flow approach with adaptive regularization in 3D. The method aims at the estimation of discontinuous deformation fields resulting from the movement or deformation of multiple independent objects. The algorithm extends an existing 2D optical flow approach. A multigrid algorithm for the numerical solution of the 3D optical flow equations is designed.

- Comparison of the developed adaptive regularization method with a fast state of the art template matching approach. Identification of the difficulties of both

methods regarding the registration of segmented images of multiple objects.

- Development of a multi-channel probabilistic similarity measure to improve the registration of multiple objects in segmented images.
- Comparison and validation of a sum-of-squared difference and the new multi-channel probabilistic similarity measure to match a digital brain atlas to individual MRI datasets, demonstrating a higher accuracy using the probabilistic similarity measure.
- Identification of spatial and signal intensity characteristics of meningiomas and low grade gliomas in spin-echo MRI relevant to the design of automated image segmentation methods.
- Design and application of a method for the automated segmentation of the skin surface, the brain, the ventricles and the tumor in gradient echo MRI images of patients with brain tumors. The algorithm extends an existing template based segmentation framework that combines statistical classification and anatomical knowledge.
- Validation of the segmentation method for the tumor types meningiomas and low grade gliomas based on comparison with manual segmentations from trained medical experts, showing comparable accuracy and higher reproducibility of the automated method.
- Development of a method for the automated projection of functional structures from an anatomical normal brain atlas onto patients with brain tumors.

In the following chapters, the methods outlined here will be discussed in detail. While the methods presented here operate in 3D, in some cases, the performance of an algorithm was better illustrated by showing 2D cross-sections through the 3D MRI volume rather than a pseudo-3D representation.

Chapter 4

Segmentation of MRI of Brain Tumors

In this chapter, the development of a method for the automated segmentation of normal and pathologic tissue in patients with brain tumors is described. After an analysis of meningiomas and low grade gliomas in MRI (Section 4.1) with respect to the task of designing an automated image segmentation method, the general segmentation framework is presented in detail (Section 4.2), the specific design of the framework for brain tumor segmentation [77, 78] is derived (Section 4.3), and illustrative results from the application of the method to clinical MRI datasets are presented (Section 4.4).

Although non-linear registration is an important element of the segmentation method developed in this chapter, the registration algorithm used is treated as a black box. The analysis and development of registration methods is discussed in Chapter 5.

4.1 Appearance of Brain Tumors in MRI

4.1.1 Brain Tumors in MRI

Medical imaging as well as object specific properties make segmentation of brain tumors difficult. Image intrinsic factors (Section 2.2.2) cause segmentation errors, because the MR characteristics of a tissue type are mis-represented. Examples are fuzzy or blurred boundaries, or tissue appearance changing with the location. These artifacts pose a general problem to any kind of segmentation.

For tumor segmentation, additional object related issues arise from the nature and the appearance of brain tumors in MRI. A tumor is a complex object with virtually arbitrary

- histology (e.g. meningioma, low grade glioma)
- size, shape, location
- tumor composition (e.g. enhancing and non-enhancing tumor tissue, edema, necrosis, cystic parts)

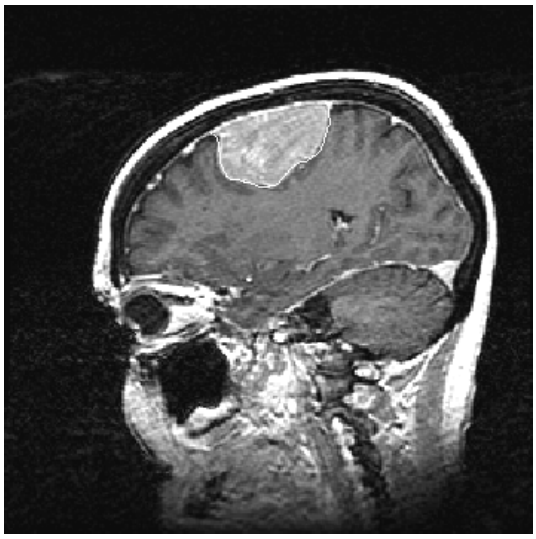

(a) MRI Cross-section of a Meningioma

(b) MRI Cross-section of a Meningioma

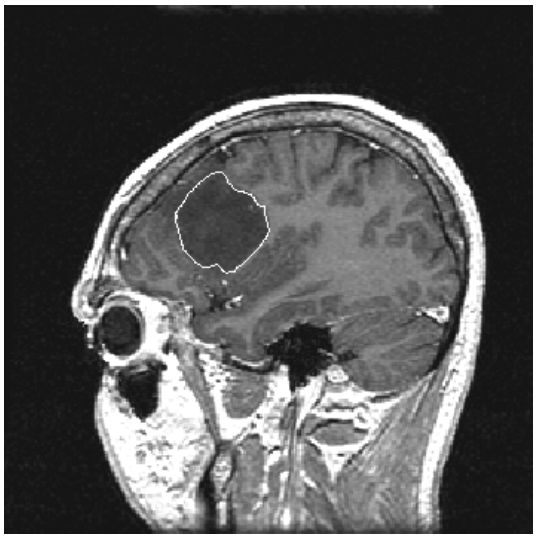

(c) MRI Cross-section of a Low grade glioma

(d) MRI Cross-section of a Low grade glioma

Figure 4.1: **Examples for some of the most common brain tumors.** *Tumors (white outline) may appear in virtually arbitrary shape, size, and location. They show large variation in terms of MRI intensity, tissue composition and degree of homogeneity [152].*

- degree of tissue composition (homogeneity, texture)

Figure 4.1 shows typical examples of meningiomas and low grade gliomas imaged with a T1-weighted SPGR sequence (see below). These tumors are relatively homogeneous and have well defined imaging characteristics [152]. Meningiomas are high in intensity because they enhance well with the application of contrast agent, and have well defined boundaries. Low grade gliomas, in contrast, are low in in-

tensity because they do not enhance well with the application of contrast agent, and boundaries to the brain are difficult to detect. In the presence of edema, it is usually difficult to separate tumor from edema with T1 images only, and additional T2 images are necessary to distinguish between edema and tumor.

In an in vivo study of 160 tumor patients on tissue characterization with calculated T1, T2 and Proton Density values, Just *et al.* report large variations in the gray value distribution across patients with the same tumor type and considerable overlap of gray value distribution both among different tumor types and with normal tissue [70, 71]. They conclude that MR tissue parameters have only limited value in characterizing and discriminating brain tumor tissue. However, they acknowledge that limiting their measurements to single-exponential T1 and T2 decay due to time constraints in a clinical setting results in a measuring error of 6%-12% and reduces the specificity.

Schad *et al.* analyze 12 tumor patients with glioblastoma multiforme or metastasis on the basis of first- and second- order image texture parameters [109]. They state, that quantitative measures of brightness, micro- and macrotexture may improve the discrimination accuracy over the use of MR parameters only, however neither discrimination between the different tumor types nor between the tumor tissues (e.g. edema and active tumor tissue) is reliable. In a similar but more extensive study on 88 tumor cases, Kjaer *et al.* [83] report satisfactory discrimination by means of texture analysis. However, mean values over regions have to be used, as discrimination power is not satisfactory on a voxel level.

The high variability of brain tumors and their appearance is demonstrated in a report by Roßmanith *et al.* [107]. For the purpose of characterization and classification of (manually segmented) brain tumors for diagnostic aid, they find that the combination of several features is necessary, including shape description, fractal features of the contours and texture analysis.

4.1.2 Brain Tumors in MRI for 3D Model Generation

Image Acquisition Optimization of the image acquisition protocol is usually necessary for automated image segmentation. The better the design of an imaging protocol for a specific image analysis task, the simpler the task of segmentation, and the better the results.

For surgical planning, high image resolution is necessary for the generation of accurate 3D models. The MRI sequence used in this work optimizes the tradeoff between resolution, contrast to noise and scanning time. Heads where imaged in the sagittal and axial plane with a 1.5 T system (Signa, GE Medical Systems, Milwaukee, WI).

- A 3D sagittal spoiled gradient recalled (SPGR) acquisition with contiguous slices after gadolinium-enhancement (flip angle, 45°; repetition time (TR), 35 msec; echo time (TE), 7 msec; field of view, 240 mm; slice-thickness, 1.5 mm; 256× 256 × 124 matrix).

Image Intensity Distribution In order to illustrate the spectral properties of normal and abnormal tissue in the human head, examples of SPGR images of a

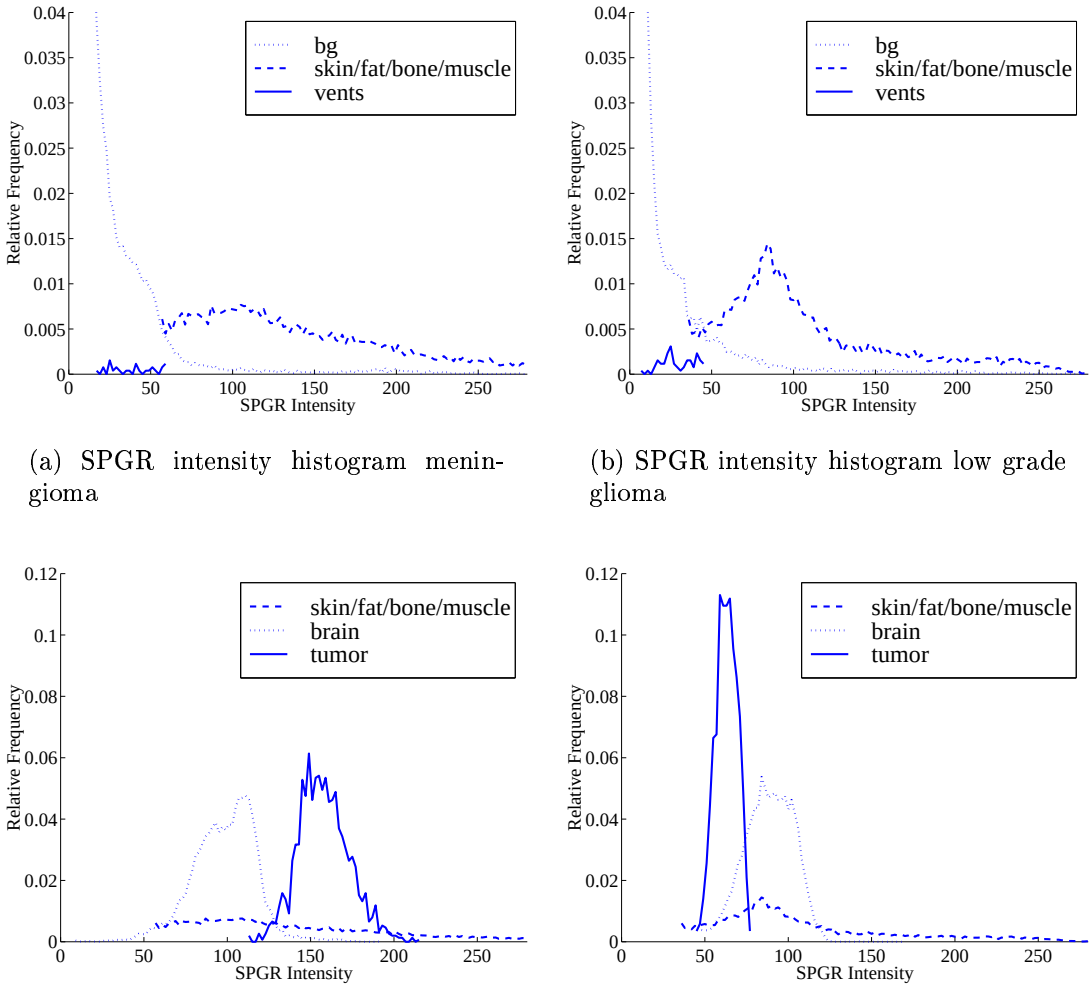

(a) SPGR intensity histogram meningioma

(b) SPGR intensity histogram low grade glioma

(c) SPGR intensity histogram meningioma

(d) SPGR intensity histogram low grade glioma

Figure 4.2: **Histogram of MRI intensity distributions of a meningioma (a,c) and a low grade glioma (b,d).** *Histograms were assessed by masking the MR images in Figure 4.1 (a), (c) with manual segmentations. The tissue classes cannot be separated based on intensity values alone, due to overlapping intensity distributions.*

meningioma (Figure 4.1 (a)) and a low grade (Figure 4.1 (c)) glioma were manually segmented into the structures *brain*, *ventricles*, *tumor*, and *skin*. Skin comprises all voxels of the head that do not belong to brain, ventricles, or tumor. This means the skin class also contains e.g. fat, bone and bone marrow, and muscles. The segmentation was used to mask out each structure in the SPGR image, and the frequencies of the occurring intensity values were recorded (Figure 4.2).

The skin class is evenly distributed over the higher range of intensities, overlapping with all classes except the ventricles. The peak in the skin distribution (glioma case (b)) results from a larger part of muscle in the neck. The sudden drop of the ventricle and skin class distributions ((a), (b)) reflect the definition of the skin class.

Both images demonstrate the problem of intensity overlap between different tissue classes. No tissue class is free of intensity distribution overlap. As for the tumor tissue, the meningioma class overlaps with the skin class, while the low grade glioma class overlaps with the skin and the brain class (mainly the outer cortex).

4.2 ATMC - Adaptive Template Moderated Classification

The core of the method is a closed loop of two algorithms that are carried out iteratively: A traditional multi-channel statistical classifier and a non-linear registration method (see Figure 3.1).

The global separation of tissue classes is achieved with a statistical multi-channel classification algorithm. To improve separation and clustering of the feature space, knowledge about the location of structures derived from an anatomical atlas is integrated into the classification process. This is achieved by embedding the classification problem into a higher dimensionality feature space, where additional dimensionality is derived from anatomical templates, i.e. structures from a digital atlas. By adding anatomical knowledge to the classification process, the spectral information in the image is augmented with spatial information. In the common case involving some spectral overlap between tissue classes, the ATMC resolves the ambiguity of the feature space with anatomical context, i.e. with additional feature channels derived from the atlas.

To use anatomical templates in a statistical classification context, two steps are necessary: the atlas and the individual need to be spatially aligned, and anatomical knowledge needs to be represented in a statistical context.

The spatial relationship is usually non-linear in nature. In this work, the registration is established with an optical-flow based approach. The spatial relationship is computed based on labeled images classified during the iteration rather than on the original grey value images. This makes the optical flow algorithm more robust to image noise and intensity artifacts. Several issues arising from the use of labeled images with an optical flow approach are discussed in detail in Chapter 5.

Anatomical knowledge is represented by converting the anatomical templates into distance maps. Qualitatively, the ordering of the feature space is altered according to the certainty of membership to a template structure. This means, that two voxels move closer together in feature space if they are located in the same structure according to the atlas, and move further apart in feature space if they are located in different structures. The certainty about the correctness of anatomical localization derived from the atlas is modeled with the distance to a template. This is motivated by the fact that the registration result is usually more prone to error at the boundaries of a structure.

Classification and registration are repeated in several iterations. Ideally, the aligned templates improve the classification result, and improved classification results improve the alignment, until no further change of the segmentation result between iterations is reached or the registered atlas templates match the classification results.

4.2.1 The k-Nearest Neighbor Algorithm

The task of statistical classification is to subdivide the feature space into regions, one region for every tissue class. In multispectral MRI, the feature space represents the distribution of the intensity responses. The k-nearest neighbor (kNN) rule is a supervised, non-parametric pattern classification method. The mapping of a voxel onto one of different tissue classes is made according to the voxels location in feature space. Let the D-dimensional volumetric image

$$\mathbf{V}(\mathbf{x}) = \{\mathbf{v}(\mathbf{x}_1), \ldots, \mathbf{v}(\mathbf{x}_N)\} \quad , \tag{4.1}$$

N being the number of voxels, with patterns

$$\mathbf{v}(\mathbf{x}_i) = \mathbf{v}_i = [v_i^1, \ldots, v_i^D]^T \quad \text{with} \quad v_i^l = I^l(\mathbf{x}_i) \quad , \tag{4.2}$$

D being the number of image channels and v_i^l representing the grey value of the l-th image volume I^l of the multispectral MRI at location $\mathbf{x}_i = [x, y, z]^T$, and $i = z * y_{\max} * x_{\max} + y * x_{\max} + x$ the indexing according to row-major ordering. Given a set of training prototype vectors

$$\mathbf{W} = \{\mathbf{w}_1, \mathbf{w}_2, ..., \mathbf{w}_M\} \quad , \tag{4.3}$$

and the correct classification for each prototype in one of the C classes $c_1, c_2, ..., c_C$. According to the kNN rule, a voxel $\mathbf{x}_i$ with the pattern $\mathbf{v}_i$ of unknown class is classified as class c_i, if most of the k closest prototypes are from class c_i [34]. The distance metric used here is euclidian, i.e.

$$\begin{aligned} d(\mathbf{v}_i, \mathbf{w}_j) &= \|\|\mathbf{v}_i - \mathbf{w}_j\|\| \\ &= \sqrt{(\mathbf{v}_i - \mathbf{w}_j)^T(\mathbf{v}_i - \mathbf{w}_j)} \\ &= \sqrt{\sum_{l=1}^{D} (v_i^l - w_j^l)^2} \end{aligned} \tag{4.4}$$

describes the distance between the pattern feature vector $\mathbf{v}_i$ and the prototype feature vector $\mathbf{w}_i$.

As for the probabilistic view, let $\bar{\mathbf{W}} \subset \mathbf{W}$ be the subset of the k nearest prototypes. An estimate of the joint probability is

$$p(\mathbf{v}_i, c_i) = \frac{k_i}{NV} \quad , \tag{4.5}$$

with k_i being the number of prototypes p_i belonging to class c_i and V the volume that encloses all k prototypes. Then an estimate for the a posteriori probabilities $P(c_i|\mathbf{v}_i)$ is

$$P(c_i|\mathbf{v}_i) = \frac{p(\mathbf{v}_i, c_i)}{\sum_{j=1}^{C} p(\mathbf{v}_i, c_j)} = \frac{k_i}{k} \quad , \tag{4.6}$$

and the decision is made according to $\max_i\{P(c_i|\mathbf{v}_i)\}$.

4.2.2 Integration of Anatomical Knowledge and Statistical Classification

Statistical classification leads to erroneous decisions if tissue classes overlap in grey value distribution. To resolve such ambiguities, a presegmented anatomical brain atlas can be used as a template to interact with the classification process. Since brains differ considerably across individuals in size, shape and location, a non-linear alignment method is required to establish a one-to-one mapping of the template onto the individual

$$T(\mathbf{x}) : \mathbf{V_a}(\mathbf{x}) \rightarrow \mathbf{V_i}(\mathbf{x}) \quad , \tag{4.7}$$

with $\mathbf{V_a}$ being the atlas image and $\mathbf{V_i}$ the image of the individual (see chapter 5 for details).

If the template were perfectly aligned with the atlas, it could be used directly, and no further classification would be necessary. However, correct alignment cant be assumed, since the transform T is subject to error too. Thus, anatomical knowledge of a approximately registered template should be expressed with some degree of confidence in the spatial correctness of anatomical knowledge, suggesting a formulation in a statistical context. Essentially, the computation of the distance to prototypes is modified in a way that reflects the confidence in its spatial location.

The kNN classifier from the previous section may be used with an arbitrary number of feature channels. Provided a representation for a certainty map of anatomical localization from aligned templates, anatomical knowledge can be expressed in terms of additional feature channels. Equation (4.4) becomes

$$d(\mathbf{v}_i, \mathbf{w}_j) = \sqrt{\sum_{l=1}^{D} (v_i^l - w_j^l)^2 + \sum_{m=1}^{A} (v_i^m - w_j^m)^2} \quad , \tag{4.8}$$

where A is the number of anatomical channels added, one channel per anatomical structure, and $(v_i^m - w_j^m)$ represents the difference in anatomical localization between the voxel to be classified and the prototype. The classification problem is transformed into a higher dimensional space, leading to a new ordering of the feature space.

Figure 4.3 shows an example in case of a single aligned template (note that any number of templates may be used). Given an approximately aligned anatomical brain template, the distance measure in Equation (4.8) becomes

$$d = \sqrt{\sum_{l=1}^{D} (v_i^l - w_j^l)^2 + (d^2_{v,\text{brain}} - d^2_{w,\text{brain}})} \quad , \tag{4.9}$$

where $d^2_{v/w,\text{brain}}$ represent the certainty of membership to the brain at the location of the voxel and prototype in the image.

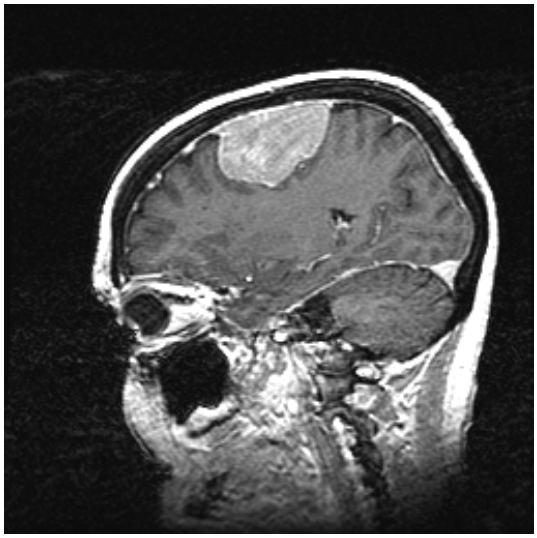

(a) Cross-section of 3D MRI of a tumor patient

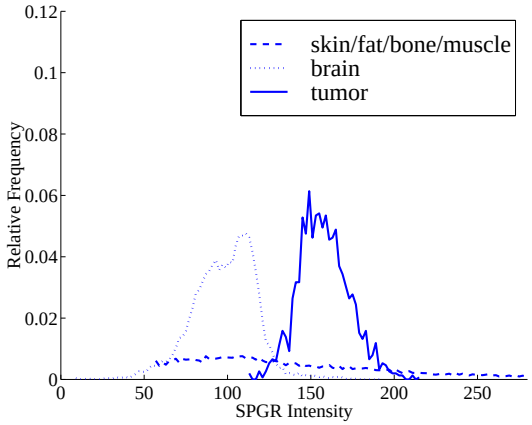

(b) Histogram: intensity of the MRI volume

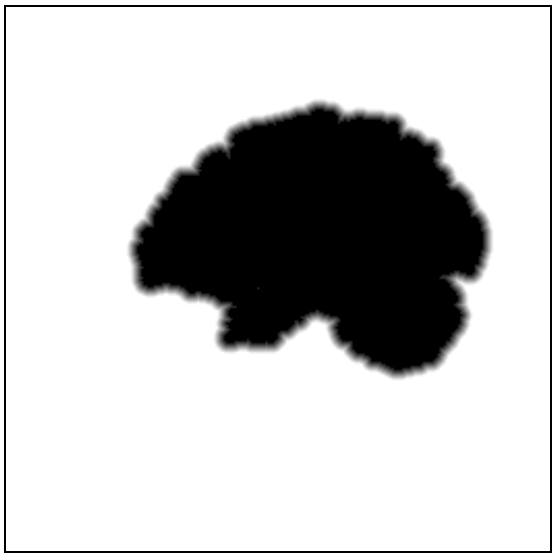

(c) Saturated distance transform of the intra-cranial cavity (ICC) template of the aligned atlas (distance corresponds to intensity, i.e. black is 0 distance)

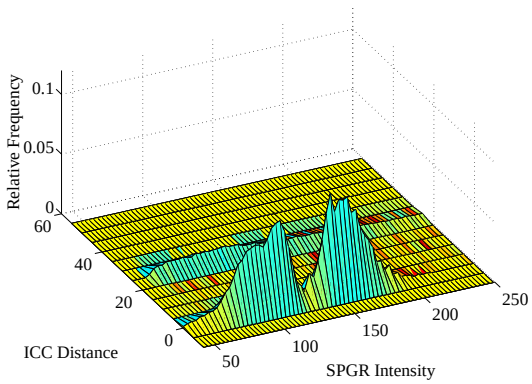

(d) Histogram: intensity vs. spatial distance to atlas

Figure 4.3: **Illustration of the change in feature space with the integration of anatomical knowledge.** *The feature space was recorded from a 3D MRI volume of a head with a meningioma (a). The intensity distributions of skin, brain and tumor overlap (b). An additional anatomical feature channel extracted from the registered atlas ((c), 2D slice from same plane as in (a)) increases the separability between the tissue classes in the 2D feature space (d).*

Three basic cases may be distinguished:

- $(\mathbf{w}_j \text{ xor } \mathbf{v}_i) \notin \text{brain} \rightarrow (d^2_{v,\text{brain}} - d^2_{w,\text{brain}}) = \infty$, making $\mathbf{w}_j$ a very distant neighbor
- $(\mathbf{w}_j \text{ and } \mathbf{v}_i) \in \text{brain} \rightarrow (d^2_{v,\text{brain}} - d^2_{w,\text{brain}}) = 0$, classification relying on the D image features only
- $(\mathbf{w}_j \text{ and } \mathbf{v}_i) \notin \text{brain} \rightarrow (d^2_{v,\text{brain}} - d^2_{w,\text{brain}}) = 0$, classification relying on the D image features only

Thus, if voxel and prototype are located in the same anatomical structure suggested by the aligned atlas, the classification relies on the spectral information alone. If they are located in different structures, the distance between the feature vectors is large.

4.2.3 Model of Anatomical Localization

The alignment of the anatomical templates usually requires several iterations, especially in the case of large shape differences between atlas and patient due to pathologic tissue. This means, that the accuracy of anatomical localization changes in the course of the segmentation process. Thus, a range of confidence in the anatomical localization should be considered, which is directly related to the spatial alignment error.

The alignment error of anatomical templates is usually low inside the structure and higher at the boundaries. A straightforward model of error is to use a penalty of $d_{v/w,\text{brain}} = 0$ where labels for the matched template are present, and increase the penalty with distance from the anatomical template. The certainty values can be efficiently estimated by computing distance transforms which approximate the euclidian distance (here: 3D-Chamfer (3,4,5), see [12]) for each of the structures in the aligned atlas.

The distance transform volumes can be used as additional feature channels for the kNN classifier. Let dist() be the distance function operation on an image, then the overall feature space distance metric Equation (4.8) becomes

$$d(\mathbf{v}_i, \mathbf{w}_j) = \sqrt{\sum_{l=1}^{D} (v_i^l - w_j^l)^2 + \sum_{m=1}^{A} (\text{dist}(T(v_i^m)) - \text{dist}(T(w_j^m)))^2} \quad , \qquad (4.10)$$

where T is the transform that maps the atlas onto the template (see Equation (4.7)).

To model uncertainty in anatomical localization approaching the boundary of a structure from the inside as well as from the outside the boundary of the templates, anatomical localization for each template is represented with two distance transform maps. One describes the distance to the structure, with the effect of increasing the penalty away from the structure. The other describes the distance to the background of the structure, with the effect of increasing the penalty towards the inside of the structure.

Two parameters define the anatomical localization, a saturation value and the function operating on the distance maps to derive the classification penalty:

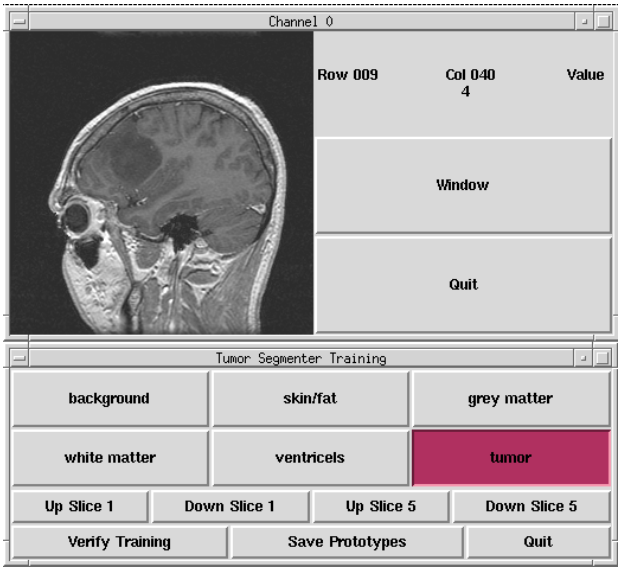

Figure 4.4: **User interface for the selection of tissue class prototypes.** *The automated segmentation method requires the physician to select 5–10 voxels for every tissue class using the mouse.*

- The largest penalty is limited by clamping the distance function. A saturation $\text{dist}_{\max}$ is applied to the distance maps since distant structures should not dominate the classification distance computation.
- The derivation of the penalty from the distance values is arbitrary, e.g. the penalty may increase linearly, quadratically or logarithmically with the distance.

When the accuracy of the anatomical localization is known to be high, a quadratic distance function in conjunction with a high clamp value is applied. If the segmentation process is at an early stage, a lower clamp value and a linear increase can be chosen to reduce the effect of the anatomical localization and increase the area of uncertainty at the boundaries.

4.2.4 Dynamic Prototypes

The kNN rule is a supervised classification method, i.e. it requires training. The prototypes are example voxels of tissue classes selected by a trained technician (see Figure 4.4), used to model the probability density function of particular tissue classes. The prototypes store the spatial location of the voxel in the volume and the spectral values in each of the feature channels. The spatial location is used to update the spectral information in the anatomical localization channels, which are dynamic since they change during the iterations. The location is also directly used as a starting point for a connected component analysis (Section 4.3.3).

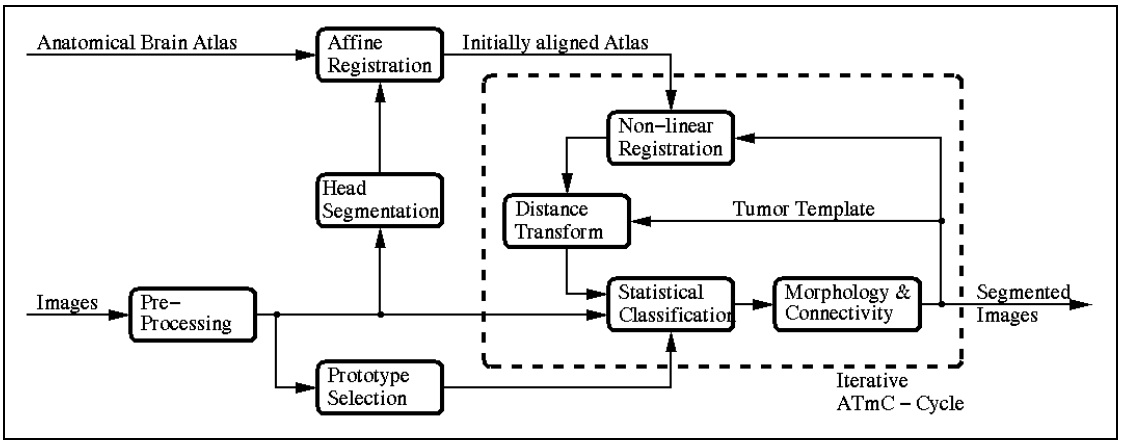

Figure 4.5: **Schematic description of the brain tumor segmentation scheme.** *The modules in the dashed box are iterated. Because the anatomical atlas does not contain tumor templates, the i-th tumor segmentation is used as a template for the (i+1)-th tumor segmentation for all* $i > 0$.

4.3 Design of ATMC for the Segmentation of Brain Tumors in MRI

The application of ATMC to a specific segmentation task requires several specifications and modifications. The goal of this section is the design of an automated method for the segmentation of MRI of the head of brain tumor patients into the tissue classes skin, brain, ventricles and tumor. In the following, the skin comprises all tissues that is not part of brain, ventricles or tumor, i.e. skin, fat, bone, bone marrow, muscle etc.

In the following, the necessary modifications and extensions of the ATMC concept for the task of tumor segmentation will be addressed qualitatively. Figure 4.5 is a schematic representation of the segmentation process, describing the modules of the system.

4.3.1 Segmentation Strategy

The segmentation strategy defines the order in which different structures are separated from each other, and follows a simple, hierarchical model of anatomy (illustrated in Figure 4.10. By proceeding hierarchically from the outside to the inside, each segmented structure refines the volume of interest for the next structure to be segmented.

The choice of strategy is motivated by several reasons:

- By defining volumes of interest, structures can be successfully classified which otherwise show spectral overlap with classes outside the volume of interest and therefore cannot be segmented (e.g. the tumor cannot be successfully segmented without a restriction to the ICC).

- The registration of atlas to patient is based on segmented images, i.e. segmented structures are registered to each other. The idea of the ATMC is that the accuracy of registration is improved by improving the accuracy of the segmentation. Because it is easy to separate the head from the background, but impossible to correctly segment the ICC without anatomical knowledge, an initial registration can only be achieved based on the heads of atlas and patient. The pre-aligned atlas then provides a template for the ICC, leading to a more accurate segmentation. This template in turn improves the registration of the ICC template, since a registration based on the head does not provide an exact registration of the ICC.

- An atlas of normal anatomy provides information about the location and shape of normal structures, but does not provide templates for pathologic structures. This means the atlas can be used only for the segmentation of normal anatomy, i.e. skin/fat/bone, brain and ventricles. Because it is "easier" to segment structures where anatomical information is available, these structures should be segmented first. Consequently, it is natural to segment pathologic tissue last.

- The registration paradigm assumes correspondence between every structure in atlas and patient. Because there is no tumor in the atlas, a correspondence is not available. This has two consequences. First, during ICC segmentation, a compound class of the normal and pathologic brain structures is formed. The atlas is registered to the brain *and* pathology. Second, for the segmentation of the tumor, only the atlas brain template is used. A tumor template is derived during the iteration of segmentation and registration.

4.3.2 Initialization

The initialization of the segmentation process involves two pre-processing steps:

1. Noise reduction of the MR data to improve the SNR (Figure 4.6)

2. Initial spatial alignment of a digital 3D anatomical atlas to the patient images with an affine transform. The alignment is established based on the atlas and patient head, which is segmented using thresholding followed by a combination of local segmentation strategies (Figure 4.7)

which will be briefly discussed in the following.

Noise Reduction

MRI data is usually noisy. When using fast, high resolution imaging sequences, tradeoffs are made regarding image contrast and signal-to-noise ratio (SNR). These properties reduce the quality of any segmentation process. Thus, noise reduction is an essential step prior to segmentation.

Linear spatial filters (e.g. low pass filtering) reduce the amplitude of noise at the cost of blurring high frequency details such as lines and edges and diffusing small

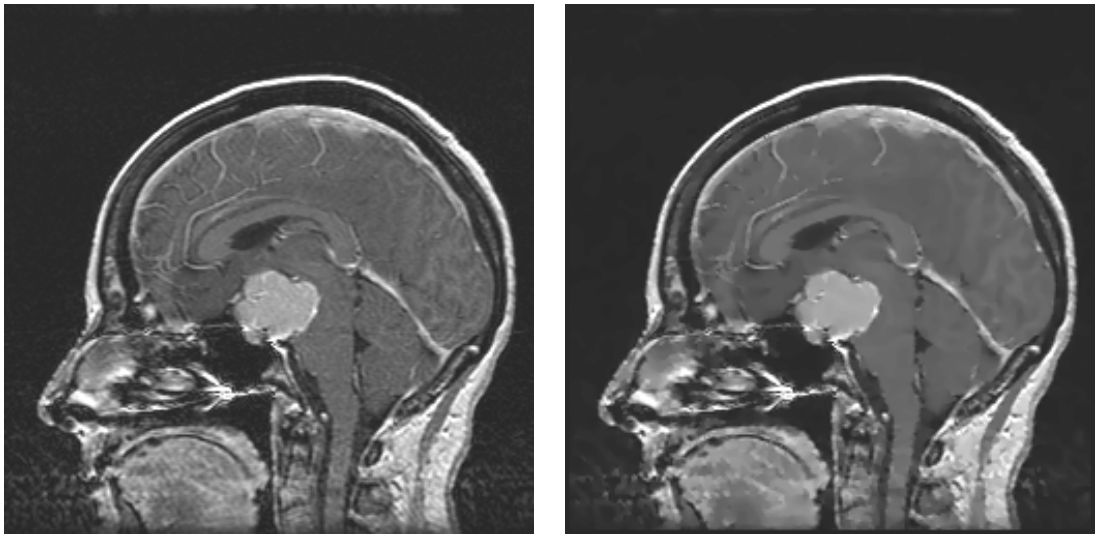

(a) Cross-section of the original 3D MRI (b) MRI after noise reduction

Figure 4.6: **Noise reduction with non-linear anisotropic diffusion filtering.** *The parameters of the filter are set to make skin, brain, ventricles and tumor more homogeneous without blurring the boundaries of these structures.*

structures. Nonlinear filtering methods (commonly median filtering) reduce these effects, but result in a loss of resolution by suppressing fine details.

The filtering technique used in this work is known as "non-linear anisotropic diffusion filtering" developed by Perona and Malik [102] and first applied to MR images by Gerig *et al.* [47]. It is capable of noise reduction whilst preserving and enhancing object boundaries and detailed structures. In principle, the filtering is modeled as an anisotropic diffusion process of heat. Assuming the image to be piecewise constant or slowly varying inside objects, the strength of smoothing (diffusion) may be locally adapted according to the image gradient, thus encouraging smoothing inside regions (low image gradient) and stopping smoothing at object boundaries (high image gradient). The diffusion process is executed iteratively by solving

$$\frac{\partial I}{\partial t} = \nabla \cdot (c(\kappa) \cdot \nabla I) \tag{4.11}$$

iteratively, where I is the image, t is time (iteration number) and $c(\kappa)$ is the spatially adaptive diffusion strength function. The parameter κ acts as a threshold for valid edges. Figure 4.6 shows an example of the improvement through this technique with $\kappa = 5.2$ and $t = 2$ (see [47], Section 3.5).

Initial Alignment of the Atlas to the Patient

The goal of the linear registration is an initial global alignment between the anatomical brain atlas and the patient. This is a necessary pre-requisite for the following

non-linear registration steps, which are restricted to the detection of local deformations. In order to align the atlas with the patient an affine transformation (9 degrees of freedom, translation, rotation, scaling) is estimated. The algorithm utilized here is described below and is based on a method described in [138].

(a) Atlas head and patient MRI cross-sections before affine registration

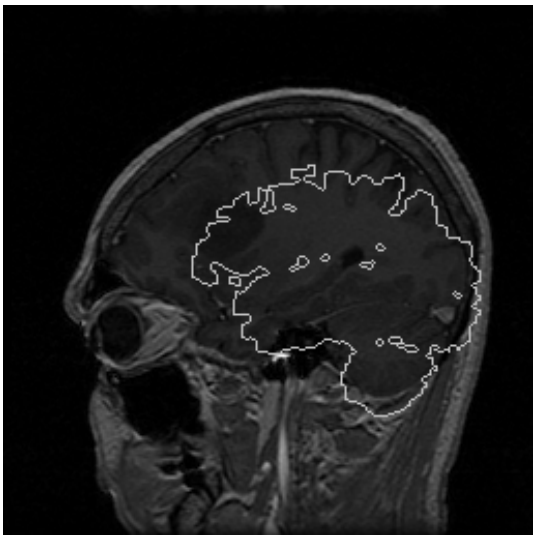

(b) Cross-section of 3D MRI and overlay of atlas brain contour before registration

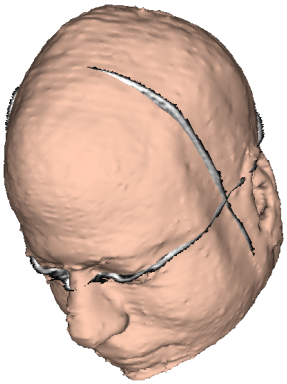

(c) Atlas head and patient MRI cross-sections after affine registration

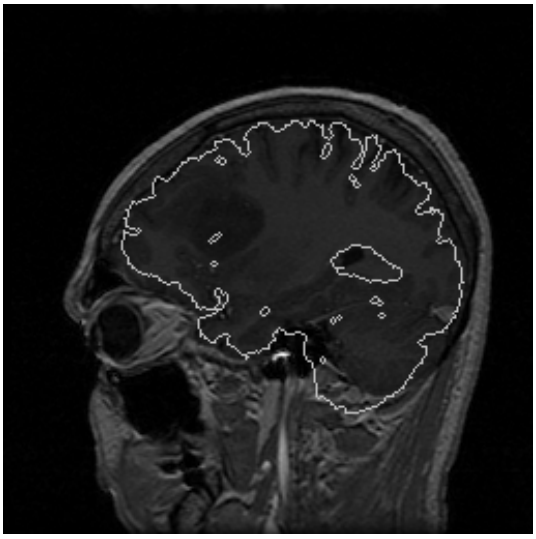

(d) Cross-section of 3D MRI and overlay of atlas brain contour after registration

Figure 4.7: **Affine initial alignment of the atlas to the patient.** *The atlas head (3D-model in (a), (c)) is aligned to a preliminary segmentation of the patient head (MRI cross-sections in (a), (c). The transform resulting from the registration of the atlas head is applied to the atlas brain (d), improving the alignment of atlas and patient brain (b).*

Given two labeled images, the fixed image $I_{\mathrm{f}}(\mathbf{x})$ and the moving image $I_{\mathrm{m}}(\mathbf{x})$ with $\mathbf{x} = [x, y, z]^T$, then the linear affine transformation

$$T: \quad I_{\mathrm{m}}(\mathbf{x}) \rightarrow I_{\mathrm{f}}(\mathbf{x}) \tag{4.12}$$

that registers image $I_{\mathrm{m}}(\mathbf{x})$ to $I_{\mathrm{f}}(\mathbf{x})$ is computed by minimizing the similarity measure

$$S = \sum_{i=1}^{N} f\left(I_{\mathrm{f}}(\mathbf{x}_i), I_{\mathrm{m}}(T^{-1}(\mathbf{x}_i)\right) \quad , \tag{4.13}$$

where N is the total number of voxels and

$$f\left(I_{\mathrm{f}}(\mathbf{x}_i), I_{\mathrm{m}}(T^{-1}(\mathbf{x}_i)\right) = \left\{ \begin{array}{ll} 0 & \text{for} \quad I_{\mathrm{f}}(\mathbf{x}) = I_{\mathrm{m}}(T^{-1}(\mathbf{x})) \\ 1 & \text{for} \quad I_{\mathrm{f}}(\mathbf{x}) \neq I_{\mathrm{m}}(T^{-1}(\mathbf{x})) \end{array} \right\} \quad . \tag{4.14}$$

For the minimization process a direct descent method based on Powell's algorithm and described in [105] is adopted. To decrease conversion time, a multiresolution pyramid is formed by subsampling by a factor of 2 in each dimension. The minimization is carried out in a coarse-to-fine manner, minimizing on each level and taking the tentative transform to the next higher resolution. Algorithm 4.1 shows the scheme of the algorithm.

from coarse to fine resolution **do**
 repeat until convergence
  compute T_{i+1}: $S_{i+1}(\mathbf{I}_f, \mathbf{I}_m) < S_i(\mathbf{I}_f, \mathbf{I}_m)$
  apply T_{i+1} to I_{m}

Algorithm 4.1: Global affine registration. *A similarity measure S_i is minimized with a direct descent method. S_i counts the number of voxels of mismatch between the segmented fixed image $\mathbf{I}_f$ and the segmented moving $\mathbf{I}_m$. The transform T_i is computed on a coarse-to-fine image resolution hierarchy.*

Initialization of the algorithm is crucial to the convergence, since Powell's method is a local optimization procedure prone to remain in a local instead of the desired global minimum. In this work, this is achieved in the following way:

- Segmentation of the head in the patient dataset using thresholding and local segmentation strategies.
- Find the initial pose according to the acquisition order of the atlas and the patient dataset. Align the top and the back of the bounding boxes of the atlas and the patient head.

4.3.3 Local Strategies for the Refinement of Segmented Structures

The global nature of statistical classification results in gross separation of tissue types based on grey value intensities. As a result, image artifacts lead to segmentation artifacts, typically small holes in the structures of interest, clusters of non-object pixels, and thin connections between different objects.

Local low level segmentation operations allow to divide an image based on structural and shape assumptions. Here, two assumptions are made. First, all voxels of an object may be joined by one path, which may be accomplished by a region growing algorithm [1]. Second, thin structures are not allowed. Objects connected by thin structures are separated through binary morphological operations to prevent the region growing algorithm from joining two different objects [112].

The remainder of this section explains in principle how these operations work and how they may be combined. For further reading refer to e.g. [1, 112].

Mathematical Morphological Operations

Structural analysis of binary images can be done efficiently with mathematical morphological operations. The two basic operations are *erosion* and *dilation*. In principle, applying a morphological operation to a binary images (foreground and background) involves the translation of a *structuring element* (kernel) to all foreground points in the input image, and examining the intersection between the translated kernel coordinates and the input image coordinates. The structuring element consists of a pattern specified as the coordinates of a number of discrete points relative to some origin.

The mathematical definition of erosion and dilation of binary images are as follows: Suppose that I is the set of euclidian coordinates corresponding to the input binary image, and that K is the set of coordinates for the structuring element. Let Kx denote the translation of K so that its origin is at x. The *erosion* of I by K is the set of all points x such that Kx is a subset of X. The *dilation* of I by K is the set of all points x such that the intersection of Kx with I is non-empty.

If the structural element is a small sphere shape, erosion "shrinks" an object and removes thin connections to other structures, while dilation "grows" back boundary pixels that have previously been eroded.

Seeded Region Growing

Region growing is a procedure that groups pixels or subregions into larger regions based on the connectivity of pixels with similar or identical properties (here, identical label values, since the region growing is executed on classified image data). In the case of seeded region growing (SRG), region growing is performed with respect to one or more *seeds* as starting points. This method is efficient and easily implemented. Algorithm 4.2 shows the scheme for SRG.

The selection of seeds is crucial to the performance of the region growing algorithm, since seed locations outside the structure of interest could lead to the segmentation of an object other than the object of interest. In the context of the

repeat until $S = \{\emptyset\}$
  take and remove leading seed s from S
  for all voxels $i \in R$ of s
   if $l(i) = l(s)$ **then**
    append v to S
    set $l(o) = l(i)$

Algorithm 4.2: Seeded region growing (SRG). *Let* $S = \{s_1, ..., s_N\}$ *the initial set of seedpoints,* $I = \{i_1, ..., i_M\}$ *the set of input image voxel locations,* $O = \{o_1, ..., o_M\}$ *the set of output image voxel locations,* $l(i_j)$ *the label value at location* i_j *and* R *the local neighborhood of* i_j.

segmentation system however, seed locations need not be selected and controlled algorithmically (as is done e.g. in [140]), but can be derived from the kNN-prototypes selected by the user.

Application of Local Refinement Methods

For each structure of interest, the following local low level operations are applied to the presegmented image:

1. *Erosion* to remove thin connections between the object of interest and other objects or clusters of voxels.

2. *Seeded region growing* to identify all voxels that belong to the structures of interest, fill small holes inside the structures and remove non-connected pixels. The tissue prototypes from the classification step (Section 4.2.4) serve as seedpoints.

3. *Dilation* to recover the boundary that was eroded in the first step

.

All procedures in the refinement step operate in 3D. This is necessary since in 2D parts of an object may appear non-connected although they are connected in 3D. For the morphological operations a spherical structuring element with a window size of $7 \times 7 \times 7$ was found to be a good choice, and the region growing algorithm uses the 18-connectivity model.

4.3.4 Segmentation of Structures present in the Atlas

For the segmentation of structures present in the atlas, three compound classes are differentiated: skin/fat/bone, brain/pathology and ventricles. The segmentation system proceeds hierarchically, each segmentation step providing a volume of interest for the next structure to segment:

1. Using the initially aligned atlas structures skin/fat/bone and brain/ventricles (ICC) (Figure 4.8(a)) as anatomical constraints, the kNN classification subdivides the patient image volume into the classes background, skin/fat/bone and ICC (consisting of brain, ventricles and pathology). The ICC is assumed to be a single, connected objects, so classification artifacts can be removed using morphological operations combined with region growing (Figure 4.8(b)).

2. To improve the alignment of the atlas, the ICC template is now re-aligned to the first patient ICC segmentation. Because the template has already been registered linearly, the remaining residual mis-alignment can be considered local, and is typically non-linear. The atlas ICC is re-aligned using the non-linear registration method described in Section 5.1.4 (Figure 4.8(c)).

3. With the re-aligned atlas template, a second kNN-classification and local segmentation step is carried out (Figure 4.8(d)). 4 iterations of registration, kNN-classification and local segmentation were found to be optimal in terms of robustness, accuracy and computation time.

4. Next, the ventricle is classified using the ICC template as anatomical constraint and local segmentation strategies are applied (Figure 4.9). No template of the atlas is used, because the registration does not produce sufficiently accurate registration results (see Section **??**). However, restriction to the ICC is sufficient.

The segmentations of the brain/pathology and the ventricles define a volume of interest for pathological tissue.

4.3.5 Segmentation of Pathology: Meningiomas and Low Grade Gliomas

Meningiomas and low grade gliomas show homogeneous tissue composition, such that they can be modeled with a single tissue class. Another important aspect is the spectral overlap of pathologic with normal tissue. The meningioma tissue class partially overlaps with parts of the skin, fat in the neck, parts of the vessels and the dura. Low grade gliomas partially overlap with the skin and parts of the outer cortex. In both cases, classification constrained with the brain template does captures the tumor, but details on the boundary or parts of the tumor can be lost due to the application of mathematical erosion and dilation (Figure 4.10(c)). To capture the whole tumor, a template is derived from the first tumor segmentation by applying a distance transform to it (Figure 4.10(e)). The second classification is constrained with the brain and the tumor template, to prevent cortex voxels from being segmented as tumor (Figure 4.10(e)), and no local segmentation strategies are applied to prevent the undesired smoothing effect.

Note that the atlas is also re-registered and the patient's skin, brain and ventricles are re-classified. Registration of the atlas to the patient brain is achieved in the following way: a) the patients tumor is relabeled with the patient's brain label, b) the ventricles are relabeled to background, c) the atlas brain is registered to the relabeled brain (which contains brain and pathology).

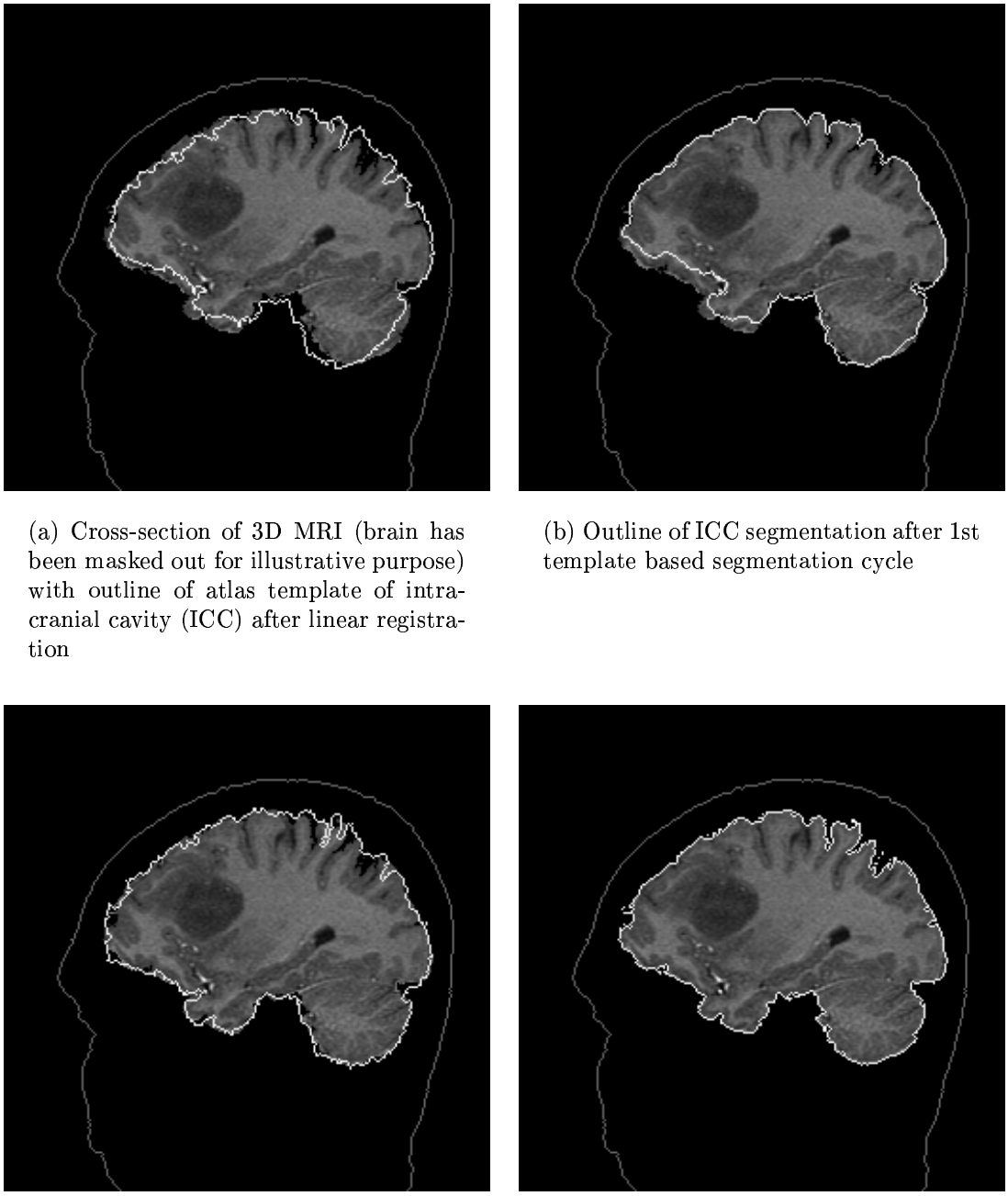

(a) Cross-section of 3D MRI (brain has been masked out for illustrative purpose) with outline of atlas template of intra-cranial cavity (ICC) after linear registration

(b) Outline of ICC segmentation after 1st template based segmentation cycle

(c) Outline of atlas ICC template after nonlinear re-registration

(d) Outline of ICC segmentaion after 2nd template based segmentation cycle

Figure 4.8: **Improvement of the intra-cranial cavity (ICC) segmentation during the classification-registration iteration.** *Linear registration of the atlas template results in a rough alignment to the patient ICC (a). Template based segmentation with the linearly aligned atlas template improves the segmentation (b). Re-registration of the atlas (c) result in improved alignment and a 2nd segmentation cycle results in an improved ICC segmentation (d).*

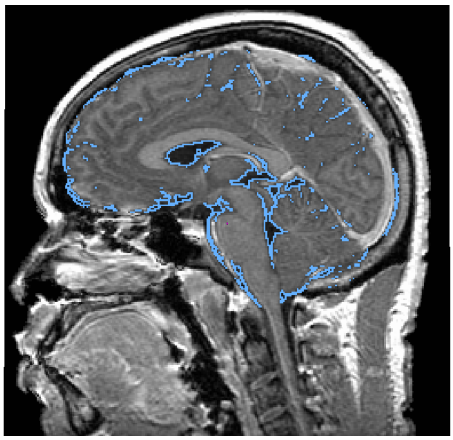

(a) Cross-section of 3D MRI and outline of ventricles after template moderated classification

(b) Cross-section of 3D MRI and outline of ventricles after artifact removal using local segmentation strategies

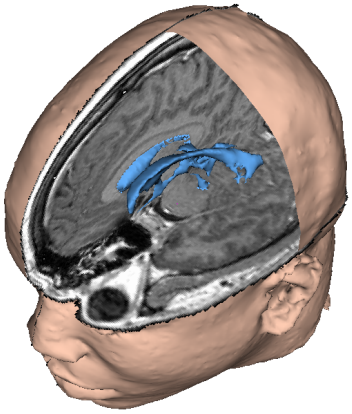

(c) 3D rendering and axial MRI cross-section of ventricles

Figure 4.9: **Improvement of the ventricle segmentation during the classification-registration iteration.** *Segmentation the ventricles (a) using template moderated classification (ICC template) results in artifacts (CSF surrounding the brain). The CSF surrounding the brain can be removed with the application of local segmentation strategies (b).*

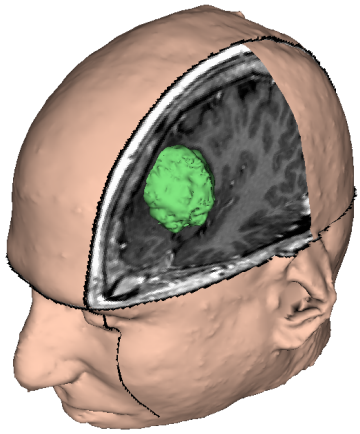

(a) MRI cross-sections and 3D model of skin and tumor

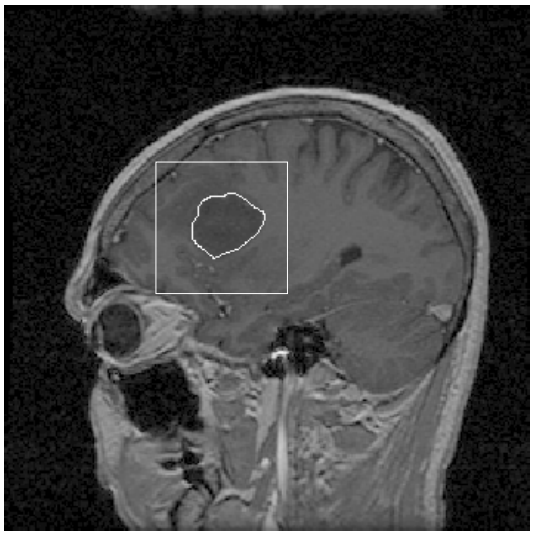

(b) MRI cross-section and manual outline of tumor

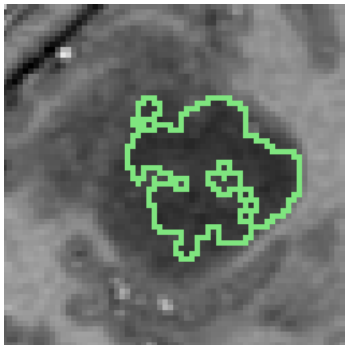

(c) Tumor after first segmentation cycle (with brain template)

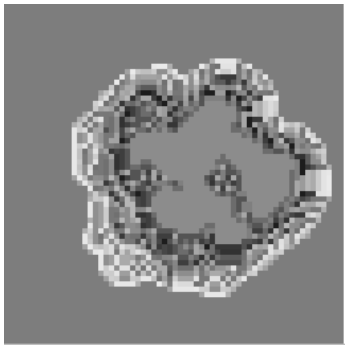

(d) Tumor template (distance map from segmentation in (c)

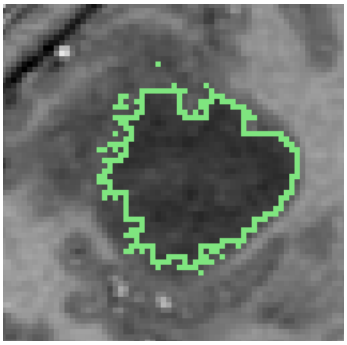

(e) Tumor after second segmentation cycle (with brain and tumor template)

Figure 4.10: **Improvement of the tumor segmentation during the classification-registration iteration.** *Classification constrained with ICC and ventricle templates results in artifacts (a). The application of local segmentation strategies (b) removes distant artifacts, but cannot capture the whole tumor. A distance transform of the preliminary tumor segmentation is used as a template for re-classification of the tumor (d).*

4.4 Illustrative Results

Table 4.1 lists the parameter settings used throughout this work. Furthermore, every iterational process requires a stop criteria. Ideally, the segmentation process converges when the aligned templates of the atlas match the classified structures in the anatomy. However, this criteria is not applicable since there are no pathologic structures in the atlas. Instead, a fixed number of iteration cycles were derived experimentally: 4 iterations for the ICC segmentation, 1 iteration for the ventricle segmentation, and 2 iterations for the tumor segmentation. The brain and the ventricle are also re-segmented during tumor segmentation.

Segmentation Module	Parameters
Anisotropic Diffusion	Iterations $i = 2$, timestep $dt = 0.2$, $\kappa = 5.2$
kNN Classification	$k = 5$, number of classes $C = 5$
Affine Registration	9 degrees of freedom, 4 resolution levels
Distance Transform	Square of euclidian distance, saturation $\text{dist}_{\max} = 100$
Non-linear Registration	3 resolution levels, min. window size $w = 9{\times}9{\times}9$
Morphology	spherical structuring element, $w = 7{\times}7{\times}7$
Region Growing	18-connectivity

Table 4.1: **Parameter settings for each module.** *The parameter settings are also used for the validation in Section 6.1.*

For the segmentation of normal structures (i.e. skin/fat/bone, brain, ventricles), the pattern used in this work is $\mathbf{v}_i = [v_i^1, ..., v_i^5]^T$, i being the index to a spatial location $\mathbf{x}_i$ according to Section 4.2.1. In order to provide a concise overview of the elements v_i^l, the image processing steps described in the previous sections are represented by Operators T_l, i.e.

$$
\begin{aligned}
v_i^1 &= T_1(I(\mathbf{x}_i)), \quad T_1: \text{ Anisotropic Diffusion Filtering} \\
v_i^2 &= T_2(A(\mathbf{x}_i)), \quad T_2: \text{ Distance transform of skin/fat/bone} \\
v_i^3 &= T_3(A(\mathbf{x}_i)), \quad T_3: \text{ Distance transform of skin/fat/bone background} \\
v_i^4 &= T_4(A(\mathbf{x}_i)), \quad T_4: \text{ Distance transform of brain} \\
v_i^5 &= T_5(A(\mathbf{x}_i)), \quad T_5: \text{ Distance transform of brain background}
\end{aligned}
$$

which are applied to the MRI $I(\mathbf{x})$ and the image of the registered anatomical atlas $A(\mathbf{x})$ respectively. While T_1 is carried out only during the preprocessing stage, the operators $T_2, ..., T_5$ are applied to the re-registered atlas in every segmentation iteration cycle. For the first tumor segmentation cycle, the patterns are also $\mathbf{v}_i = [v_i^1, ..., v_i^5]^T$. For the second tumor segmentation cycle, the patterns are $\mathbf{v}_i = [v_i^1, ..., v_i^6]^T$, where the v_i^l, $i = 1..5$ are defined as above, but with the additional element

$$
v_i^6 = T_6(I_b(\mathbf{x}_i)), \quad T_6: \text{ Distance transform of initial tumor segmentation}
$$

where I_b is the result image of the first tumor segmentation.

Segmentation Module	Processing Time [min.sec]
Anisotropic Diffusion	0.15
kNN Classification	0.52
Affine Registration + Reformatting	5.58
Euclidian Distance Transform	3.30
Elastic Registration + Warping	2.30
Morphology + Region Growing	1.36

Table 4.2: **Mean processing times for each of the segmentation modules.** *The algorithms were implemented in parallel and benchmarked in a high performance computing environment on a full 3D dataset consisting of 256×256×124 voxels. The overall mean computing time for a complete segmentation was approximately 75 minutes. Overall operator time was approximately 5–10 minutes, while overall manual segmentation time was reported to be in the range of 180 minutes.*

In Table 4.2 the processing times of each module for a volume containing 256 × 256× 124 voxels are listed.

All algorithms were multi-threaded implementations. K-NN classification (implemented based on the k-DT method [140]), distance transform, non-linear matching and local refinement operations were executed on a Sun Enterprise Server (ES) 6000 (20 233 Mhz UltraSPARC-II CPUs and 5 GB of RAM). Execution of the affine registration was carried out on a compute cluster consisting of two Sun Enterprise Server 5000 (ES 5000, 8 167 Mhz UltraSPARC-I CPUs and 2 GB of RAM) and an ES 6000. The three machines were interconnected via a hybrid network: The main network was Fast Ethernet. The two ES 5000s were also connected via a private SCI network. The ES 6000 was also connected to the 5000s via a 1Gbps Ethernet.

The overall computation time amounted to approximately 75 minutes on the HPC cluster described above. The overall operator time was approximately 5–10 minutes for the selection of prototypes for each of the relevant tissue classes. Overall manual segmentation time has been reported to be in the range of 180 minutes [98]. Thus, the automated method achieves a reduction of the operator time for a segmentation of around 95%.

Figure 4.11 and Figure 4.12 show the segmentation of a meningioma and a low grade glioma with the kNN-rule alone and the ATMC-method. Complete segmentation of the structures is possible with the developed segmentation method, while the kNN-method results in several misclassifications, and the registered atlas cannot identify pathology at all. A quantitative validation study is presented in Chapter 6.

4.5 Conclusion

The spectral and anatomical properties of some of the most common brain tumors, i.e. meningiomas and low grade gliomas were analyzed. A new method for the segmentation of meningiomas and low grade gliomas was developed. The method, based on a combination of statistical classification, anatomical knowledge derived

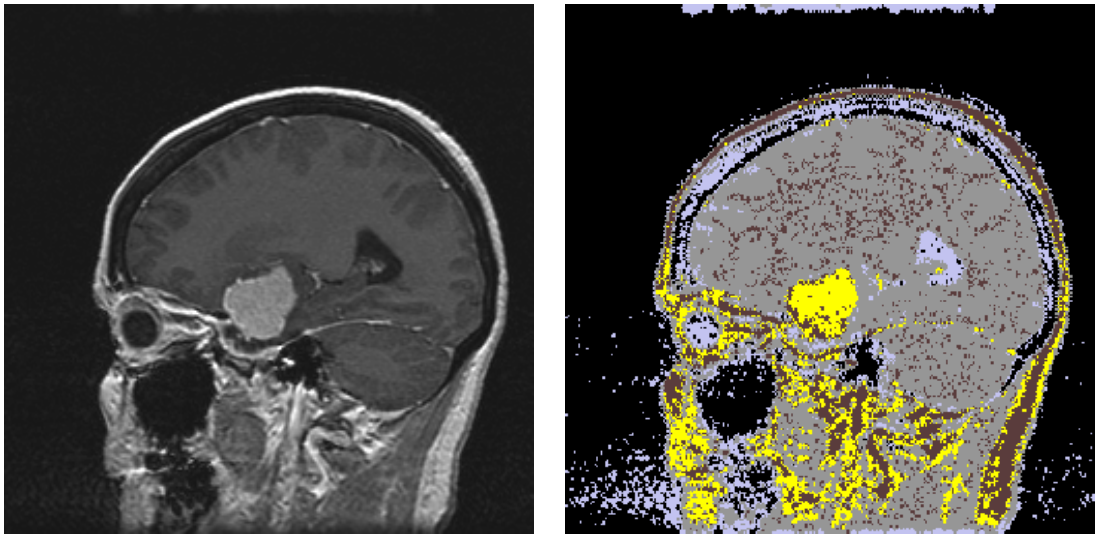

(a) Cross-section of 3D MRI with a Meningioma

(b) Result of kNN-rule classification

(c) Result of ATMC segmentation

Figure 4.11: **Example for kNN and ATMC segmentation of a meningioma.** *The ATMC correctly segments each of the structures, while kNN alone suffers from signal intensity distribution overlap.*

from the registration of a digital atlas, and structural segmentation techniques, is capable of resolving the ambiguities caused by overlapping tissue class distributions, and enables to segment pathology not represented by the anatomical brain atlas.

The iteration of a) statistical classification and b) registration of an anatomical brain atlas allows for the automated segmentation of the skin surface, the brain, the ventricles and the brain tumor.

The application and validation results of the new segmentation method are pre-

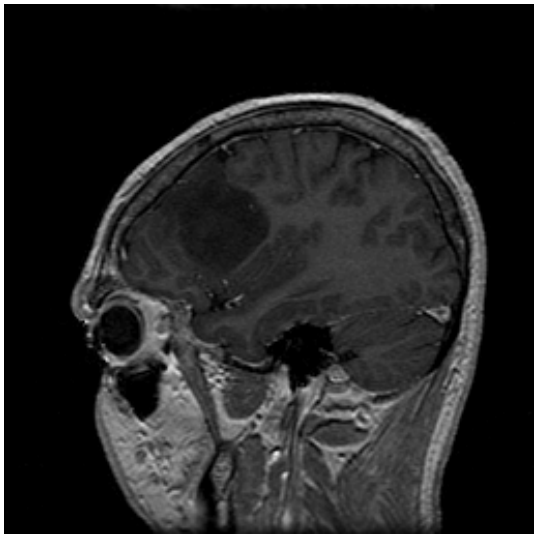

(a) Cross-section of 3D MRI with a low grade glioma

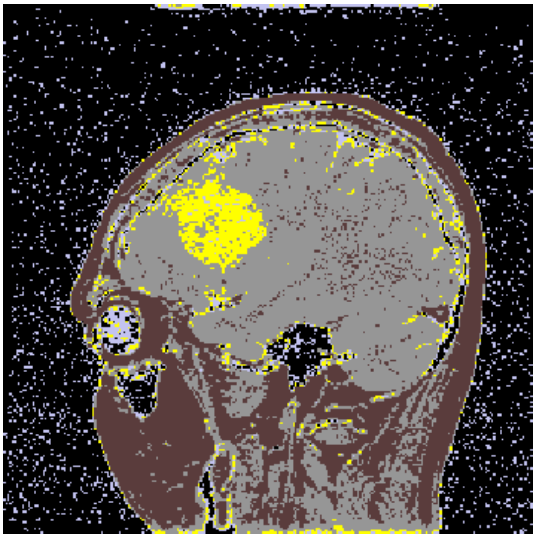

(b) Result of kNN-rule classification

(c) Result of ATMC segmentation

Figure 4.12: **Example for kNN and ATMC segmentation of a low grade glioma.** *The ATMC correctly segments each of the structures, while kNN alone suffers from signal intensity distribution overlap.*

sented in Chapter 6.

Chapter 5

Non-linear Registration of Medical Images for ATMC

The adaptive template moderated segmentation (ATMC) approach developed in the preceding chapter makes use of an optical flow method to align a digital atlas to individual patient datasets. In this chapter, the performance of several optical flow methods for the purpose of aligning segmented images is compared and the adaptive template approach is found to be the most efficient. However, this method leads to mis-registrations, if several objects that move or deform independently need to be aligned, and if the underlying data has not been segmented correctly. The analysis of an adaptive regularization approach suggested for this situation leads to the development of a new, computationally efficient method for the alignment of multiple objects in images with segmentation errors.

In Section 5.1 the mathematical model of two optical flow approaches, i.e. a regularization method and an adaptive template matching method, are briefly reviewed.

In Section **??**, a 2D adaptive regularization approach that models discontinuities resulting from the movement of independent objects is extended to 3D. A representation for discontinuities in 3D is derived, and a multigrid method is designed for the numerical solution of the resulting partial differental equations (PDEs).

The analysis and comparison of adaptive regularization and adaptive template matching in Section **??** shows i) significant computational disadvantages of the adaptive regularization method, ii) the limitations of both methods regarding the registration of multiple templates, and iii) the limitations of both methods regarding the registration of images with segmentation errors.

This analysis leads to the formulation of a probabilistic, multi-channel adaptive template matching method in Section **??**, which performs well in the presence of multiple objects and achieves better results with segmented data, while maintaining the computational advantages of template matching.

5.1 Optical Flow

5.1.1 Optical Flow for 3D Medical Image Registration

Optical flow has traditionally been used to determine the movement (translation) of objects in images of a scene over time. In medical image registration, however, the goal is to align two images (and the objects represented by them), i.e. to deform a template image I_1 to optimally fit a target image I_2. In the optical flow paradigm, the template image can be interpreted as the second instance of a scene represented in the target image, and the optical flow represents the shape differences between two objects. The optical flow field is usually represented by a vector field $\mathbf{u}(\mathbf{x}) = [u(\mathbf{x}), v(\mathbf{x}), w(\mathbf{x})]^T$ that stores a translation for every location $\mathbf{x} = [x, y, z]^T$ in I_1. To construct the deformed template image $I_1' \leftarrow I_1$, $\mathbf{u}$ is used to translate the value at each location in I_1 according to $I_1'(\mathbf{x}) = I_1(\mathbf{x}') = I_1(\mathbf{x} - \mathbf{u}(\mathbf{x}))$. Since $\mathbf{x}'$ in general will not be a point on the regular grid, $I_1'(\mathbf{x})$ is assigned the value $I_1(\mathbf{x}'')$, $\mathbf{x}''$ being the closest point to $\mathbf{x}'$ (nearest neighbor interpolation).

In medical image registration, differences between anatomical objects are often large [129]. To estimate large motion, or rather deformations, it is common to use a coarse-to-fine approach [4]. A resolution pyramid of both images is formed by subsampling. On every resolution level starting at the coarsest resolution, the optical flow is determined and interpolated to the next finer grid, where the deformed template image is constructed. The match is repeated on the next finer grid, until the finest resolution is reached. This coarse-to-fine strategy is adopted throughout the work presented in this chapter.

5.1.2 Estimation of Optical Flow

Region-based matching defines the relative displacement $\mathbf{u}(\mathbf{x}) = [u(\mathbf{x}), v(\mathbf{x}), w(\mathbf{x})]^T$, $\mathbf{x} = [x, y, z]^T$ between image regions $W(\mathbf{x})$ of a target image $I_2(\mathbf{x})$ and a template image $I_1(\mathbf{x})$ [7]. The best match can be found by minimizing a similarity measure $\mathbf{S}(\mathbf{u}(\mathbf{x}))$ (e.g. the sum-of-squared differences, SSD) that describes the image intensity difference between I_1 and I_2 depending on their relative displacement $\mathbf{u}(\mathbf{x})$:

$$\mathbf{S}(\mathbf{u}(\mathbf{x})) = \int_{I_2} W(\mathbf{x}) \big(I_2(\mathbf{x}) - I_1(\mathbf{x} - \mathbf{u}(\mathbf{x}))\big)^2 \, d\mathbf{x} \quad . \tag{5.1}$$

W controls the size of the image patches that are compared. Thus, deformations are assumed to be constant in this region and only estimated locally, such that S is effectively a function of $\mathbf{x}$. If the similarity between $I_1(\mathbf{x})$ and $I_2(\mathbf{x})$ increases, then $\mathbf{S}(\mathbf{u}(\mathbf{x}))$ decreases. To solve Equation (5.1), I_1 is approximated with a first order Taylor expansion

$$I_1(\mathbf{x} - \mathbf{u}(\mathbf{x})) = I_1(\mathbf{x}) - \mathbf{u}(\mathbf{x}) \nabla I_1(\mathbf{x}) \quad , \tag{5.2}$$

assuming small $\mathbf{u}$, and the substitution of Equation (5.2) into Equation (5.1) leads to

$$\begin{aligned}\mathbf{S}(\mathbf{u}) &= \int_{I_2} W(I_2 - I_1 + \mathbf{u}\nabla I_1)^2 \, d\mathbf{x} \\ &= \int_{I_2} W\left[(I_2 - I_1)^2 + 2(I_2 - I_1)\mathbf{u}\nabla I_1 + (\mathbf{u}\nabla I_1)^2\right] d\mathbf{x} \quad . \end{aligned} \tag{5.3}$$

For clarity, the dependence on $\mathbf{x}$ has been omitted. The derivative of $\mathbf{S}(\mathbf{u})$ with respect to $\mathbf{u}$ leads to

$$\begin{aligned}\frac{\partial \mathbf{S}}{\partial \mathbf{u}} &= \int_{I_2} W \frac{\partial}{\partial \mathbf{u}} \left((I_2 - I_1)^2 + 2(I_2 - I_1)\mathbf{u}\nabla I_1 + (\mathbf{u}\nabla I_1)^2 \right) d\mathbf{x} \\ &= 2\int_{I_2} W \nabla I_1 (I_2 - I_1)\, d\mathbf{x} + 2\mathbf{u}\int_{I_2} W \nabla I_1 \nabla I_1^T \, d\mathbf{x} \quad . \end{aligned} \tag{5.4}$$

With the definition of the abbreviations

$$\mathbf{Q} = \int_{I_2} W \nabla I_1 \nabla I_1^T d\mathbf{x}\,, \qquad \mathbf{f} = \int_{I_2} W \nabla I_1 (I_2 - I_1) d\mathbf{x} \quad , \tag{5.5}$$

Equation (5.4) becomes

$$\frac{\partial \mathbf{S}}{\partial \mathbf{u}} = 2(\mathbf{Q}\mathbf{u} + \mathbf{f}) \quad , \tag{5.6}$$

and the optical flow estimator becomes

$$\mathbf{Q}\mathbf{u} = -\mathbf{f} \quad . \tag{5.7}$$

5.1.3 Regularization

Optical flow can only be estimated in *structured* regions of the images, i.e. regions with a gradient ∇I different from 0 (this is also known as the aperture problem in optical flow). When $\nabla I = \mathbf{0}$, $\mathbf{Q}$ in Equation (5.5) is not invertible and Equation (5.7) has no solution. Thus, the determination of the full vector field is an under-constrained problem.

This situation can be resolved by constraining Equation (5.7). The constraints express prior knowledge about the behaviour of the deformation field. In the literature, a simplified model of the elastic medium has been widely used [15]. Image I_1 can be though of as being pinned to an elastic medium and locally deformed until an optimal fit with the image I_2, which is in a fixed frame, is achieved. By adding an *elasticity* or *smoothness* functional

$$\begin{aligned}\mathbf{E}(\mathbf{u}) &= \lambda \nabla u (\nabla u)^T \\ &= \lambda \left(u_x^2 + u_y^2 + u_z^2 + v_x^2 + v_y^2 + v_z^2 + w_x^2 + w_y^2 + w_z^2 \right) \quad , \end{aligned} \tag{5.8}$$

the energy potential now becomes the sum of $\mathbf{S}(\mathbf{u}) + \mathbf{E}(\mathbf{u})$. The *similarity* measure $\mathbf{S}(\mathbf{u})$ describes the goodness of fit between the two images, and the elasticity functional $\mathbf{E}(\mathbf{u})$ interpolates the deformation estimated in regions of high structure into regions of no or little structure. This approach is also known as *regularization* [128].

The Euler-Lagrange formalism (e.g. [16]) can be used for the minimization of functionals of the type

$$F(y(x)) = \int (f(x,\, y(x),\, y_x(x))\; dx \tag{5.9}$$

by solving the partial differential equation (PDE)

$$F_y - \frac{d}{dx} F_{y_x} = 0 \quad . \tag{5.10}$$

Then, the minimization of $\mathbf{S}(\mathbf{u}) + \mathbf{E}(\mathbf{u})$ is equivalent to solving the system of partial differential equations

$$\begin{aligned}
\frac{\partial \mathbf{S}}{\partial u} - \frac{\partial}{\partial x}\frac{\partial \mathbf{E}}{\partial u_x} - \frac{\partial}{\partial y}\frac{\partial \mathbf{E}}{\partial u_y} - \frac{\partial}{\partial z}\frac{\partial \mathbf{E}}{\partial u_z} &= \mathbf{0} \\
\frac{\partial \mathbf{S}}{\partial v} - \frac{\partial}{\partial x}\frac{\partial \mathbf{E}}{\partial v_x} - \frac{\partial}{\partial y}\frac{\partial \mathbf{E}}{\partial v_y} - \frac{\partial}{\partial z}\frac{\partial \mathbf{E}}{\partial v_z} &= \mathbf{0} \\
\frac{\partial \mathbf{S}}{\partial w} - \frac{\partial}{\partial x}\frac{\partial \mathbf{E}}{\partial w_x} - \frac{\partial}{\partial y}\frac{\partial \mathbf{E}}{\partial w_y} - \frac{\partial}{\partial z}\frac{\partial \mathbf{E}}{\partial w_z} &= \mathbf{0} \quad .
\end{aligned} \tag{5.11}$$

Using Equation (5.8) leads to

$$\begin{aligned}
-\frac{\partial}{\partial x}\frac{\partial \mathbf{E}}{\partial u_x} - \frac{\partial}{\partial y}\frac{\partial \mathbf{E}}{\partial u_y} - \frac{\partial}{\partial z}\frac{\partial \mathbf{E}}{\partial u_z} &= -\lambda \left(\frac{\partial}{\partial x} 2u_x + \frac{\partial}{\partial y} 2u_y + \frac{\partial}{\partial z} 2u_z \right) \\
&= -2\lambda \left(u_{xx} + u_{yy} + u_{zz} \right) \\
&= -2\lambda \Delta u \quad ,
\end{aligned} \tag{5.12}$$

and substitution of equations (5.6) and (5.12) into Equation (5.11) leads to

$$\mathbf{Q}\mathbf{u} - \lambda \Delta \mathbf{u} = -\mathbf{f} \quad . \tag{5.13}$$

The parameter λ controls the influence of the smoothness constraint on the solution for a flow field $\mathbf{u}$.

5.1.4 Adaptive Template Matching

Regularization of the optical flow estimation transports or interpolates the deformation vectors estimated in structured regions to regions where there is insufficient structure [32]. However, numerical solution of this method is computationally intensive (see Section **??**). A significant simplification of the numerical problem can be achieved by estimating the deformation field for each voxel locally and independently from other locations in the image, leading to a set of linear equations that can be solved directly [143]. The algorithm is briefly outlined:

Consider Equation (5.7) for a fixed value $\mathbf{x}$

$$Q\mathbf{u} = -f \quad , \tag{5.14}$$

where $\mathbf{u} = \mathbf{u}(\mathbf{x})$, $Q = Q(\mathbf{x})$ and $f = f(\mathbf{x})$ (see Equation (5.5) in Section 5.1). Recall that with this approach $\mathbf{u}$ is modeled to be constant in the region of W, i.e. the width of W (which is fixed for the whole volume) determines how fast $\mathbf{u}$ can vary. This means, if $\mathbf{u}$ needs to vary rapidly, a small window is required. However, if this image patch does not provide sufficient structure (i.e. $\nabla I_1 \approx 0$), a larger window size becomes necessary. The solution to this problem proposed by Dengler [32, 143] is the use of a spatially adaptive window function W

$$W = W(\mathbf{x}) = \sum_{i=1}^{i_{\max}} w_i W_i \tag{5.15}$$

that takes into account several window functions W_i of size s_i,

$$s_{i+1} = 2s_i,\ s_{\max} < \min_{x,y,z}(\text{axis length}) \tag{5.16}$$

and weighs the contribution of each of the windows with

$$w_i = \frac{1}{\sum_i \det(Q_i)} \det(Q_i) \quad , \tag{5.17}$$

where Q_i corresponds to the matrices calculated at different window sizes s_i. The weights can be seen as a measure of "topological uniqueness" or "structural information" contained in the image patch. Qualitatively, the weight tends to be large when the image patch contains large gradients in a variety of directions. If the structure of a small image patch is sufficient, $\mathbf{u}$ can be estimated, otherwise larger image patches dominate the estimation. With equations (5.15, 5.17), Equation (5.14) for arbitrary $\mathbf{x}$ becomes

$$\left(\sum_{i=1}^{i_{\max}} w_i(\mathbf{x}) Q_i(\mathbf{x})\right) \mathbf{u}(\mathbf{x}) = -\left(\sum_{i=1}^{i_{\max}} w_i(\mathbf{x}) f_i(\mathbf{x})\right) \quad , \tag{5.18}$$

which can be efficiently solved according to Cramers rule [16]. If a solution is not possible, i.e. $\det Q_i(\mathbf{x}) = 0,\ \forall i,\ \mathbf{u}(\mathbf{x})$ is set to zero.

Template matching results in a smooth deformation field, although no explicit smoothing of the deformation vectors takes place. This is due to the approximations made to achieve a rapidly solvable system of equations. Qualitatively, for every voxel, the deformation is estimated by integrating image information over several window patches. To do so, the deformation is assumed to be constant in these regions. Since neighboring voxels have similar neighborhoods, the similarity measure (integrated in the window patches) at neighboring voxels is also similar, resulting in a slowly varying or smooth deformation field.

Chapter 6

Applications

In this chapter, the algorithms developed in this thesis are applied to different problems in the domain of medical image analysis, more specifically a) the segmentation of brain tumors, b) the registration of a digital atlas to individual MR datasets, and c) the segmentation of anatomical structures in brain tumor patients which so far cannot be imaged in a clinical environment. Strategies for the validation of medical image processing methods are developed to characterize the performance of the new methods, including quantitative measures and experiments based on synthetic and clinical MRI data.

6.1 Segmentation of Brain Tumors in MRI: Meningiomas and Low Grade Gliomas

The question of how valid image segmentations are is difficult to answer, since there is no ground truth or a "gold standard" to compare with. Realistic simulation of MRI data that covers all aspects of clinical data is not yet possible [25], and dissection of actual tissue does not preserve shape nor location of structures of interest.

However, a goal of automated segmentation is to replace manual outlining without a measurable effect on the results. Therefore, a validation study was designed to determine how closely trained experts agree within a single method (automated and manual) and how closely the two methods are in segmenting the structures of interest. The consistent estimation of the structures of interest achieved with the automated and the manual method legitimates the use of the automated technique.

Brain Tumor Patients 20 patients with brain tumors of different size, shape and location were selected for this study. The pathological diagnoses included 6 meningiomas (cases No. 1–3, 11, 12, 16), and 14 low grade gliomas (cases No. 4–10, 13–15, 17-20). These two types were selected because they are relatively homogeneous and have well defined imaging characteristics. In this study, 6 out of 6 meningiomas enhanced well, and 14 out of 14 low grade gliomas were non-enhancing. Cases No. 1–10 formed the development database used for the design and validation of the automated segmentation method. The cases were extracted from a neurosurgical image database of app. 100 brain tumor patients that had been post-processed for

image-guided neurosurgery by using a combination of semiautomated techniques and manual outlining of the skin-surface, brain, ventricles, vessels and tumor. The development database provided a representative selection of meningioma and low grade glioma cases as a basis for the development of the automated segmentation tool. To ensure that the method produced correct results when applied to cases other than those of the development database, additional validation was carried out on the datasets of 10 patients that had been selected from the neurosurgery database after completion of the algorithm development.

Definition of Ground Truth The definition of a segmentation gold standard is based upon the opinion of medical experts, manifested in manual segmentations using interactive computer segmentation tools.

Manual segmentation is subject to interobserver variability and human error. To minimize the influence of these factors whilst maintaining the means of measuring the segmentation accuracy and reproducibility of the individual raters, the standard was defined based on the segmentations of 4 independent human observers.

A single 2D slice was randomly selected from the subset of MRI that showed the tumor. On this slice, the brain and the tumor was then manually outlined by 4 human observers independently. The standard segmentation for each structure and each patient dataset was defined as the area of those voxels where at least 3 out of 4 raters agreed upon the identification. All other voxels were labeled as background.

Manual segmentation of the brain and the brain tumor For manual segmentation of the brain and the tumor an interactive segmentation tool was used (MRX, GE Medical Systems, Schenectady, NY). The structures were outlined slice-by-slice by pointing and clicking with a mouse. The program connects consecutive points with lines. An anatomical object is defined by a closed contour, and the program labels every voxel of the enclosed volume.

6.1.1 Accuracy Analysis

Aim: To assess and compare the accuracy of the automated and the manual segmentation method.

Method: The automated segmentation tool was trained once on a single 2D MRI containing all tissue types of interest and executed on the full 3D dataset. This resulted in a segmentation of the entire dataset. For each dataset, the structures skin, brain, ventricles and tumor were segmented using the parameter settings described in Section 4.4.

The analysis was carried out on the basis of volume of overlap comparison in the 2D slice selected. Accuracy was defined as the overall number of correctly segmented voxels with respect to the standard segmentation

$$A = \frac{V_{TP} + V_{TN}}{V_T} \% \tag{6.1}$$

relative to the total number of voxels $V_S = 256 \times 256$ of the 2D MRI. V_{TP} (true positive volume or *sensitivity*) denotes the number of voxels correctly segmented as the structure of interest and V_{TN} (true negative volume *specificity*) denotes the number of voxels correctly segmented as background.

Results Examples of the manual and the automated segmentation of a meningioma and a low grade glioma (Figures 6.1 and 6.2) indicate the similarity between the results with the two methods.

The segmentation accuracy with the automated method was high and within the range of the accuracy of the manual method. The overall mean accuracy for the tumor segmentation was $99.68 \pm 0.29\%$ (mean $\pm$ standard deviation) with the automated and $99.68 \pm 0.44\%$ with the manual method (Figure 6.4), while the mean accuracy for the brain segmentation was $98.40 \pm 0.57\%$ and $98.81 \pm 0.88\%$ respectively (Figure 6.3).

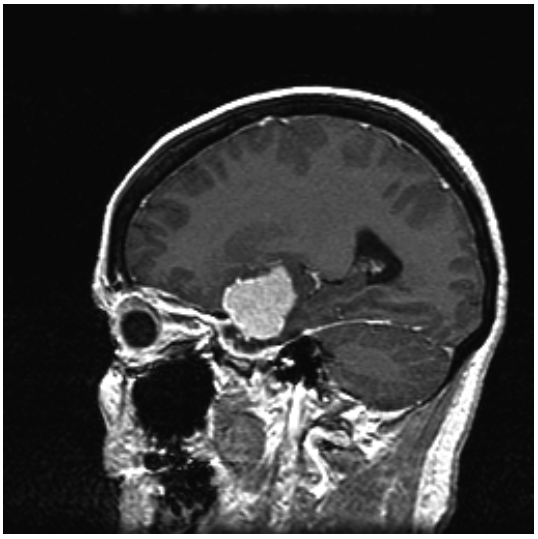

(a) Cross-section of MRI showing a Meningioma

(b) Manual Segmentation

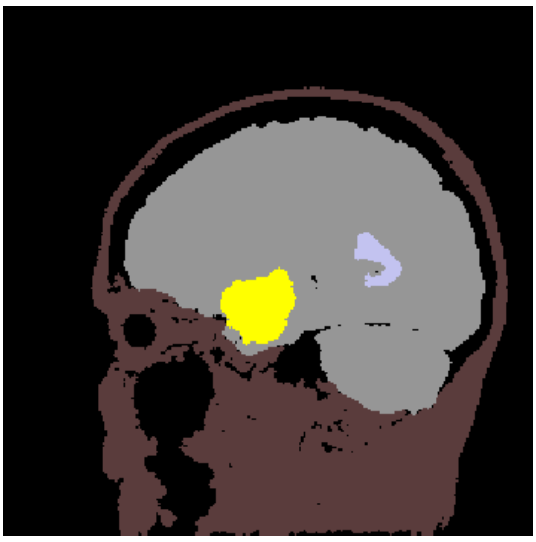

(c) Automated Segmentation

Figure 6.1: **Example of manual and automated segmentations.** *Manual and automated segmentation are consistent. It is a matter of definition that the automated skin segmentation (no cerebro-spinal fluid and air) is not equivalent to the manual skin segmentation (every voxel of the head that is not brain, ventricle or tumor).*

(a) Cross-section of MRI showing a Low Grade Glioma

(b) Manual Segmentation

(c) Automated Segmentation

Figure 6.2: **Example of manual and automated segmentations.** *Manual and automated segmentation are consistent. It is a matter of definition that the automated skin segmentation (no cerebro-spinal fluid and air) is not equivalent to the manual skin segmentation (every voxel of the head that is not brain, ventricle or tumor).*

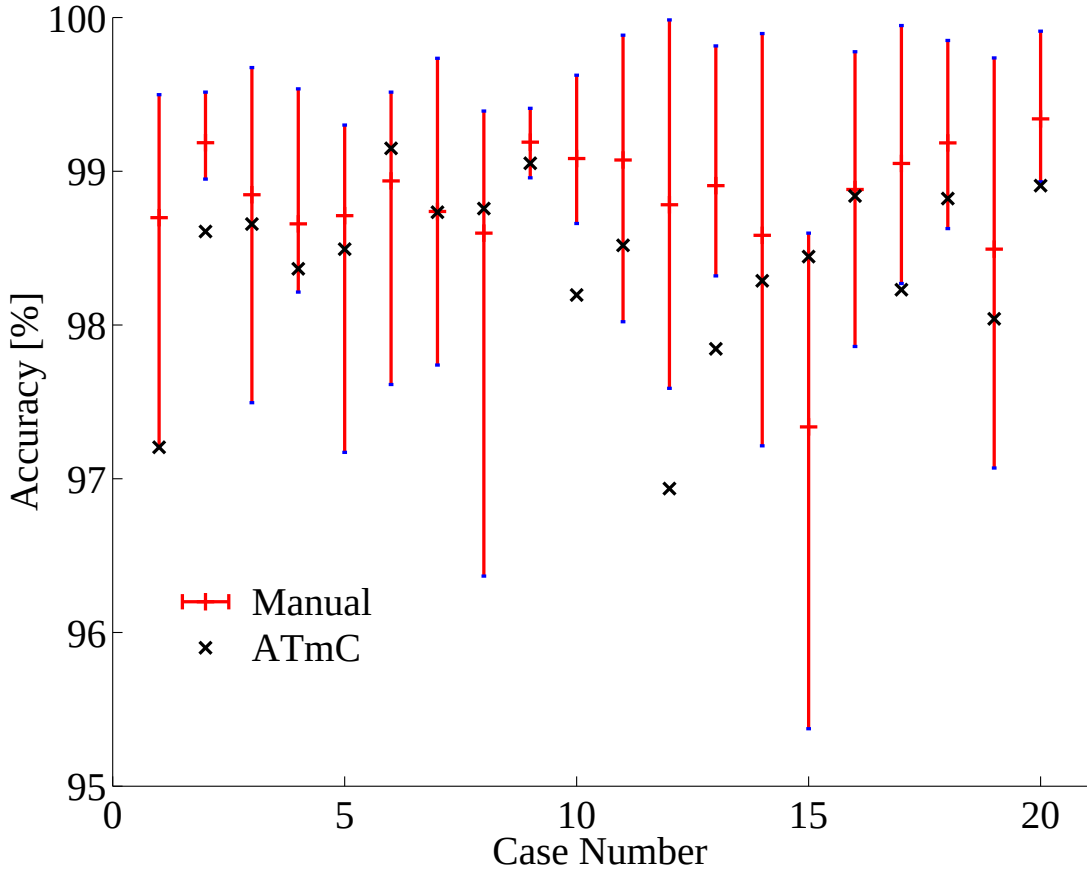

Figure 6.3: **Brain segmentation accuracy of the manual (mean, minimum and maximum) and the automated method for each of the 20 brain tumor cases.** *Meningiomas: 1–3, 11, 12, 16; low grade gliomas: 4–10, 13–15, 17–20. The bars represent the minimum, maximum and mean accuracy achieved by the four manual segmentations. The automated method is within or close to the range of the manual method.*

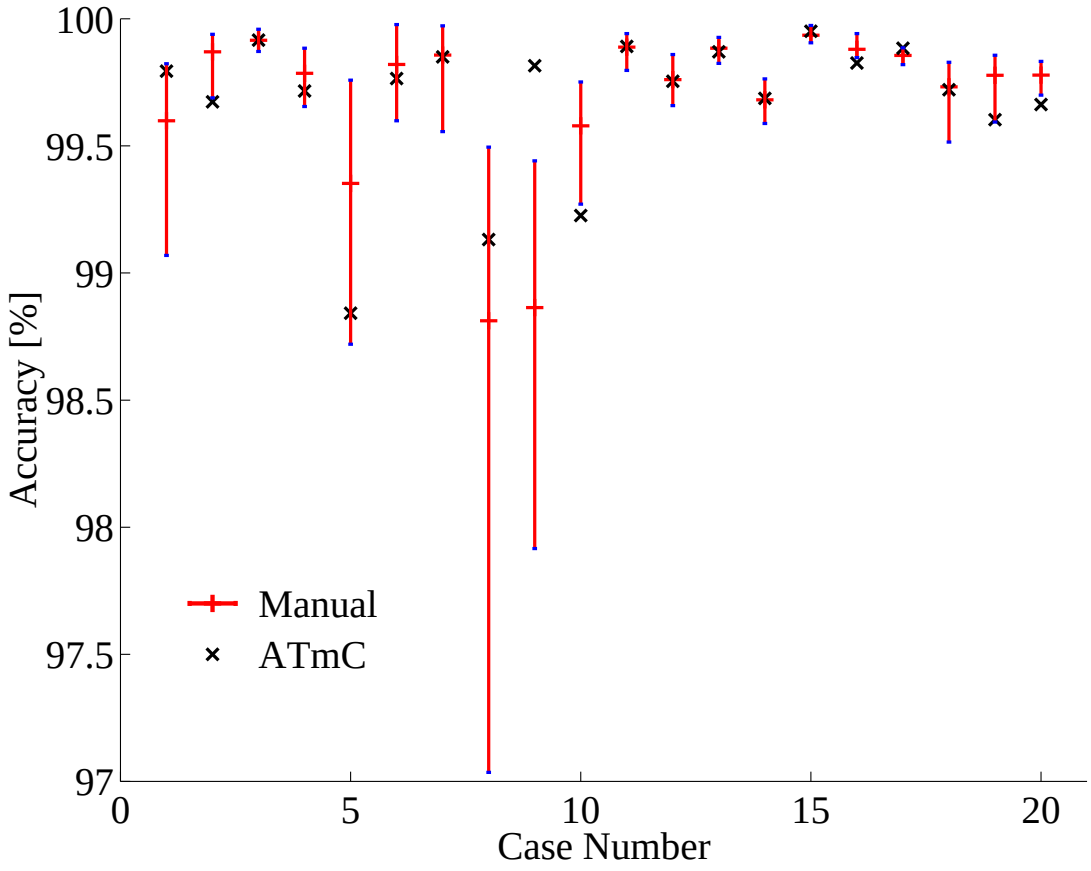

Figure 6.4: **Tumor segmentation accuracy of the manual (mean, minimum and maximum) and the automated method for each of the 20 brain tumor cases.** *Meningiomas: 1–3, 11, 12, 16; low grade gliomas: 4–10, 13–15, 17–20. The bars represent the minimum, maximum and mean accuracy achieved by the four manual segmentations. The automated method is within or close to the range of the manual method.*

Discussion The segmentation accuracy with the automated method was high, and within or close (maximum difference 0.6 %) to the range of the minimum and maximum of the accuracy with the manual method. The errors of the automated brain segmentation are in part due to the over- and under-segmentation in the area of the tentorium cerebelli and the area of the lateral sulcus with abundant vessels. The algorithm tends to oversegment these areas, if voxels e.g. of the neck close to the cerebellum are misclassified as brain and the template intra-cranial cavity (ICC) derived from the atlas is misregistered.

The size of the structure affects the segmentation accuracy. Since the comparison is based on counting the number of voxels agreed on (fore- and background), large objects tend to have a lower accuracy since there are more surface voxels to misclassify.

6.1.2 Reproducibility Analysis

Aim: To assess and compare the reproducibility of the automated and the manual segmentation method.

Method: To assess the *interrater variability error* of the automated method, training and execution of the algorithm was carried out as describe above by 4 independent operators. The variability error of the manual segmentation was measured based on the 4 manual segmentations executed for the derivation of the gold standard.

The analysis was carried out on the basis of volume of overlap comparison in the 2D slice selected. For the measurement of the *intraobserver variability error*, a fifth medical expert manually segmented each selected 2D slice 4 times over a period of one week, and training of the automated method was carried out 4 times over a period of one week.

The inter- and intrarater variability error was defined as the coefficient of variation

$$\mathrm{CV} = 100 * \frac{\mathrm{SD}[\mathrm{V_T}]}{\mathrm{M}[\mathrm{V_T}]} \,\% \tag{6.2}$$

where V_T is the total number of voxels of the segmented structure and SD and M are the mean and the standard deviation.

Results: Intraobserver variability of the automated and manual method were both low. For brain and tumor segmentation, the intraobserver variability with the automated method was 0.10–3.57% and 0.14–4.70%, while the manual method achieved CVs of 0.24–4.11% and 0.80–3.28% (Table 6.3, 6.4).

Interobserver variability was lower with the automated than with the manual method. The interobserver variability with the automated method was 0.33–4.72% and 0.99–6.11% for brain and tumor segmentation, while the manual method achieved CVs of 2.62–10.51% and 3.58–14.42% (Table 6.1, 6.2).

Table 6.1: **Interobserver variability of the brain volume segmented with the manual and the automated method.** *Listed are the mean (M) and the standard deviation (SD) of the coefficient of variation (CV) over all 13 cases. Interobserver variability is significantly reduced with the automated method.*

Tumor Histology	CV Manual		CV Automated	
	M [%]	SD	M [%]	SD
Meningioma	3.92	0.52	1.84	0.65
Low Grade Glioma	6.18	3.24	2.71	1.68

Table 6.2: **Interobserver variability of the tumor volume segmented with the manual and the automated method.** *Interobserver variability is significantly reduced with the automated method.*

Tumor Histology	CV Manual		CV Automated	
	M [%]	SD	M [%]	SD
Meningioma	5.13	0.46	2.66	0.38
Low Grade Glioma	8.05	3.79	2.97	1.58

Table 6.3: **Intraobserver variability of the brain volume segmented with the manual and the automated method.** *Intraobserver variability is consistent with both methods.*

Tumor Histology	CV Manual		CV Automated	
	M [%]	SD	M [%]	SD
Meningioma	0.42	0.03	0.36	0.45
Low Grade Glioma	1.79	1.53	1.44	1.33

Table 6.4: **Intraobserver variability of the tumor volume segmented with the manual and the automated method.** *Intraobserver variability is consistent with both methods.*

Tumor Histology	CV Manual		CV Automated	
	M [%]	SD	M [%]	SD
Meningioma	1.58	0.98	0.66	0.72
Low Grade Glioma	2.08	0.78	2.06	1.73

Discussion: The reproducibility of the segmentations for brain and tumor was high. Nevertheless, the inter- and intraobserver reproducibility of both methods are higher for the brain than for the tumor. This again may be explained with the size of the object and the nature of the segmentation error. Since the surface-to-volume-ratio is smaller for the brain than for the tumor, the disagreement on the brain surface with respect to the overall brain volume is less significant than for the tumor.

Reproducibility is higher with the automated than with the manual method, because manual segmentation involves a human decision on every voxel while our automated segmentation method only requires the selection of a few example points for every tissue class. It has been previously shown by others that the statistical classification method used in our work (kNN rule) is robust with respect to the selection of tissue prototypes [25].

However, while interobserver variability is significantly reduced with the automated method for all cases, the intraobserver variability is lower only for the tumor segmentation of the meningioma cases. This can be explained with the different gray value distributions of the meningioma and the low grade gliomas with respect to the brain.

The meningioma tissue class partially overlaps with parts of the skin, fat in the neck and the straight and superior sagittal sinus, and is well distinguishable from brain tissue with the application of contrast enhancing agent. Restricting the region of interest (ROI) for the meningioma to the ICC, the tissues that show signal intensity overlap with the meningioma are excluded and the meningioma can be successfully segmented.

Low grade gliomas, however, are less distinguishable from brain tissue and ordinarily there is no contrast enhancement, making segmentation a more difficult task. This is indicated by the higher reproducibility of both methods for meningioma cases than for low grade gliomas cases.

In some cases, the choice of the ICC as ROI for the tumor segmentation may not be sufficient for an accurate segmentation. If signal intensity overlap between the tumor and the brain (usually gray matter) occurs, the automated segmentation may result in over- or under-segmentation depending on the spatial location of the voxels of the brain that were erroneously classified as tumor or vice versa.

The local refinement operations cannot correct false classifications, resulting in an over-segmentation of the low grade glioma if a) brain misclassified as tumor tissue is adjacent to the tumor boundary (over-segmentation), or b) tumor tissue on the boundary of the tumor is misclassified as brain (under-segmentation). The incorporation of T2 weighted images, which clearly distinguishes the tumor as hyperintense tissue, may enable the precise definition of the tumor boundaries. The local segmentation strategies correct classification artifacts if a) the voxels of the brain misclassified as tumor are distant to the tumor boundary or connected to the tumor only with thin structures, or b) tumor voxels "inside" the tumor are falsely classified as brain.

6.1.3 Conclusion

A new algorithm was developed for the automated segmentation of meningiomas and low grade gliomas. The method combines anatomical knowledge with statistical classification and low level segmentation techniques. The study shows that the brain and meningiomas and low grade gliomas can be accurately and reproducibly segmented by means of automated processing of gradient echo MRI. It is shown that the new algorithm allows complete segmentation of the brain and the tumor requiring only the manual selection of a small sample of example voxels (21–28).

6.2 Segmentation of White Matter Tract in Magnetic Resonance Images of Brain Tumor Patients

Introduction

One of the principal goals of neurosurgical planning is the localization of critical brain structures (e.g. eloquent areas, motor and sensory cortex) with respect to the tumor to define the safest possible surgical approach that ensures the least possible damage to the brain.

If a tumor is located close to the motor area (the precentral gyri) of the brain, the location of the white matter tracts is particularly important to the surgeon. These tracts converge fan-like from the motor cortex, connecting it to the spinal cord (Figure 6.6 (c)). A tumor close to the tracts may impair motor abilities of the patient, and the damage of theses structures during surgery may lead to spastic paralysis which cannot be recovered. Pre-operative knowledge about the deformation and location of the white matter tracts allows the surgeon to plan the surgical approach most likely to avoid additional damage of the white matter tracts.

The white matter tracts can be manually segmented from MRI by an experienced radiologist. However, manual segmentation is clinically not feasible, and automatic identification is not yet possible, because these structures do not differentiate in conventional MRI. MRI dedicated to the imaging of white matter bundles is not yet at the stage of providing exact information [104]. The registration of an anatomical atlas, where functional areas have been identified and segmented, enables to identify particular structures of the brain [86, 155].

This section presents a method to retrieve the structural information, in particular the white matter tracts, in patients with brain tumors, by using an automated image processing pipeline [76].

Methods

A representation of the image processing pipeline is illustrated in Figure 6.5. The patient dataset was segmented into the classes skin (fat/bone), brain, ventricles and tumor using the automated segmentation method (Section 4). Subsequently, the atlas was relabeled to contain only skin (fat/bone), brain and ventricles and registered to the segmented patient dataset (Chapter 5). The established deformation

field was applied to the white matter tracts, which had been previously extracted from the digital atlas.

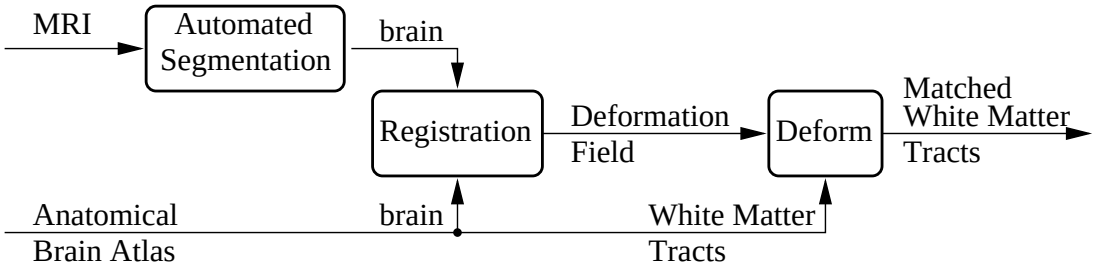

Figure 6.5: **Image processing pipeline for the projection of white matter tracts onto patients with brain tumors.** *The atlas brain is registered to the labeled patient's brain to compute the deformation field. Subsequently, the deformation field is applied to the white matter tracts and other structures of the atlas.*

Preliminary Results and Discussion

The result of the projected white matter tracts onto a brain tumor patient is shown in Figure 6.6 shows several 3D renderings of different anatomical structures of the patient, and structures projected from the atlas, i.e. the precentral gyri and the white matter tracts. Visual validation of the projected structures correlated well with the neuroradiological interpretation. The precentral gryi coincide with the correct gyri from the actual patient's brain model (Figure 6.6 (b)), and the white matter tracts passes the crus cerebri, a part of the brainstem, in the correct location (Figure 6.6 (d)). It can be also seen, that the projection of atlas structures is consistent, i.e. the white matter tracts touch the precentral gryi in the correct location (Figure 6.6 (c)).

It was demonstrated that structural information like the white matter tracts retrieved from a normal brain atlas can be projected onto patients with brain tumors with reasonable accuracy. This enables the visualization of complex anatomical relationships with minimal user interaction for surgical planning that cannot otherwise be visualized.

Currently, the method is limited to the special case of extrinsic tumors, because the registration method is not capable of matching structures that are topologically not equivalent.

Validation has been carried out visually. Future work will include the clinical validation on the basis of a larger number of cases, and the comparison of projected with manually segmented anatomical structures.

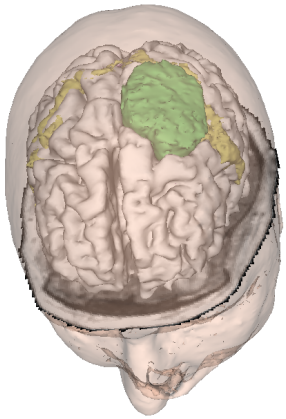

(a) 3D Model of a meningioma patient

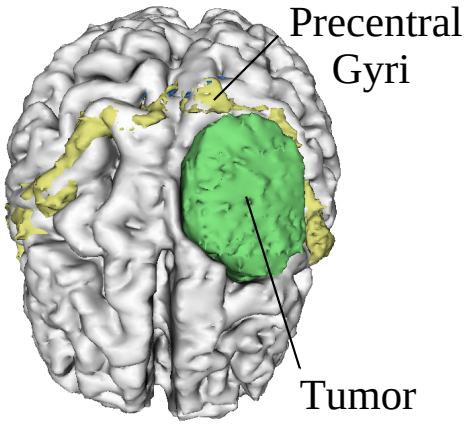

(b) Projected precentral gyri coincides with the manually generated brain model

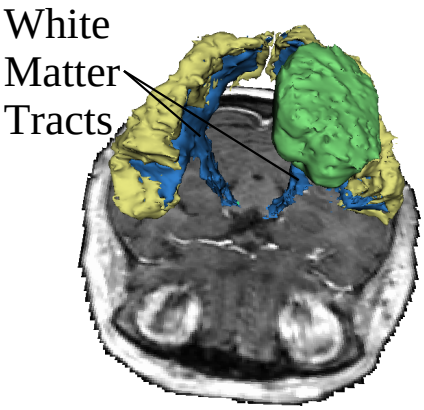

(c) Projection of structures is anatomically consistent

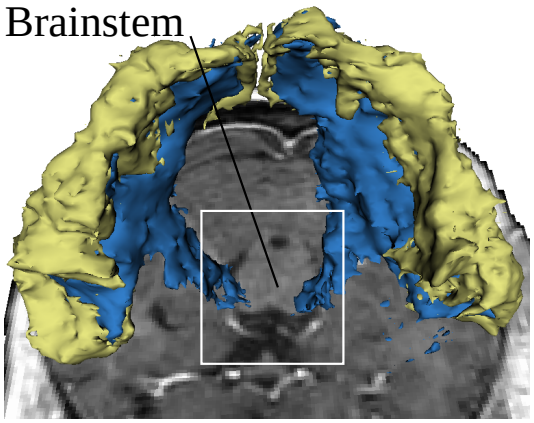

(d) White matter tracts passes crus cerebri (part of brainstem) correctly

Figure 6.6: **Visual verification of the structures projected from the atlas onto the patient's brain.** *Comparing the projected structures with manually segmented and grey value data of the patient show's that the precentral gyri coincide well with the manually segmented brain (b), the structures are projected coherently (i.e. the white matter tracts and the precentral gyri are connected in the correct locations) (c), and the white matter tracts passes the "crus cerebri" (part of the brainstem) at the correct location (d).*

Chapter 7

Conclusion

Computer based image guided technology and computer aided surgical planning have become increasingly utilized in neurosurgical treatment. While two-dimensional (2D) cross-sections of the intensity value images accurately describes the size and location of anatomical objects, the availability of three dimensional (3D) anatomical models significantly improves spatial information concerning relationships of critical structures (e.g. eloquent cortical areas, vascular structures) and pathology. Computer assisted techniques have shown the potential for increasing the safety in the removal of pathologic tissue, improving treatment outcome and reducing postoperative deficits.

Precise 3D modeling requires the segmentation of magnetic resonance images (MRI), and the lack of automated segmentation algorithms necessitates the use of interactive segmentation methods, which require tedious manual labor. This has been one of the reasons why 3D models have been typically limited to university research settings.

In this thesis, the problem of segmenting MRI in patients with brain tumors was studied. An algorithm was developed that allows the automated segmentation of some of the most common tumor types, meningiomas and low grade gliomas, from MRI data. With the combination of anatomical knowledge and local segmentation strategies such as statistical classification, mathematical morphology and region growing, normal and abnormal structures can be correctly identified, despite similar image intensity values of different tissue types. At the Surgical Planning Laboratory, the preliminary application of the method has reduced the operator time from 3 hours to 5-10 minutes. This makes it practical to consider the integration of computerized segmentation into daily clinical routine.

In this work, anatomical knowledge is integrated into the segmentation process through the registration of an anatomical atlas using an adaptive template matching approach. It has been shown how an N-channel probabilistic similarity measure achieves better accuracy than the conventional sum-of-squared difference (SSD) method for the registration of multiple anatomical templates. Also, the accuracy for the alignment of anatomical templates to images with classification errors could be improved with the use of this method. The improved registration results suggest an integration into the segmentation method presented in this work, with the potential of improving robustness and reducing computation time.

7.1 Summary

After an overview of the state of the art in Chapter 2 and an outline of the methodology of this work, a method for the automated segmentation of MRI in brain tumor patients was presented in Chapter 4. Initially, tissue composition and intensity distribution of brain and tumors (meningiomas and low grade gliomas) in spin-echo MRI were analyzed. It was shown that segmentation is not possible with the use of statistical classification or registration of an anatomical atlas alone, because a) statistical classification due to overlapping intensities of different tissue classes, or b) registration of an anatomical brain atlas because it does not describe pathology. A method for the automated segmentation of meningiomas and low grade gliomas was developed, based on the concept of adaptive template moderated classification (ATMC), a general segmentation framework which iterates between classification and registration. The method operates in stages, and sequentially segments the head, the brain, the ventricles and the tumor according to a hierarchical model of anatomy.

The use of optical flow methods for the task of aligning an anatomical atlas to individual patient datasets were analyzed in Chapter 5. A N-channel probabilistic (NP) similarity measure was presented, which increases the accuracy of a classic sum-of-squared difference (SSD) measure when registering multiple templates, and registering templates to images with segmentation errors. The improvement was achieved by a) making explicit use of the correspondence established with segmentation, i.e. separating labels of different objects into different channels, and b) using classification probabilities as confidence measures.

The algorithms were applied to different problems in the domain of medical image analysis and validated with synthetic and clinical image data (Chapter 6). The goal of the segmentation validation study was to assess the difference between the manual and the automated segmentation in terms of accuracy and reproducibility. A study based on 20 clinical datasets of patients with meningiomas and low grade gliomas demonstrated that automated segmentation produces comparable accuracy at higher inter-operator reproducibility in all cases. In the registration validation study, the performance of an adaptive template matching approach was analyzed in the framework of ATMC. The accuracy of two similarity measures (SSD and NP) were compared in a study based on synthetic and 5 clinical datasets. While both methods showed difficulties with the alignment of the 3rd and 4th ventricle, it was demonstrated that NP achieves better alignment for images with more than one object. Also, better alignment was achieved when using classification probabilities as confidence measures. The chapter concludes with the presentation of a method to project white matter tracts from a normal brain atlas onto patients with brain tumors.

7.2 Future Work

Adaptive template moderated segmentation (ATMC) is a method of combining registration and statistical classification into an iteration process. Registration was

implemented with adaptive template matching, and statistical classification with the kNN-rule. However, these may be substituted by or combined with complementary techniques which may improve the overall segmentation. Recent work by Kapur *et al.* [73, 74] on classification of MRI images using a Bayesian framework and spatial priors reports improved robustness to image noise. Preliminary work by Ferrant *et al.* [39] presents a biomechanical tissue model for the registration of medical images, that allows improved control over the type of deformation.

The improved accuracy for aligning multiple objects and segmentations of early stages of the ATMC segmentation cycle suggests the integration of the N-channel probabilistic (NP) similarity measure into ATMC. Future work will involve the redesign of the segmentation hierarchy to allow the segmentation of several objects in less iterations.

The similarity measures described in this work are not specific to non-linear template matching, but rather may be used with any kind of registration algorithm that uses a scalar similarity measure. For example, the use of the NP measure could be investigated with biomechanical deformation models to compute external forces.

In this work, non-linear registration was investigated for the registration of an anatomical atlas to individual patient datasets. However, other areas of applications, e.g. intra-operative registration to update preoperative images and 3D models would be interesting to investigate. Some of the problems known to make intra-operative registration difficult, e.g. intensity variations due to intra-operative application of contrast agent, field inhomogeneities and noise, are addressed by the NP similarity measure.

Segmentation of intra-operative images to update pre-operative image information and 3D models is another important application area. Preliminary trials using preoperatively segmented data as a template were carried out [142]. While reasonable result were obtained, future work will require algorithmical improvements to meet the time constraints of the neurosurgical intervention.

The segmentation method presented in this thesis is currently being used for the preparation of data for image guided surgery in a clinical setting. In an ongoing study, the method will be further evaluated based on a larger number of patient cases.

The tumor segmentation method has been applied to the segmentation of meningiomas and low grade gliomas. The extension to more complex tumors, e.g. glioblastoma multiforme, will involve the modeling of separate pathological tissue classes (e.g. enhancing and non-enhancing tissue, edema, cystic necrosis), improved use of anatomical information, and the investigation of additional imaging modalities.

Appendix A

Description of normal and pathologic Brain

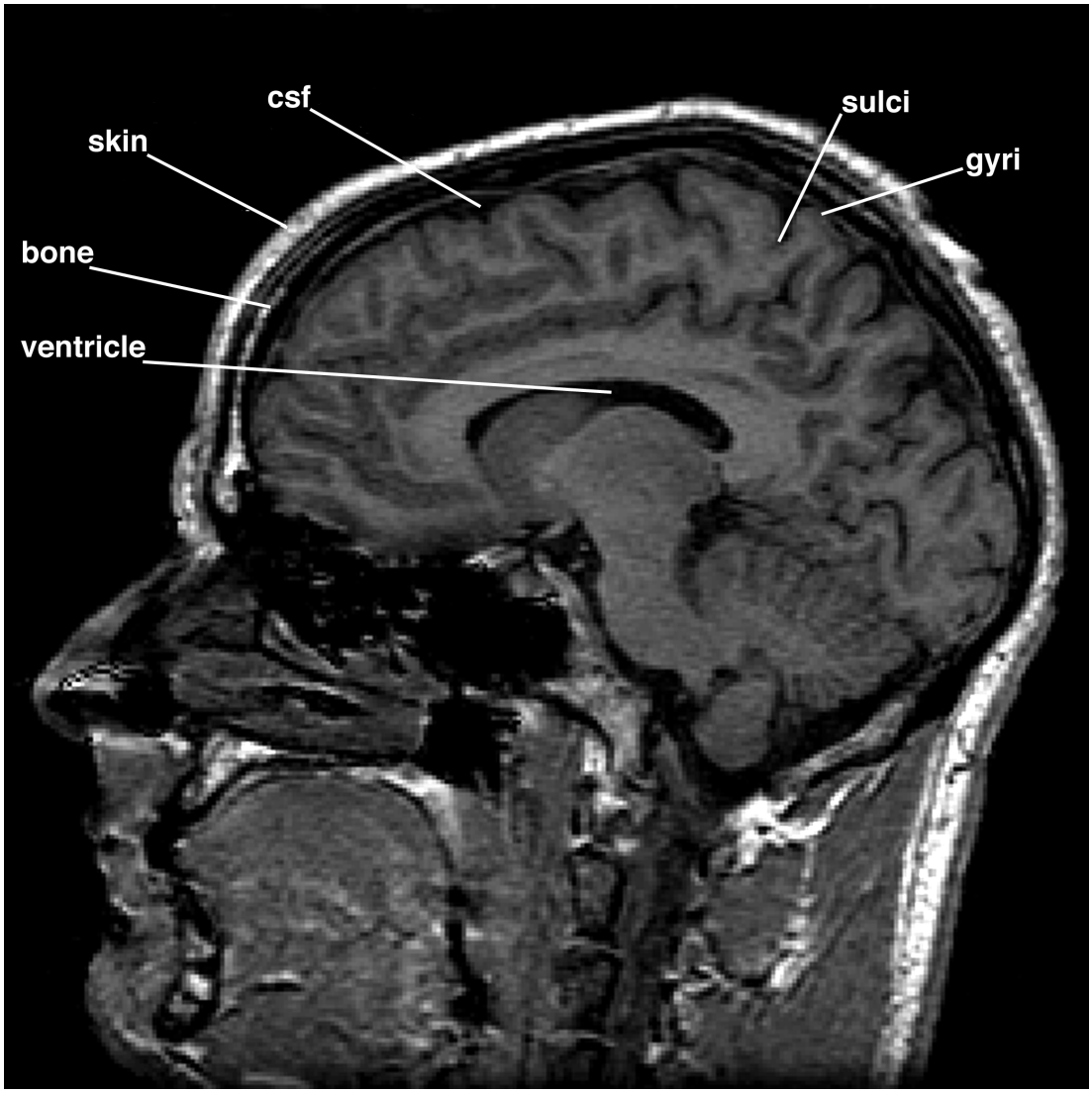

Figure A.1: **SPGR MR exam of a normal brain. The white matter is the brain tissue appearing light grey and the grey matter appears dark grey.**

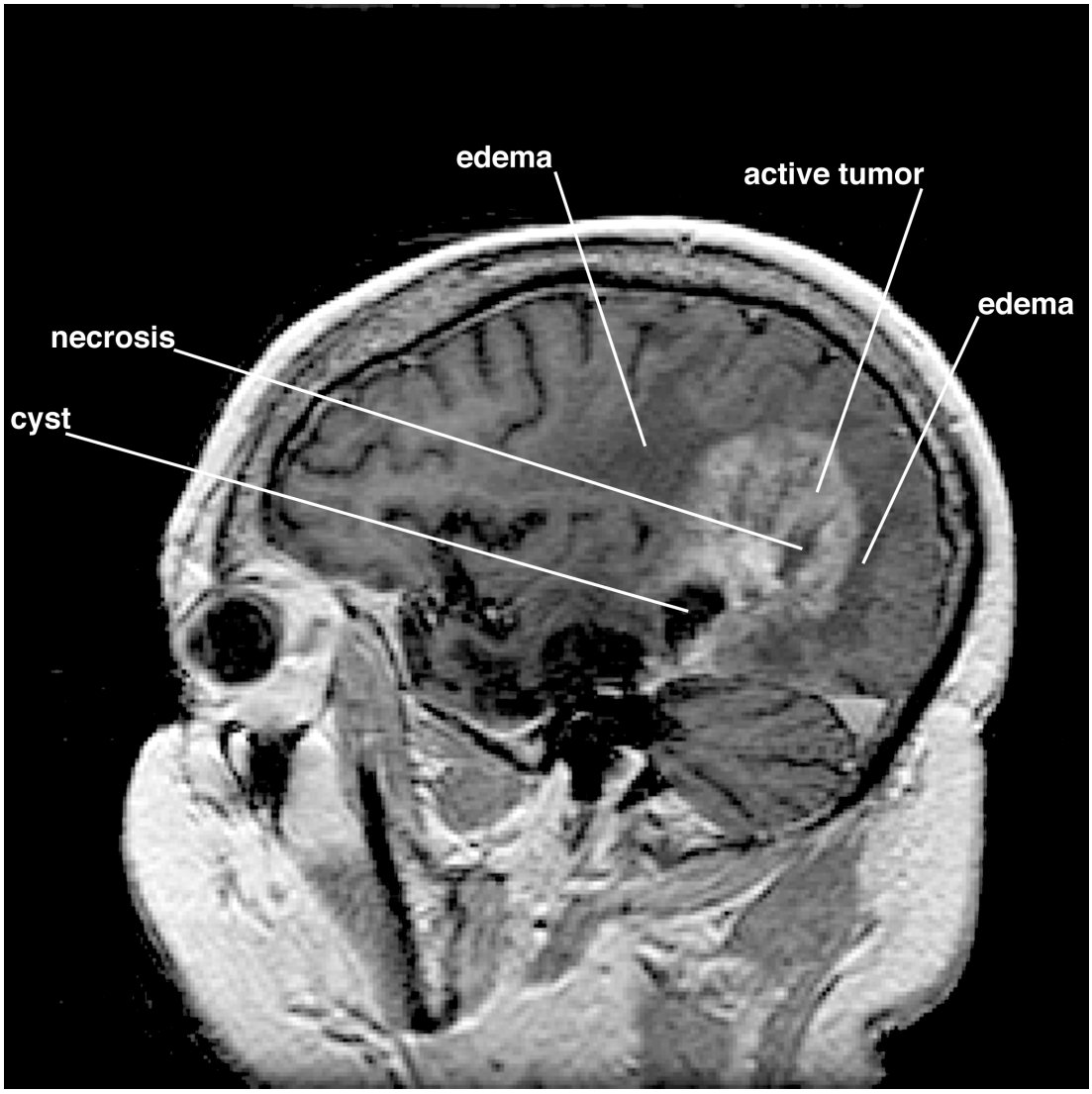

Figure A.2: **SPGR MR exam of a brain with a glioblastoma multiforme and related pathology.**

Appendix B

List of frequently used Abbreviations

ATMC	-	Adaptive Templater Moderated Classification
CAS	-	Computer assisted surgery
CGC	-	Coarse grid correction
CSF	-	Cerebro-spinal fluid
CT	-	Computer Tomography
CV	-	Coefficient of Variation
DOF	-	Degrees of freedom
FOV	-	Field of view
GRE	-	Gradient-recalled-echo
HPC	-	High Performance Computing
ICC	-	Intra-cranial cavity
M	-	Mean
MI	-	Mutual Information
MRI	-	Magnetic Resonance Imaging
MS	-	Multiple Sclerosis
NP	-	N-channel probabilistic similarity measure
OF	-	Optical flow
PD	-	Proton Density
PDE	-	Partial differential equation
ROI	-	Region of interest
SD	-	Standard Deviation
SE	-	Spin-echo
SNR	-	Signal-to-noise
SPGR	-	Spoiled gradient recalled
SRG	-	Seeded region growing
SSD	-	Sum of squared differences
TE	-	Echo time
TR	-	Repetition time
kNN	-	k-nearest-neighbour rule

Appendix C

Discretization of the Optical Flow PDE

The source and target image data is presented on a regular, discrete grid with cubic elements. In the following, a discretization of Equation (5.13) will be derived. Let the volumetric images $I_{1,2}$ (in the following treated as I) be defined on

$$\begin{aligned} x_{\min} \leq x \leq x_{\max} \\ y_{\min} \leq y \leq y_{\max} \\ z_{\min} \leq z \leq z_{\max} \quad . \end{aligned} \tag{C.1}$$

The discrete grid of I is defined with the integer indices $i_{\max}$, $j_{\max}$ and $k_{\max}$ and the grid spacing

$$\begin{aligned} h_x &= \frac{x_{\max} - x_{\min}}{i_{\max} - 1} \\ h_y &= \frac{y_{\max} - y_{\min}}{j_{\max} - 1} \\ h_z &= \frac{z_{\max} - z_{\min}}{k_{\max} - 1} \quad . \end{aligned} \tag{C.2}$$

Then for each grid point (i, j, k) the coordinates (x, y, z) are given by

$$\begin{aligned} x &= x_{\min} + (i-1)h_x \\ y &= y_{\min} + (i-1)h_y \\ z &= z_{\min} + (i-1)h_z \quad , \end{aligned} \tag{C.3}$$

where

$$\begin{aligned} 1 \leq i \leq i_{\max} \\ 1 \leq j \leq j_{\max} \\ 1 \leq k \leq k_{\max} \quad . \end{aligned} \tag{C.4}$$

In the following the notation $f_{i,j,k}$ and $f[i, j, k]$ are used to denote a value of a function $f(x, y, z)$, where x, y, z and i, j, k relate to each other according to Equation (C.3).

For the discretization of the Laplacian operator Δ, 2nd order central finite differences (see e.g. [16])

$$\frac{\partial^2 u}{\partial^2 x}[i,j,k] = u_{xx}[i,j,k] \approx \frac{u_{i-1,j,k} - 2u_{i,j,k} + u_{i+1,j,k}}{{h_x}^2} \tag{C.5}$$

for the approximation of the derivative in x-direction and similarly for y and z are used. Thus, Δ can be estimated with

$$\begin{aligned} \Delta u_{i,j,k} \approx & \frac{u_{i-1,j,k} - 2u_{i,j,k} + u_{i+1,j,k}}{{h_x}^2} + \frac{u_{i,j-1,k} - 2u_{i,j,k} + u_{i,j+1,k}}{{h_y}^2} + \\ & + \frac{u_{i,j,k-1} - 2u_{i,j,k} + u_{i,j,k+1}}{{h_z}^2} \quad . \end{aligned} \tag{C.6}$$

On a uniform grid with $h_x = h_y = h_z$, this leads to

$$\Delta u_{i,j,k} \approx u_{i,j,k} - \bar{u}_{i,j,k} \quad , \tag{C.7}$$

where

$$\bar{u}_{i,j,k} = \frac{\sum^W u_{i,j,k}}{\sum^W 1} \tag{C.8}$$

is the average of the neighbors of u and similarly for v and w.

The integral can be approximated with a sum over the integration volume, and the spatial image gradients ∇ are approximated with 1st order central finite differences

$$\frac{\partial I}{\partial x}[i,j,k] = I_x[i,j,k] \approx \frac{I_{i+1,j,k} - I_{i-1,j,k}}{2h_x} \tag{C.9}$$

for the derivative in x-direction and similarly for y and z.

With lexicographical ordering, i.e. $i = i + j * i_{\max} + k * i_{\max} * j_{\max}$, Equation (5.5) becomes

$$\begin{aligned} \mathbf{Q}(\mathbf{x}) &= \int^W \nabla I_1(\mathbf{x}) \nabla I_1(\mathbf{x})^T \, d\mathbf{x} \\ &\approx \begin{bmatrix} \sum_i^W I_{1x}^2[i] & \sum_i^W I_{1x}[i] I_{1y}[i] & \sum_i^W I_{1x}[i] I_{1z}[i] \\ \sum_i^W I_{1y}[i] I_{1x}[i] & \sum_i^W I_{1y}^2[i] & \sum_i^W I_{1y}[i] I_{1z}[i] \\ \sum_i^W I_{1z}[i] I_{1x}[i] & \sum_i^W I_{1z}[i] I_{1y}[i] & \sum_i^W I_{1z}^2[i] \end{bmatrix} \quad , \end{aligned} \tag{C.10}$$

and

$$\begin{aligned} \mathbf{f}(\mathbf{x}) &= \int^W \nabla I_1(\mathbf{x}) (I_2(\mathbf{x}) - I_1(\mathbf{x})) \\ &\approx \begin{bmatrix} \sum_i^W I_{1x}[i] (I_2[i] - I_1[i]) \\ \sum_i^W I_{1y}[i] (I_2[i] - I_1[i]) \\ \sum_i^W I_{1z}[i] (I_2[i] - I_1[i]) \end{bmatrix} \quad . \end{aligned} \tag{C.11}$$

Substituting equations Equation (5.5)) into Equation (5.13) results in the system of linear equations

$$\begin{bmatrix} \sum_i^W I_{1x}^2[i] & \sum_i^W I_{1x}[i]I_{1y}[i] & \sum_i^W I_{1x}[i]I_{1z}[i] \\ \sum_i^W I_{1y}[i]I_{1x}[i] & \sum_i^W I_{1y}^2[i] & \sum_i^W I_{1y}[i]I_{1z}[i] \\ \sum_i^W I_{1z}[i]I_{1x}[i] & \sum_i^W I_{1z}[i]I_{1y}[i] & \sum_i^W I_{1z}^2[i] \end{bmatrix} \begin{bmatrix} u[i] \\ v[i] \\ w[i] \end{bmatrix} - \lambda \begin{bmatrix} u[i] - \frac{\sum_i^W u_[i]}{\sum^W 1} \\ v[i] - \frac{\sum_i^W v_[i]}{\sum^W 1} \\ w[i] - \frac{\sum_i^W w_[i]}{\sum^W 1} \end{bmatrix} =$$

$$= \begin{bmatrix} \sum_i^W I_{1x}[i](I_1[i] - I_2[i]) \\ \sum_i^W I_{1y}[i](I_1[i] - I_2[i]) \\ \sum_i^W I_{1z}[i](I_1[i] - I_2[i]) \end{bmatrix} \quad . \tag{C.12}$$

Appendix D

Generation of synthetic Deformation Fields

A set of points (landmarks) $[\mathbf{p}_1, \ldots, \mathbf{p}_M]$, $\mathbf{p} = [x, y, x]^T]$ is manually identified in the template dataset. A set of random translations $[\mathbf{u}_1, \ldots, \mathbf{u}_M]$, $\mathbf{u}_i \leq 5$ mm $\mathbf{u}_i = [u_x(\mathbf{p}_i), u_y(\mathbf{p}_i), u_z(\mathbf{p}_i)]^T$, is generated for each landmark, and the corresponding coordinates $[\tilde{\mathbf{p}}_1, \ldots, \tilde{\mathbf{p}}_M]$ in the target image are calculated. The sets of corresponding landmarks is used to calculate a volumetric deformation field that transforms the template to the target landmarks and interpolates between these translation vectors based on a polynomial model.

The degrees of freedom needed to achieve the desired "warping" is not so important since we know where the landmarks are in both images. Thus, it is not necessary to get a perfectly deformed target where all landmarks have been warped to the exact location according to the random offset.

The relationship between locations $\mathbf{p}$ in the template and $\tilde{\mathbf{p}}$ in the target image is defined by the Nth-order polynomials

$$\tilde{x} = P_{\tilde{x}}(a_i, x, y, z) = \sum_{i=0}^{N}\sum_{j=0}^{N}\sum_{k=0}^{N} a_l x^i y^j z^k,\ i+j+k \leq N \quad , \tag{D.1}$$

and $\tilde{y} = P_{\tilde{y}}(b_i, x, y, z)$, $\tilde{z} = P_{\tilde{z}}(c_i, x, y, z)$ respectively. Writing the equations in vector form

$$\begin{bmatrix} \tilde{x} \\ \tilde{y} \\ \tilde{z} \end{bmatrix} = \begin{bmatrix} a_0 & \ldots & a_L \\ b_0 & \ldots & b_L \\ c_0 & \ldots & c_L \end{bmatrix} \begin{bmatrix} 1 \\ x \\ y \\ z \\ xy \\ \vdots \end{bmatrix} \quad , \tag{D.2}$$

and solving Equation (D.2) for $[\tilde{x}\,\tilde{y}\,\tilde{z}]$ leads to

$$\tilde{\mathbf{x}} = \mathbf{A}^T\mathbf{a}, \quad \tilde{\mathbf{y}} = \mathbf{A}^T\mathbf{b}, \quad \tilde{\mathbf{z}} = \mathbf{A}^T\mathbf{c} \quad , \tag{D.3}$$

where

$$\begin{aligned} \tilde{\mathbf{x}} = [\tilde{x}_1 \ \ldots \ \tilde{x}_M]^T, \quad \tilde{\mathbf{y}} = [\tilde{y}_1 \ \ldots \ \tilde{y}_M]^T, \quad \tilde{\mathbf{z}} = [\tilde{z}_1 \ \ldots \ \tilde{z}_M]^T \\ \mathbf{a} = [a_1 \ \ldots \ a_M]^T, \quad \mathbf{b} = [b_1 \ \ldots \ b_M]^T, \quad \mathbf{c} = [c_1 \ \ldots \ c_M]^T \quad , \end{aligned} \tag{D.4}$$

and

$$\mathbf{A} \ = \ \begin{bmatrix} 1 & x_1 & y_1 & z_1 & \ldots \\ 1 & x_1 & y_1 & z_1 & \ldots \\ 1 & x_1 & y_1 & z_1 & \ldots \\ \vdots & \vdots & \vdots & \vdots & \vdots \\ 1 & x_M & y_M & z_M & \ldots \end{bmatrix} \quad . \tag{D.5}$$

The polynomial coefficients a_l, b_l and c_l can be computed in a least-squares sense according to

$$\mathbf{a} = \mathbf{A}^{-1}\tilde{\mathbf{x}}, \quad \mathbf{b} = \mathbf{A}^{-1}\tilde{\mathbf{y}}, \quad \mathbf{c} = \mathbf{A}^{-1}\tilde{\mathbf{z}} \quad . \tag{D.6}$$

The deformation field $\mathbf{u}(x, y, z)$ for every voxel in the template image is calculated according to

$$\mathbf{u}(x, y, z) = \begin{bmatrix} P_{\tilde{x}}(a_l, x, y, z) - x \\ P_{\tilde{x}}(a_l, x, y, z) - y \\ P_{\tilde{x}}(a_l, x, y, z) - z \end{bmatrix} \quad . \tag{D.7}$$

Bibliography

[1] R. Adams and L. Bischof. Seeded region growing. *IEEE Transactions on Pattern Analysis and Machine Intelligence*, 16(6):642–645, 1994.

[2] E. Alexander, R. Kikinis, and F.A. Jolesz. Intraoperative Magnetic Resonance Imaging Therapy. In G.H. Barnett, D. Roberts, and B. Guthrie, editors, *Neurosurgery: Clinical Applications of Interactive Surgical Navigation*, pages 260–266, St. Louis, USA, 1996. Quality Medical Publisher.

[3] N. Ayache. Volume Image Processing: Results and Research Challenges. Technical Report RR-2050, Institute National de Recherche en Informatique et en Automatique (INRIA), Sophia-Antipolis, France, 1993.

[4] R. Bajcsy and S. Kovacic. Multiresolution Elastic Matching. *Computer Vision, Graphics and Image Processing*, 46:1–21, 1989.

[5] R. Bajcsy, R. Lieberson, and M. Reivich. A Computerized System for the Elastic Matching of Deformable Radiographic Images to Idealized Atlas Images. *Journal of Computer Assisted Tomography*, 7(4):618–625, 1983.

[6] J.L. Barron and S.S. Beauchemin. The Computation of Optical Flow. Technical report, Univ. of Western Ontario, Dpt. of Computer Science, London, Ontario, Canada, 1995.

[7] J.L. Barron, D.J. Fleet, and S.S. Beauchemin. Performance of Optical Flow. *IEEE International Journal of Computer Vision*, 12(1):43–77, 1994.

[8] J.C. Bezdek, L.O. Hall, and L.P. Clarke. Review of MR Image Segmentation Techniques using Pattern Recognition. *Medical Physics*, 20(4):1033–1048, 1993.

[9] P.M. Black, T. Moriarty, E. Alexander, P. Stieg, and E.J. Woodward. Development and Implementation of Intraoperative Magnetic Resonance Imaging and its Neurosurgical Applications. *Neurosurgery*, 41:831–845, 1997.

[10] A. Blake and A. Zisserman. *Visual Reconstruction*. MIT Press, Cambridge, MA, USA, 1987.

[11] F. Bookstein. *Morphometric Tools for Landmark Data: Geometry and Biology*. Cambridge University Press, Cambridge, MA, USA, 1991.

[12] Gunilla Borgefors. Distance transformations in arbitrary dimensions. *Computer Vision, Graphics, Image Processing*, 27:321–345, 1984.

[13] Chr. Brechbühler, G. Gerig, and G. Szekely. Compensation of Spatial Inhomogeneity in MRI Based on a Parametric Bias Estimate. In *LNCS No. 1131, Proceedings of the 4th International Conference on Visualization in Biomedical Computing*, pages 141–146, 1996.

[14] M. Bro-Nielsen and C. Grankow. Fast Fluid Registration of Medical Images. In *LNCS No. 1131, Proceedings of the 4th International Conference on Visualization in Biomedical Computing*, pages 267–276, 1996.

[15] C. Broit. *Optimal Registration of Deformed Images.* PhD thesis, University of Pennsylvania, Pennsylvania, USA, 1981.

[16] I.N. Bronstein and K.A. Semendjajew. *Taschenbuch der Mathematik.* Harri Deutsch Verlag, Berlin, 1990.

[17] M.E. Brummer, R.M. Mersereau, R.L. Eisner, and R.R. Lewine. Automatic Detection of Brain Contours in MRI Data Sets. *IEEE Transactions on Medical Imaging*, 12(2):153–166, 1993.

[18] A. Chabrerie, F. Ozlen, S. Nakajima, M.E. Leventon, H. Atsumi, E. Grimson, F.A. Jolesz, R. Kikinis, and P. Black. Three-dimensional Image Reconstruction for Low-Grade Glioma Surgery. *Neurosurgical Focus*, 4(4):Article 7, 1996.

[19] G. Christensen, R. Rabbitt, and M. Miller. Deformable Templates using large Deformation Kinematics. *IEEE Transactions on Medical Imaging*, 5(10):1435–1447, 1996.

[20] G.E. Christensen, M.I. Miller, J.L. Marsh, and M.W. Vannier. Automatic Analysis of Medical Images using a Deformable Textbook. In *Computer Assisted Radiology CAR*, pages 146–151, 1995.

[21] G.E. Christensen, R.D. Rabbitt, and M.I. Miller. 3D Brain Mapping using a Deformable Neuronatomy. *Physics in Medicine and Biology*, 39:609–618, 1994.

[22] M. Clark. *Knowledge Guided Processing of Magnetic Resonance Images of the Brain.* PhD thesis, University of Florida, Florida, 1998.

[23] M.C. Clark, L.O. Hall, D.B. Goldgof, L.P. Clarke, R.P. Velthuizen, and M.S. Silbiger. MRI Segmentation Using Fuzzy Clustering Techniques: Integrating Knowledge. In *IEEE Engineering Medicine and Biology Magazine*, page talk, 1994.

[24] L.P. Clarke, R.P. Velthuizen, M.A. Camacho, J.J. Heine, M. Vaidyanathan, L.O. Hall, R.W. Thatcher, and M.L. Silbinger. MRI Segmentation: Methods and Applications. *Magnetic Resonance Imaging*, 13(3):343–368, 1995.

[25] L.P. Clarke, R.P. Velthuizen, S. Phuphanich, J.D. Schellenberg, J.A. Arrington, and M. Silbinger. MRI: Stability of Three Supervised Segmentation Techniques. *Magnetic Resonance Imaging*, 11(1):95–106, 1993.

[26] H.E. Cline, E. Lorensen, R. Kikinis, and F.A. Jolesz. Three-Dimensional Segmentation of MR Images of the Head using Probability and Connectivity. *Journal of Computer Assisted Tomography*, 14(6):1037–1045, 1990.

[27] A. Collignon, F. Maes, D. Delaere, D. Vandermeulen, P. Suetens, and G. Marchal. Automated Multi-Modality Image Registration based on Information Theory. In *Proceedings of the 13th International Conference on Information Processing in Medical Imaging*, pages 263–274, 1995.

[28] D.L. Collins. *3D Model-Based Segmentation of Individual Brain Structures from Magnetic Resonance Imaging Data.* PhD thesis, McGill Uuniversity, Canada, 1994.

[29] D.L. Collins, G. Le Goualher, and A.C. Evans. Non-linear Cerebral egistration with Sulcal Constraints. In *1st. International Conference on Medical Image Computing and Computer-Assisted Intervention*, pages 974–984, 1998.

[30] D.L. Collins, G. Le Goualher, R. Venugopal, A. Caramanos, A.C. Evans, and C. Barillot. Cortical Constraints for Non-Linear Cortical Registration. In *LNCS No. 1131, Proceedings of the 4th International Conference on Visualization in Biomedical Computing*, pages 307–316, 1996.

[31] D.L. Collins, T.M. Peters, W. Dai, and A.C. Evans. Model based Segmentation of Individual Brain Structures from MRI Data. In *SPIE Vol. 1808, Proceedings of the 1st International Conference on Visualization in Biomedical Computing*, pages 10–23, 1992.

[32] J. Dengler and M. Schmidt. The Dynamic Pyramid - A Model for Motion Analysis with Controlled Continuity. *International Journal of Pattern Recognition and Artificial Intelligence*, 2(2):275–286, 1987.

[33] S. Dickson and B.T. Thomas. Using Neural Networks to automatically detect Brain Tumours in MR Images. *International Journal of Neural Systems*, 4(1):91–99, 1997.

[34] R.O. Duda and P.E Hart. *Pattern Classification and Scene Analysis.* John Wiley and Sons, New York, 1973.

[35] G. Ettinger, W.E.L. Grimson, M. Leventon, R. Kikinis, V. Gugino, W. Cote, M. Karapelou, L. Aglio, M. Shenton, G. Potts, and E. Alexander. Non-Invasive Functional Brain Mapping using Registered Transcranial Magnetic Simulation. In *IEEE Workshop on Mathematical Methods in Biomedical Image Analysis*, Registration I, 1996.

[36] A. Evans, W. Dai, L. Collins, P. Neelin, and S. Marrett. Warping of a Computerized 3-D Atlas to Match Brain Image Volumes for Quantitative Neuroanatomical and Functional Analysis. In *SPIE Medical Imaging V: Image Processing*, volume 1445, pages 236–246, 1991.

[37] A.C. Evans, D.L. Collins, and B. Milner. An MRI-based Stereotactic Brain Atlas from 300 young normal subjects. In *Proceedings of the 22nd Symposium of the Society for Neuroscience*, volume 408, 1992.

[38] A.C. Evans, J.A. Frank, J. Antel, and D.H. Miller. The Role of MRI in Clinical Trials of Multiple Sclerosis: Comparison of Image Processing Techniques. *Ann Neurol*, 41:125–132, 1997.

[39] M. Ferrant, S.K. Warfield, C.R. Guttmann, R.V. Mulkern, F.A. Jolesz, and R. Kikinis. 3D Image Matching using a Finite Element based Elastic Deformation Model. In *2nd International Conference on Medical Image Computing and Computer-Assisted Intervention*, pages 202–209, 1999.

[40] M. Fröder. *Darstellung geringkontrastiger Objekte im menschlichen Schädel mit rechnerunterstützter Röntegenvideotechnik.* PhD thesis, Lehrstuhl für Technische Elektronik, Universität Erlangen-Nürnberg, Erlangen, 1986.

[41] H. Fuchs. 3D Imaging in Medicine. In K.H. Höhne, H. Fuchs, and S. Pizer, editors, *Systems for Display of 3D Medical Image Data*, volume F60 of *Nato ASI Series*, pages 315–331. Springer-Verlag, Berlin-Heidelberg-Tokyo, 1990.

[42] K. Fukunaga. *Introduction to Statistical Pattern Recognition.* Academic Press, New York, 2nd edition, 1990.

[43] R.L.J. Galloway and R.J. Maciunas. Stereotactic Neurosurgery. *Critical Revisions of Biomedical Engineering*, 18:181–205, 1990.

[44] J.C. Gee, M. Reivich, and R. Bajcsy. Quantitative Analysis of Cerebral Images using an Elastically Deforming Atlas: Theory and Validation. *SPIE Medical Imaging IV: Image Processing*, 1652:260–269, 1992.

[45] J.C. Gee, M. Reivich, and R. Bajcsy. Elastically Deforming 3D Atlas to Match Anatomical Brain Images. *Journal of Computer Assisted Tomography*, 17(2):225–236, 1993.

[46] S. Geman and D. Geman. Stochastic Relaxation, Gibbs Distribution and the Bayesian Restoration of Images. *IEEE Transactions on Pattern Analysis and Machine Intelligence*, 6:721–741, 1984.

[47] G. Gerig, R. Kikinis, O. Kübler, and F.A. Jolesz. Nonlinear Anisotropic Filtering of MRI Data. *IEEE Transactions on Medical Imaging*, 11(2):221–232, 1992.

[48] G. Gerig, J. Martin, R. Kikinis, O. Kübler, M. Shenton, and F.A. Jolesz. Unsupervised Tissue Type Segmentation of 3D dual-echo MR Head Data. *Image and Vision Computing*, 10(6):349–360, 1992. IPMI 1991 Special Issue.

[49] D.T Gering, A. Nabavi, R. Kikinis, W.E.L. Grimson, N. Hata, P. Everett, F.A. Jolesz, and W.M. Wells. An Integrated Visualization System for Surgical Planning and Guidance using Image Fusion and Interventional Imaging. In *2nd International Conference on Medical Image Computing and Computer-Assisted Intervention*, pages 809–819, Cambridge, UK, 1999.

[50] P. Gibbs, D.L. Buckley, S.J. Blackband, and A. Horsman. Tumour Volume Determination from MR Images by Morphological Segmentation. *Physics in Medicine and Biology*, 41:2437–2446, 1996.

[51] S. Gilles, M. Brady, J. Declerck, J.-P. Thirion, and N. Ayache. Bias Field Correction of Breast Images. In *LNCS No. 1131, Proceedings of the 4th International Conference on Visualization in Biomedical Computing*, pages 153–158, 1996.

[52] S. Gilman. Imaging the Brain. *New England Journal of Medicine*, 338(12):812–896, 1998.

[53] R.C. Gonzalez and P. Wintz. *Digital Image Processing.* Addison-Wesley, Reading, MA, USA, 1987.

[54] W.E.L. Grimson, M. Leventon, A. Chabrerie, F. Ozlen, S. Nakajima, H. Atsumi, R. Kikinis, and P. Black. Clinical Experience with a high Precision Image-guided Neurosurgery System. In *1st. International Conference on Medical Image Computing and Computer-Assisted Intervention*, pages 63–73, 1998.

[55] W.E.L. Grimson, T. Lozano-Perez, W.M. Wells, G.J. Ettinger, S.J. White, and R. Kikinis. An automatic Rregistration Method for Frameless Stereotaxy, Image-guided Surgery, and enhanced Reality Visualization. *IEEE Transactions on Medical Imaging*, 15(2):129–140, 1996.

[56] D.H.W. Grönemeyer, R.M.M. Seibel, A. Melzer, et al. Future of advanced Guidance Techniques by interventional CT and MRI. *Minimally Invasive Therapy*, 4:251–259, 1995.

[57] J.W. Haller, G.E. Christensen, M.I. Miller, M. Gado, D.W. McKeel, J.G. Csernansky, and M.W. Vannier. A Comparison of Automated and Manual Segmentation of Hippocampus MR Images. In *SPIE Vol 2434, Proceedings of the Conference on Medical Imaging*, pages 206–215, 1995.

[58] R.M. Haralick and L.G. Shapiro. Image Segmentation Techniques. *Computer Vision, Graphics, Image Processing*, 29:100–132, 1985.

[59] N. Hata. *Rigid and deformable medical Image Registration for Image-guided Surgery.* PhD thesis, University of Tokyo, Tokyo, Japan, 1998.

[60] N. Hata, T. Dohi, S. Warfield, S.W. Wells, R. Kikinis, and F.A. Jolesz. Multimodality deformable Registration of pre- and intraoperative Images for MRI-guided Brain Surgery. In *1st. International Conference on Medical Image Computing and Computer-Assisted Intervention*, pages 1067–1074, 1998.

[61] K. Held, E. Rota Kops, B.J. Kraus, W. M. Wells, and R. Kikinis H.W. Müller-Gärtner. Markov Random Field Segmentation of Brain MRI Images. *IEEE Transactions on Medical Imaging*, 16(6):878–886, 1996.

[62] K.H. Höhne and W.A. Hanson. Interactive 3D Segmentation of MRI and CT Volumes using Morphological Operations. *Journal of Computer Assisted Tomography*, 16(2):285–294, 1992.

[63] K.H. Höhne, A. Pommert, M. Riemer, T. Schiemann, R. Schubert, U. Tiede, and W. Lierse. Framework for the generation of 3D Anatomical Atlases. In *SPIE Vol. 1808, Proceedings of the 1st International Conference on Visualization in Biomedical Computing*, pages 510–520, 1992.

[64] B.K.P. Horn and B.G. Schunk. Determining Optical Flow. *Artifical Intelligence*, 17:185–203, 1980.

[65] X. Hu, K.K. Tan, and D.N. Levin. Three-dimensional Magnetic Resonance Images of the Brain: Application to Neurosurgical Planning. *Journal of Neurosurgery*, 72:443–440, 1990.

[66] D.V. Iosifescu, M.E. Shenton, R. Kikinis, S.K. Warfield, and R.W. McCarley. Elastically Matching an MR Brain Atlas onto a new MR image of the Brain. In *Proceedings of the 8th Scientific Assembly and Annual Meeting, Radiological Society of North America*, pages 293–301, 1995.

[67] E.F. Jackson, L.E. Ginsberg, D.F. Schomer, and N.E. Leeds. A Review of MRI Pulse Sequences and Techniques in Neuroimaging. *Surgical Neurology*, 47:185–199, 1997.

[68] B. Jähne. *Digital Image Processing: Concepts, Algorithms and Scientific Application.* Springer-Verlag, Berlin-Heidelberg-Tokyo, 1991.

[69] F.A. Jolesz. Image-Guided Procedures and the Operating Room of the Future. *Radiology*, 204:601–612, 1997.

[70] M. Just, H.P. Higer, M. Schwarz, J. Bohl, G. Fries, P. Pfannenstiel, and M. Thelen. Tissue Characterization of Benign Brain Tumors: Use of NMR-Tissue Parameters. *Magnetic Resonance Imaging*, 6(4):463–472, 1988.

[71] M. Just and M. Thelen. Tissue Characterization with T1, T2 and Proton Density Values: Results in 160 Patients with Brain Tumors. *Radiology*, 169:779–785, 1988.

[72] M. Kamber, R. Shinghal, D.L. Collins, G.S. Francis, and A.C. Evans. Model-Based 3-D Segmentation of Multiple Sclerosis Lesions in Magnetic Resonance Brain Images. *IEEE Transactions on Medical Imaging*, 14(3):442–453, 1995.

[73] T. Kapur. *Model-Based Segmentation of Three-Dimensional Medical Images.* PhD thesis, MIT, Cambridge, MA, 1999.

[74] T. Kapur, W.E.L. Grimson, R. Kikinis, and W.M. Wells. Enhanced Spatial Priors for Segmentation of Magnetic Resonance Imagery. In *1st. International Conference on Medical Image Computing and Computer-Assisted Intervention*, pages 457–468, 1998.

[75] M. Kass, A. Witkin, and D. Terzopoulos. Snakes: Active Contour Models. *IEEE International Journal of Computer Vision*, 1(4):321–331, 1988.

[76] M.R. Kaus, A. Nabavi, S. Warfield, F.A. Jolesz, and R. Kikinis. Computer Simulation of the Displacement of white Matter Tracts in Patients with Brain Tumors for the Planning of Surgical Approaches. In *Proceedings of the Tagung der Deutschen Gesellschaft für Neurochirurgie*, Munich, Germany. Abstract, 1999.

[77] M.R. Kaus, S. Warfield, F.A. Jolesz, and R. Kikinis. Adaptive template moderated tumor segmentation of mri images. In *Workshop für Bildverarbeitung in der Medizin*, pages 102–106, Heidelberg, Germany, 1999.

[78] M.R. Kaus, S.K. Warfield, A. Nabavi, E. Chatzidakis, P. Black, F.A. Jolesz, and R. Kikinis. Automated Brain Tumor Segmentation in MRI: Meningiomas and Low Grade Gliomas. In *2nd International Conference on Medical Image Computing and Computer-Assisted Intervention*, pages 1–10, 1999.

[79] P.K. Kelly, B.A. Kall, S. Goerss, and F. Earnest. Computer-assisted stereotaxic Laser Resection of intra-axial Brain Neoplasms. *Journal of Neurosurgery*, 64:427–439, 1986.

[80] R. Kikinis, P.L. Gleason, T.M. Moriarty, M.R. Moore, E. Alexander III, P.E. Stieg, M. Matsumae, W.E. Lorensen, H.E. Cline, P.McL. Black, and F.A. Jolesz. Computer-assisted interactive three-dimensional Planning for Neurosurgical Procedures. *Neurosurgery*, 38:640–649, 1996.

[81] R. Kikinis, M.E. Shenton, D.V. Iosifescu, R.W. McCarley, P. Saiviroonporn, H.H. Hokama, A. Robatino, D. Metcalf, C.G. Wible, C.M. Portas, R. Donnino, and F.A. Jolesz. A Digital Brain Atlas for Surgical Planning, Model Driven Segmentation and Teaching. *IEEE Transactions on Visualization and Computer Graphics*, 2(3):232–241, 1996.

[82] B. Kim, J.L. Boes, K.A. Frey, and C.R. Meyer. Mutual Information for Automated Multimodal Image Warping. In *LNCS No. 1131, Proceedings of the 4th International Conference on Visualization in Biomedical Computing*, pages 349–354, 1995.

[83] L. Kjaer, P. Ring, C. Thomsen, and O. Henriksen. Texture Analysis in Quantitative MR Imaging: Tissue Characterisation of Normal Brain and Intracranial Tumors at 1.5 T. *Acta Radiologica*, 36:127–135, 1995.

[84] M.I. Kohn, N.K. Tanna, G.T. Herman, S.M. Resnick, P.D. Mozley, R.E. Gur, A. Alavi, R.A. Zimmerman, and R.C. Gur. Analysis of Brain and Cerebrospinal Fluid Volumes with MR Imaging. *Radiology*, 178(1):115–122, 1991.

[85] E. Krestel. *Bildgebende Systeme für die medizinische Diagnostik.* Siemens Aktiengesellschaft, Berlin, Germany, 1988.

[86] G. Le Goualher, D.L. Collins, C. Bariollot, and A.C. Evans. Automatic identification of cortical Sulci using a 3D probabilistic Atlas. In *1st. International Conference on Medical Image Computing and Computer-Assisted Intervention*, pages 509–518, 1998.

[87] D.N. Levin, X. Hu, K.K. Tan, et al. The Brain: Integrated three-dimensional Display of MR and PET Images. *Radiology*, 172:783–789, 1989.

[88] K.O. Lim and A. Pfefferbaum. Segmentation of MR Brain Images into Cerebrospinal Fluid Spaces, White and Grey Matter. *Journal of Computer Assisted Tomography*, 13(4):588–593, 1989.

[89] R.B. Lufkin. Interventional MRI. *Radiology*, 197:16–18, 1995.

[90] L.D. Lunsford, R. Parrish, and L. Albright. Intraoperative Imaging with a therapeutic computed tomographic Scanner. *Neurosurgery*, 15:559–561, 1984.

[91] D. MacDonald, D. Avis, and A.C. Evans. Multiple Surface Identification and Matching in Magnetic Resonance Images. In *SPIE Vol. 2359, Proceedings of the 3rd International Conference on Visualization in Biomedical Computing*, pages 160–169, 1994.

[92] R.J. Maciunas, M.S. Berger, B. Copeland, M.R. Mayberg, R. Selker, and G.S. Allen. A Technique for Interactive Image Guided Neurosurgical Intervention in Primary Brain Tumors. *Neurosurgery Clinics of North America: Clinical Frontiers of Interactive Image Guided Neurosurgery*, 245(7):323–331, 1996.

[93] J.A. Maintz. *Retrospective Registration of Tomographic Brain Images.* PhD thesis, Helmholtz Instituut, School for Autonomous Systems Research, Utrecht, Netherlands, 1996.

[94] T. McInnerney and D. Terzopoulos. Deformable Models in Medical Image Analysis: A Survey. *Medical Image Analysis*, 1(2):91–108, 1996.

[95] T. McInnerney and D. Terzopoulos. Deformable Models in Medical Image Analysis: A Survey. *Medical Image Analysis*, 1(2):91–108, 1996.

[96] M.I. Miller, G.E. Christensen, Y. Amit, and U Grenander. Mathematical Textbook of Deformable Neuroanatomies. *Proceedings of the National Academy of Science USA*, 90:11944–11948, 1993.

[97] S. Nakajima, H. Atsumi, A. Bhalerao, F.A. Jolesz, R. Kikinis, T. Yoshimine, T. Moriarty, and P. Stieg. Computer-Assisted Surgical Planning for Cerebrovascular Neurosurgery. *Neurosurgery*, 41(2):403–409, 1997.

[98] S. Nakajima, H. Atsumi, and R. Kikinis. Use of Cortical Surface Vessel Registration for Image-guided Neurosurgery. *Neurosurgery*, 40:1201–1210, 1997.

[99] W.W. Orrison, J.D. Lewine, J.A. Sanders, and M.F. Hartshorne. *Functional Brain Imaging.* Mosby-Year Book Inc, St. Louis, MO, USA, 1995.

[100] F. Ozlen, S. Nakajima, A. Chabrerie, M.E. Leventon, E. Grimson, R. Kikinis, F.A. Jolesz, and P. McL. Black. The Excision of Cortical Dysplasia in the Language Area with a Surgical Navigatior: A Casereport. *Epilepsia*, 39(12):1361–1366, 1998.

[101] A.M. Parikh. *Magnetic Resonance Imaging Techniques.* Elsevier, New York, NY, USA, 1992.

[102] P. Perona and J. Malik. Scale-Space and Edge Detection Using Anisotropic Diffusion. *IEEE Transactions on Pattern Analysis and Machine Intelligence*, 12(7):629–639, 1990.

[103] W.E. Phillips II, R.P. Velthuizen, S. Phuphanich, L.O. Hall, L.P. Clarke, and M.L. Silbinger. Application of Fuzzy C-Means Segmentation Technique for Tissue Differentiation in MR Images of a Hemorrhagic Glioblastoma Multiforme. *Magnetic Resonance Imaging*, 13(2):277–290, 1995.

[104] C. Poupon, J.F. Mangin, V. Frouin, J. Regis, F. Poupon, M. Pachot-Clouard, D. Le Bihain, and I. Bloc. Regularization of MR Diffusion Tensor Maps for tracking Brain White Matter Bundles. In *1st. International Conference on Medical Image Computing and Computer-Assisted Intervention*, pages 489–498, 1998.

[105] W.H. Press, S.A. Teukolsky, W.T. Vetterling, and B.P. Flannery. *Numerical Recipes in C.* Cambridge University Press, Cambridge, MA, USA, 1988.

[106] D.W. Roberts, J.W. Strohbehn, J.F. Hatch, W. Murray, and H. Kettenberger. A frameless stereotaxic Integration of computerized Tomographic Imaging and the Operating Microscope. *Journal of Neurosurgery*, 65:545–549, 1986.

[107] I. Roßmanith, H. Handels, S.J. Pöppl, E. Rinast, and H.D. Weiss. Characterisation and Classification of Brain Tumours in Three-Dimensional MR Image Sequences. In *LNCS No. 1131, Proceedings of the 4th International Conference on Visualization in Biomedical Computing*, pages 429–438, 1996.

[108] V.M. Runge, L.R. Muroff, and J.W. Wells. Principles of Contrast Enhancement in the Evaluation of Brain Diseases: An Overview. *Journal of Magnetic Resonance Imaging*, 7:5–13, 1997.

[109] L.R. Schad, S. Blüml, and I. Zuna. MR Tissue Characterization of Intracranial Tumors by Means of Texture Analysis. *Magnetic Resonance Imaging*, 11(6):889–896, 1993.

[110] J.F. Schenck, F.A. Jolesz, P.B. Roemer, H.E. Cline, W.E. Lorensen, R. Kikinis, S.G. Silverman, C.J. Hardy, W.D. Barber, E.T. Lakaris, B. Dorri, R.W. Newman, C.E. Holley, B.D. Collick, D.P. Dietz, D.C. Mack, M.D. Ainslee, P.L. Jaslolski, M.R. Figueira, J.C. Lehn, S.P. Souza, C.L. Dumoulin, R.D. Darrow,

R.L. Peters, K.W. Rohling, R.D. Watkins, D.R. Eisner, S.M. Blumenfeld, and K.G. Vosburgh. Superconducting open Configuration MRI System for Image-guided Therapy. *Radiology*, 195:805–814, 1995.

[111] M. Schmidt. *Mehrgitterverfahren zur 3D Rekonstruktion aus 2D Ansichten.* PhD thesis, Deutsches Krebsforschungszentrum Heidelberg (DKFZ), Heidelberg, Germany, 1988.

[112] J. Serra. *Image Analysis and Mathematical Morphology.* Academic Press, 1982.

[113] A. Simmons, S.R. Arridge, G.J. Barker, and P.S. Tofts. Segmentation of Neuroanatomy in Magnetic Resonance Images. *SPIE Medical Imaging VI: Image Processing*, 1652:2–13, 1992.

[114] E.P. Sipos, S.A. Tebo, and S.J. Zinreich. In Vivo Accuracy Testing and Clinical Experience with the ISG Viewing Wand. *Neurosurgery*, 39:194–204, 1996.

[115] J.A. Sorensen. *Course Notes for Medical Physics 568.* University of Wisconsin-Madison, Wisconsin, USA, 1997.

[116] C. Sorlié, D.L. Collins, K.J. Worsley, and A.C. Evans. An anatomical variability study based on landmarks. Technical report, McConnell Brain Imaging Center, McGill University, Montreal, Canada, 1994.

[117] R. Steinmeier, R. Fahlbusch, O. Ganslandt, C. Nimsky, M. Buchfelder, M.R. Kaus, T. Heigl, G. Lenz, R. Kuth, and W. Huk. Intraoperative Magnetic Resonance Imaging with the Magnetom Oopen Scanner: Concepts, Neurosurgical Indications, and Procedures: A Preliminary Report. *Neurosurgery*, 43(4):739–748, 1998.

[118] T.S. Sumanaweera, J.R. Adler, S. Napel, and G.H. Glover. Characterization of Spatial Distortion in Magnetic Resonance Imaging and its Implications for Stereotactic Surgery. *Neurosurgery*, 35(4):696–704, 1994.

[119] J. Talairach and P. Tournoux. *Co-planar stereotaxic Atlas of the Human Brain.* Thieme, New York, USA, 1988.

[120] D. Terzopoulos. Multi-Level Reconstruction of Visual Surfaces. Technical Report 671, Massachusetts Institute of Technology (MIT), Cambride, MA, USA, 1982.

[121] D. Terzopoulos. Computing Visible-Surface Representations. Technical Report 800, Massachusetts Institute of Technology (MIT), Cambridge, MA, USA, 1985.

[122] D. Terzopoulos. Regularization of Inverse Visual Problems Involving Discontinuities. *IEEE Transactions on Pattern Analysis and Machine Intelligence*, 8(4):413–424, 1986.

[123] J.P. Thirion and G. Calmon. Deformation Analysis to Detect and Quantify Active Lesions in 3D Medical Image Sequences. Technical Report 3101, Institute National de Recherche en Informatique et en Automatique (INRIA), Sophia-Antipolis, France, 1997.

[124] P. Thompson, D. MacDonald, M.S. Mega, C.J. Holmes, A. Evans, and A.W. Toga. Detection and Mapping of Abnormal Brain Structures with a Probabilistic Atlas of Cortical Surfaces. *Journal of Computer Assisted Tomography*, 21(4):467–481, 1996.

[125] P. Thompson and A.W. Toga. A Surface-Based Technique for Warping Three-Dimensional Images of the Brain. *IEEE Transactions on Medical Imaging*, 15(4):402–417, 1996.

[126] P. Thompson and A.W. Toga. Detection, Visualizaton and Animation of Abnormal Anatomic Structure with a Deformable Probabilistic Brain Atlas based on Random Vector Field Transformation. *Medical Image Analysis*, 1(4):1–24, 1997.

[127] P.M. Thompson, C. Schwartz, R.T. Lin, A.A. Khan, and W. Toga. Three-Dimensional Statistical Analysis of Sulcal Variability in the Human Brain. *Journal of Neuroscience*, 16(13):4261–4274, 1996.

[128] A.N. Tikhonov and V.Y. Arserin. *Solutions of Ill-Posed Problems*. Wiley, New York, 1977.

[129] A. Toga and P. Thompson. An Introduction to Brain Warping. In A. Toga, editor, *Brain Warping*, pages 1–26. Academic Press, 1999.

[130] V.M. Tronnier, C.R. Wirtz, M. Knauth, G. Lenz, O. Pastyr, M.M. Bonsanto, F.K. Albert, R. Kuth, A. Staubert, W. Schlegel, K. Sartor, and S. Kunze. Intraoperative Diagnostic and Interventional Magnetic Resonance Imaging in Neurosurgery. *Neurosurgery*, 40(5):891–902, 1997.

[131] M. Vaidyanathan, L.P. Clarke, L.O. Hall, C. Heidtman, L.P. Clarke, R.P. Velthuizen, K. Gosche, S. Phuphanich, H. Wagner, H. Greenberg, and M.S. Silbinger. Monitoring Brain Tumor Response to Therapy Using MRI Segmentation. *Magnetic Resonance Imaging*, 15(3):323–334, 1997.

[132] M. Vaidyanathan, L.P. Clarke, R.P. Velthuizen, S. Phuphanich, A.M. Bensaid, L.O. Hall, J.C. Bezdek, H. Greenberg, A. Trotti, and M. Silbinger. Comparison of Supervised MRI Segmentation Methods for Tumor Volume Determination During Therapy. *Magnetic Resonance Imaging*, 13(5):719–728, 1995.

[133] M.W. Vannier, R.L. Butterfield, D.L. Rickman, D.M. Jordan, W.A. Murphy, and P.R. Biondetti. Multispectral Magnetic Resonance Image Analysis. *Radiology*, 154:221–224, 1985.

[134] M.W. Vannier, T.K. Pilgram, C.M. Speidel, L.R. Neumann, D.L. Rickman, and L.D. Schertz. Validation of Magnetic Resonance Imaging (MRI) multispectral Tissue Classification. *Computerized Medical Imaging and Graphics*, 15:217–223, 1991.

[135] R.P. Velthuizen, L.P. Clarke, S. Phuphanich, L.O. Hall, A.M. Bensaid, J.A. Arrington, H.M. Greenberg, and M.L. Silbinger. Unsupervised Measurement of Brain Tumor Volume on MR Images. *Journal of Magnetic Resonance Imaging*, 5:594–605, 1995.

[136] S. Vinitski, C. Gonzalez, F. Mohamed, T. Iwanaga, R.L. Knobler, K. Khalili, and J. Mack. Improved Intracranial Lesion Characterization by Tissue Segmentation based on a 3D Feature Map. *Magnetic Resonance in Medicine*, 37:457–469, 1997.

[137] P. Viola and W.H. Wells. Alignment by Maximization of Mutual Information. In *Proceedings of the 6th International Conference on Computer Vision*, pages 16–23, 1995.

[138] S. Warfield, F.A. Jolesz, and R. Kikinis. A High Performance Computing Approach to the Registration of Medical Image Data. *Parallel Computing*, 24:1345–1368, 1998.

[139] S. Warfield, M.R. Kaus, F.A. Jolesz, and R. Kikinis. Adaptive Template Moderated Spatially Varying Statistical Classification. In *1st. International Conference on Medical Image Computing and Computer-Assisted Intervention*, Boston, MA, USA, 1998.

[140] S.K. Warfield. *Segmentation of Magnetic Resonance Images of the Brain*. PhD thesis, University of New South Wales, Sydney, Australia, 1997.

[141] S.K. Warfield, J. Dengler, J. Zaers, C.R.G. Guttmann, W.M. Wells, G.J. Ettinger, J. Hiller, and R. Kikinis. Automatic Identification of Grey Matter Structures from MRI to Improve the Segmentation of White Matter Lesions. *Journal of Image Guided Surgery*, 1(6):326–338, 1995.

[142] S.K. Warfield, J.A. Jolesz, and R. Kikinis. Real-time Image Segmentation for Image-guided Surgery. In *High Performance Networking and Computing Conference*, 1998. Abstract No. 106.

[143] S.K. Warfield, A. Robatino, J. Dengler, F.A. Jolesz, and R. Kikinis. Nonlinear Registration and Template Driven Segmentation. In A. Toga, editor, *Brain Warping*, pages 67–84. Academic Press, 1999.

[144] E. Watanabe, Y. Mayanagi, and Y. Yosugi. Open Surgery Assisted by the Neuronavigator, a Stereotactic, Articulated, Sensitive Arm. *Neurosurgery*, 28:792–800, 1991.

[145] E. Watanabe, T. Watanabe, S. Manaka, Y. Mayanagi, and K. Takakura. Three-dimensional Digitizer (Neuronavigator): New Equipment for computed tomography-guided stereotaxic Surgery. *Surgical Neurology*, 27(6):543–547, 1987.

[146] F.W. Wehrli, D. Shaw, and J.B. Kneeland. *Biomedical Magnetic Resonance Imaging. Principles, Methodology, and Applications.* VCH Publishers Inc., NY, USA, 1988.

[147] W.H. Wells, R. Kikins, W.E.L. Grimson, and F.A. Jolesz. Adaptive Segmentation of MRI Data. In *Proceedings of the 1st International Conference on Computer Vision, Virtual Reality and Robotics in Medicine*, pages 61–69, 1995.

[148] W.H. Wells, R. Kikins, W.E.L. Grimson, and F.A. Jolesz. Adaptive Segmentation of MRI Data. *IEEE Transactions on Medical Imaging*, 15:429–442, 1995.

[149] W.H. Wells, R. Kikins, and F.A. Jolesz. Statistical Intensity Correction and Segmentation of Magnetic Resonance Image Data. In *SPIE Vol. 2359, Proceedings of the 3rd International Conference on Visualization in Biomedical Computing*, pages 13–24, 1994.

[150] W.H. Wells, P. Viola, H. Atsumi, S. Nakajima, and R. Kikinis. Multi-Modal Volume Registration by Maximization of Mutual Information. *Medical Image Analysis*, 1(1):35–51, 1996.

[151] J. West *et al.* Comparison and Evaluation of Retrospective Intermodality Brain Image Registration Techniques. *Journal of Computer Assisted Tomography*, 21:554–566, 1997.

[152] M.G. Yasargil. *Microneurosurgery.* Georg Thieme Verlag, Stuttgart, Germany, 1994.

[153] H. Zhu, H.Y. Francis, F.K. Lam, and P.W.F. Poon. Deformable Region Model for Locating the Boundary of Brain Tumors. In *Proceedings of the IEEE 17th Annual Conference on Engineering in Medicine and Biology*, page 411, 1995.

[154] Y. Zhu and H. Yan. Computerized Tumor Boundary Detection using a Hopfield Neural Network. *IEEE Transactions on Medical Imaging*, 16(1):55–67, 1997.

[155] A. Zijdenbos, R. Forghani, and A.C. Evans. Automatic Quantification of MS Lesions in 3D MRI Brain Data Sets. In *1st. International Conference on Medical Image Computing and Computer-Assisted Intervention*, pages 439–448, 1998.